Star clusters across the ages: internal kinematics from stellar nurseries to ancient globulars

Hannah Suzanne Dalgleish

A thesis submitted in partial fulfilment of the requirements of
Liverpool John Moores University
for the degree of
Doctor of Philosophy
April 2020

Declaration

The work presented in this thesis was carried out at the Astrophysics Research Institute, Liverpool John Moores University. Unless otherwise stated, it is the original work of the author.

While registered as a candidate for the degree of Doctor of Philosophy, for which submission is now made, the author has not been registered as a candidate for any other award. This thesis has not been submitted in whole, or in part, for any other degree.

Hannah Suzanne Dalgleish
Astrophysics Research Institute
Liverpool John Moores University
IC2, Liverpool Science Park
146 Brownlow Hill
Liverpool
L3 5RF
United Kingdom

July 22, 2020

Abstract

This thesis comprises the dynamical study of star clusters in the Milky Way and Magellanic Clouds from early to ancient times. Much is unknown about the formation of high-mass stars and clusters — our understanding is deeply hindered by the obscuration of stars by thick columns of dust and gas. One can infer the motions of stars in star-forming regions, however, via radio observations of ionised gas. By way of example, I examine a young, bipolar H II region in the Galactic disc which lies at the centre of a massive ($\sim 10^3$ $M_\odot$) infrared-dark cloud filament. Intriguingly, the region known as G316.81–0.06, displays a large velocity gradient (47.81 ± 3.21 km s^{-1} pc^{-1}) along the same direction as the filament — a phenomenon scarcely observed at this stage of evolution. Based on a qualitative comparison between G316.81–0.06 and simulations of young star-forming regions, the velocity gradient can be explained by rotation, inferred to be a direct result of the initial angular momentum of the natal molecular cloud. If true, this kinematic signature should be common in other young (bipolar) H II regions and may help to discern the scenario by which star clusters form and evolve.

Star clusters at ancient times (i.e. globulars) appear in an entirely different form. Rid of their natal gaseous cocoons, globulars visibly contain 10^5 – 10^6 stars, held together by their mutual gravity. One particular conundrum appeared in recent decades: observed mass-to-light ratios (M/L) of metal-rich globular clusters (GCs) disagree with theoretical predictions. This discrepancy is of fundamental importance since stellar population models provide the

stellar masses that underpin most of extragalactic astronomy, near and far. Using integral-field unit data from the WAGGS project, I have extracted radial velocities for 1,622 stars located in the centres of 59 Milky Way GCs — twelve of which have no previous kinematic information — in order to calculate dynamical masses and M/L_V ratios via N-body modelling. Most importantly, the sample includes NGC 6528 and NGC 6553, which extend the metallicity range of GCs with measured M/L up to [Fe/H] ~ -0.1 dex. The results confirm that metal-rich clusters have M/L_V more than two times lower than what is predicted by simple stellar population models, and thus the discrepant M/L–[Fe/H] relation remains a serious concern. I have explored the potential origin of the divergence, and it appears that dynamical effects are the most likely explanation.

With great technological advances in recent years, the internal kinematics of more distant star clusters can also be probed, such as massive star clusters in the Magellanic Clouds. These clusters are as young as ~ 1 Myr and are thought to be the progenitors of ancient globulars. Thus, this provides a unique opportunity for the study of globular formation at a relatively unexplored snapshot in time. I have carried out a preliminary study of eleven (young, intermediate-age and old) massive clusters in the Clouds as an extension of the M/L–[Fe/H] study of GCs. With this, I can then test stellar population models and improve constraints on theories of dynamical evolution at early times. Newly discovered *Gaia* star clusters present another avenue for novel research. Home to a new area of parameter space, these clusters appear to be old and compact, yet they are faint (V-band magnitude $\lesssim -2.5$ mag). This is an exciting opportunity to advance our knowledge of (heavily dissolved) star clusters which seem to be approaching the end of their lifetime.

Publications

In the course of completing the work presented in this thesis, the following papers have been published in a refereed journal:

H. S. Dalgleish, S. Kamann, C. Usher, H. Baumgardt, N. Bastian, J. Veitch-Michaelis, A. Bellini, S. Martocchia, G. S. Da Costa, D. Mackey, S. Bellstedt, N. Pastorello, P. Cerulo. The WAGGS project – III. Discrepant mass-to-light ratios of Galactic globular clusters at high metallicity. *MNRAS*, 492(3):3859–3871, March 2020.

H. Baumgardt, C. He, S. M. Sweet, M. Drinkwater, A. Sollima, J. Hurley, C. Usher, S. Kamann, **H. S. Dalgleish**, S. Dreizler, T. -O. Husser. No evidence for intermediate-mass black holes in the globular clusters ω Cen and NGC 6624. *MNRAS*, 488(4):5340–5351, Oct 2019. Contribution: providing radial velocity data and comments.

C. Usher, T. Beckwith, S. Bellstedt, A. Alabi, L. Chevalier, N. Pastorello, P. Cerulo, **H. S. Dalgleish**, A. Fraser-McKelvie, S. Kamann, S. Penny, C. Foster, R. McDermid, R. Schiavon, A. Villaume. *MNRAS*, 482(1):1275–1303, Jan 2019. Contribution: providing comments.

H. S. Dalgleish, S. N. Longmore, T. Peters, J. D. Henshaw, J. Veitch-Michaelis, J. S. Urquhart. Ionized gas kinematics in bipolar H II regions. *MNRAS*, 478(3):3530–3543, Aug 2018.

Alongside this work, I also published the following:

H. S. Dalgleish & J. Veitch-Michaelis. Assessing the influence of one astronomy camp over 50 years. *Nature Astronomy*, 3:1043–1047, Dec 2019.

Hannah Suzanne Dalgleish July 22, 2020

Acknowledgements

I'm not someone who often remembers my dreams, but one dream in particular has stayed with me for many years — perhaps for even more than a decade. I was walking, and what was a hill quickly turned into a mountain. It grew steeper and steeper until I was climbing almost vertically. All I wanted to do was give up, but a hand reached out to grab mine and it never let go. This dream has comforted me every time I found myself in the 'depths of despair'; I would make it through and I would have the help I needed to reach the stars.

As with every PhD, there are a multitude of people without whom this work could not have been accomplished. I wouldn't be here if it were not for the experiences of my past. To my time in St Andrews, London (the Canadian one), and with AstroMundus — you challenged me and hurled me outside of my comfort zone, nourished me and prepared me for this journey and whichever path is to come. To my previous supervisors: you are the academic foundations upon which my abilities as a researcher have been built. To Scott G. Gregory, who supported, guided and encouraged me at all times, and trained me to be a clear communicator. To Miguel A. Urbaneja, a source of never-ending laughter and whose doubt in my capabilities never wavered. To all at ePOD: thank you for your essential training and for carving and moulding me into a better communicator.

Thank you to all at the ARI, if only more departments could be like you: friendly, attentive, and doors always wide open in every direction you turn. To Steve and Nate, your combined supervision has been phenomenal. Thank you for being so supportive (especially when I wanted to do things a bit unconventionally), for never tiring of my 'stupid' questions, and for always knowing what to do. To Jonny, Sebastian, and Chris

— your help and knowledge has been indispensable. To Marie, I am struggling to find the words to say how important you have been to me on this journey — you are my rock, always listening, never judging. To Andy, you are an inspiration, I greatly admire all that you have done for the world of art, outreach, and education and I hope one day to achieve even half as much as you. To Jon, Kirsty, Silvia, Lawrence, Ted, Emma, Ash, Ivan, and William for your banter, and many a wild Friday night. To Penny, for always being there with a chocolate hobnob on the first Tuesday of every month and for putting this journey into perspective. To Victoria, thank you for everything and more! I will never forget our TransPeer travels together and how you helped me with my mammoth fellowship application (you too Andreas!) and got me onto loose leaf tea. To Nora, oh Nora, I am utterly indebted to you and so, so grateful that we crossed paths, it's not often that a deep friendship just clicks in an instant but you know as much as I do that we are a rare exception.

To my family, genetic or otherwise (Bedia, Francesca, and the Casses, I'm looking at you) — thank you for believing in me and continuing to love me even though I never call you back. To Miffy, you will always have a cherished place in my heart and I am sure that you have been with me this whole time. To Chisholme, I cannot fathom who I would be if it were not for your existence. You are an eternal source of grounding, in case I ever drift too far from Earth. To the IAYC, you taught me the hardest and most wondrous lessons in life, and probably are the reason for my pursuing astronomy for so long. You showed me true heartbreak, friendship, but that ultimately, I don't have to go it alone. To Josh, for taking a leap and joining me here in Liverpool so that we could be together (bet you never thought you'd be riding out a pandemic with me!). You are an angel, an excellent tear sponge, and there is not a problem you cannot solve. Thank you for being you, and for letting me be me. Many more adventures await for each of us, sometimes alone (don't get frozen in Antarctica!), sometimes together, but we grow ever stronger. Thank you for celebrating every achievement, big or small. Here's to many more.

Hannah Suzanne Dalgleish July 22, 2020

Without going outside, you may know the whole world.
Without looking through the window, you may see the ways of heaven.
The farther you go, the less you know.

Thus the wise know without travelling;
See without looking;
Work without doing.

Lao Tsu

Everyone says it is plain that the stars go around the earth while the Earth remains still. I say that it is plain to the eyes of the lunar people that our Earth, which is their Volva, goes around while their moon is still. If it be said that the lunatic perceptions of my moon-dwellers are deceived, I retort with equal justice that the terrestrial senses of the Earth-dwellers are devoid of reason.

Johannes Kepler

If I propose to ascertain the influence of one mote in a sunbeam upon its neighboring mote, I cannot accomplish my purpose without first counting and weighing all the atoms in the Universe and defining the precise positions of all at one particular moment. If I venture to displace, by even the billionth part of an inch, the microscopical speck of dust which lies now upon the point of my finger, what is the character of that act upon which I have adventured? I have done a deed which shakes the Moon in her path, which causes the Sun to be no longer the Sun, and which alters forever the destiny of the multitudinous myriads of stars that roll and glow in the majestic presence of their Creator.

Edgar Ellen Poe

Contents

List of Tables

List of Figures

Chapter 1

Introduction

> *And what is even more remarkable, the stars which have been called 'nebulous' by every astronomer to this time, turn out to be groups of small stars wonderfully arranged.*
>
> Galileo Galilei

1.1 The history of star clusters

1.1.1 The nebulae that were not nebulae at all

Throughout history, our understanding of the Universe has been deeply entwined with the advancement of technology. Four hundred and ten years ago, on 13th March, Galilei (1610) published the *Sidereus Nuncius* (The Starry Messenger) which changed the course of astronomy forever[1]. The work was the first examination of the heavens based on telescopic observation[2] — his ideas were extremely controversial and led to a radical deviation away from an Aristotelian understanding of the Universe. Galilei revealed that the Moon's surface was neither translucent nor a perfect orb

[1] Although one ought not to forget the heliocentric view established by Nicolas Coperincus and Johannes Kepler before him.

[2] Galilei was the first to publish, yet he was not the first to use a telescope for astronomical purposes. In 1609, Thomas Harriot made unpublished drawings based on his observations of the Moon.

— as Aristotle had claimed — but instead covered with craters and mountains. Other breakthroughs include the discovery of four of Jupiter's moons[3]; this revelation contradicted the notion that all heavenly bodies orbited the Earth, a key principle of Aristotelian astronomy.

Figure 1.1: Sketch of Praesepe, a "nebula" in the constellation Cancer. The two larger stars (upper left and lower right) are visible with the naked eye. The other 40+ stars are visible only with a telescope. Reproduced from Galilei (1610).

Less known is Galilei's study of Praesepe, a so-called "nebula", the Latin name for 'cloud' or 'fog'. For millennia, misty patches in the night sky have been referred to as nebulae, from comets to open clusters to the Andromeda galaxy[4] (Jones, 1975; Archinal & Hynes, 2003; Hoskin, 2008). As Galilei looked through the lens of his telescope Praesepe was not nebulous, but instead revealed faint stars clustered together (Figure 1.1). Of all the nebulae observed at the time, the Orion nebula was the first true nebula to be discovered, by Nicolas Claude Fabri de Peiresc in 1610 (Chapin, 1957). Intriguingly, Galilei never mentioned the nebula in any of his works, despite devoting copious time observing the constellation, giving rise to the

[3]It has been long debated whether Galilei or his rival Simon Marius observed the satellites first (Pasachoff, 2018; Zik et al., 2020). Regardless, Io, Europa, Ganymede and Callisto are the names given by Marius.

[4]Andromeda was first recorded in the *Book of the Fixed Stars* at around 964 AD by the Persian astronomer, Abd al-Rahman al-Sufi (Hafez et al., 2015). Andromeda was later rediscovered by Marius (1614), who writes, "the luster appears almost as if a candle shining through translucent horn were to be discerned from far off."

thought that perhaps it was not visible to him at the time (Harrison, 1984). Giovan Battista Hodierna also observed the Orion nebula, as noted in his remarkable 1654 publication. Hodierna was devoted to cataloguing and classifying[5] nebulae (Figure 1.2), and presented a unifying (cosmological) theory to try and explain all that he saw. Unfortunately his work has gone by entirely unnoticed for centuries, save an in-depth account from Serio et al. (1985).

Figure 1.2: The three classifications (Luminosae, Nebulosae, and Occultae) of nebulae as determined by Hodierna (1654).

Just as open clusters and galaxies were misidentified as nebulae, so too were globular clusters — as far as we know, Johannes Hevelius was the first to detect a globular, namely Messier 22. This was about 15 years before Edmond Halley (1679) observed a fuzzy blob, Omega Centauri[6], during his trip to St Helena in the South Atlantic Ocean (Burnham, 1978; Cook, 1998). Dick (2013), however, makes an interesting point: should the discovery of an object be attributed to the first person who observed it, or to the first person to have accurately described it? Following this reasoning, it is perhaps William and Caroline Herschel who are the true discovers of globular clusters, the first to resolve a cluster into its constituent stars, and thereafter the vast majority of clusters in the northern hemisphere (Herschel, 1786, 1789, 1802).

After decades of study, the Herschels consequently faced the difficult question: are all nebulae simply congeries of stars waiting to be resolved? Inspired by observations of the Orion nebula (Figure 1.3)[7], and after much deliberation, Herschel (1791) eventually came to judge that "the nebulosity about the star is not of a starry nature",

[5]Hodierna classified nebulae into three distinct classes: Luminosae (stars visible with the naked-eye e.g. the Pleiades), Nebulosae, and Occultae (stars which could and could not be resolved with a telescope, e.g. Praesepe and Andromeda, respectively).

[6]Omega Centauri is recorded in Ptolemy's *Almagest* (150 AD), but is listed as a star.

[7]See Holden (1882) for a fascinating monograph which comprises ~ 40 'eye-drawings' of the Orion nebula up until the first photograph taken by Draper (1880).

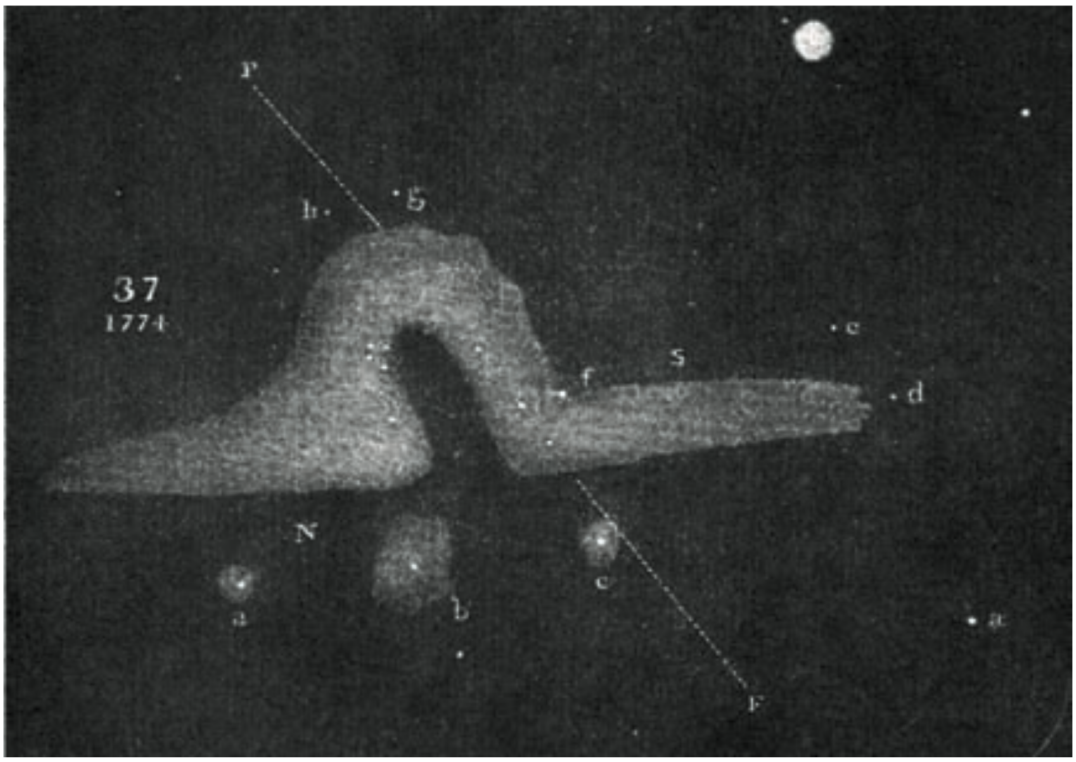

Figure 1.3: William Herschel's drawing of the nebula in Orion (1774). Reproduced from The Scientific Papers of Sir William Herschel, Vol. 2, Plate III, Fig. 37.

meaning that he had come to believe in the possibility of true nebulosity (Hoskin, 2011b,c; Nasim, 2013). Solid proof came when William Huggins spectroscopically analysed the light from the nebula in Draco, confirming that it was made up of gas[8]. Having observed nebulae and star clusters in the thousands — significantly more than any other astronomer alive at the time — the Herschel's came to other fundamental conclusions. Herschel (1814) reasoned that each object was a snapshot in time under the order of a much greater evolutionary sequence (Figure 1.4). Beginning with nebulae, the luminous material would condense and collapse into stars; those stars would then gravitate together and form globular clusters, which he would go on to describe as "undoubtedly the most interesting objects in the heavens".

[8]This discovery in itself is built upon the pioneering work of Newton (1666) who dispersed light into a spectrum using a prism; and Wollaston (1802) and Fraunhofer (1814) who observed dark absorption lines in the solar spectrum beforehand.

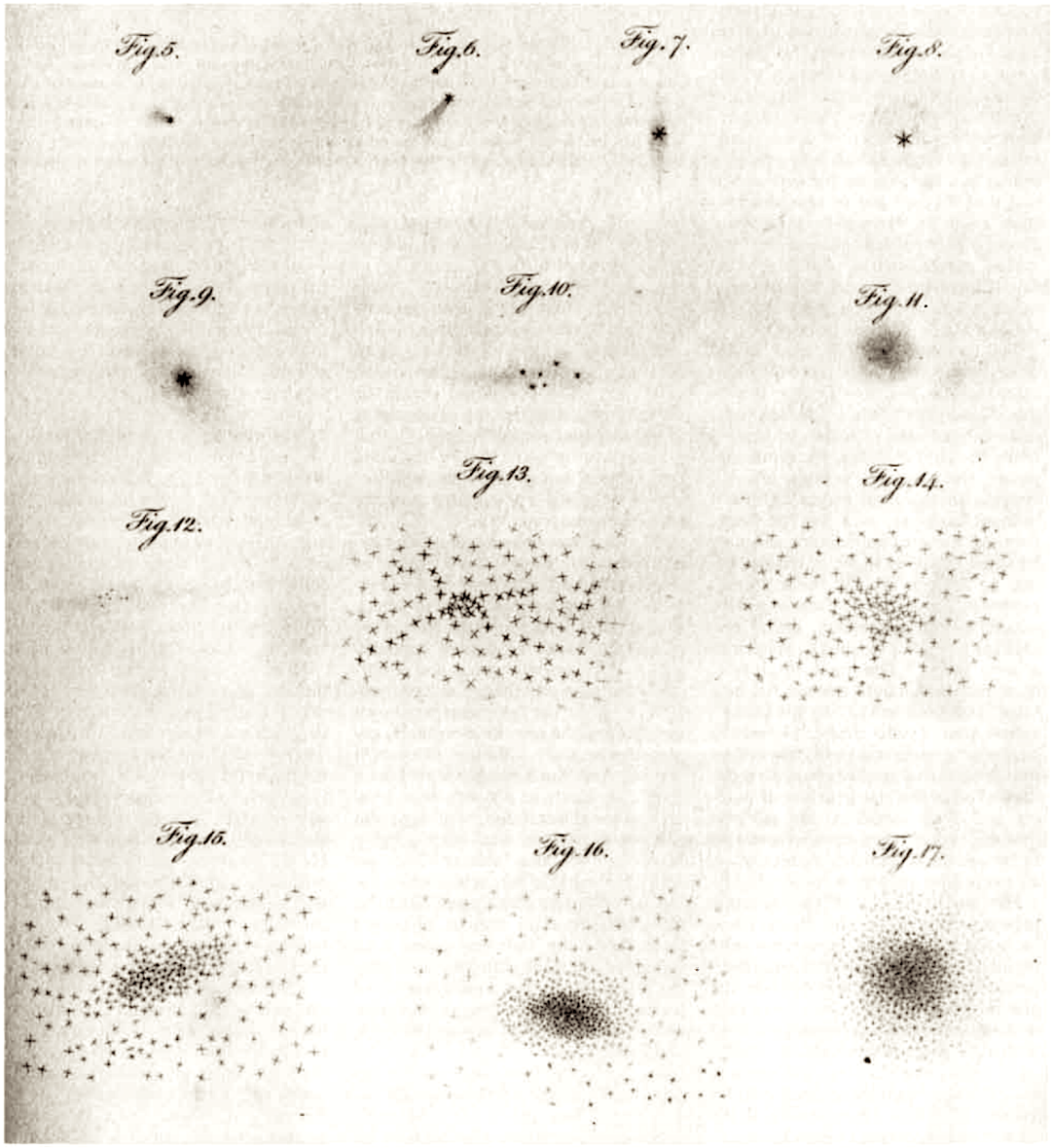

Figure 1.4: Herschel illustrates the maturation of nebulae and star clusters. Luminous matter congeals and accumulates, from which individual stars form. The stars continue to grow by accreting nebulosity and are then drawn together by gravity. The resultant globular cluster eventually tends toward collapse (bottom right). Reproduced from Herschel (1814).

1.1.2 Introducing spectroscopy and photography

It is said that modern astrophysics as we know it originates in spectroscopy and the explanation of the Fraunhofer lines. In recording the spectra of six different elements[9] from flames and sparks, Kirchhoff & Bunsen (1860) reflected that a similar method

[9] Lithium, sodium, potassium, calcium, strontium and barium.

could also be applied to stellar atmospheres, demonstrating the huge potential for the chemical analysis of stellar spectra.

At roughly the same time, it emerged that spectroscopy could do much more than detect elements in the firmament — the technique was central to further breakthroughs (i.e. radial velocities), which would open into a new branch of kinematics. The Doppler (1842) principle[10] shows that the motions of an observer or source cause a shift in perceived frequency. Although incorrect, Doppler was certain that this effect explained a long-standing puzzle regarding the observations of different coloured stars[11]. Unaware of Doppler's work, Fizeau gave a lecture in 1848 which accurately suggested that spectral line displacements could be used to measure celestial velocities. In two decades time it would become possible to measure the first line-of-sight velocity of a star, thus confirming Fizeau's prediction (Huggins, 1868).

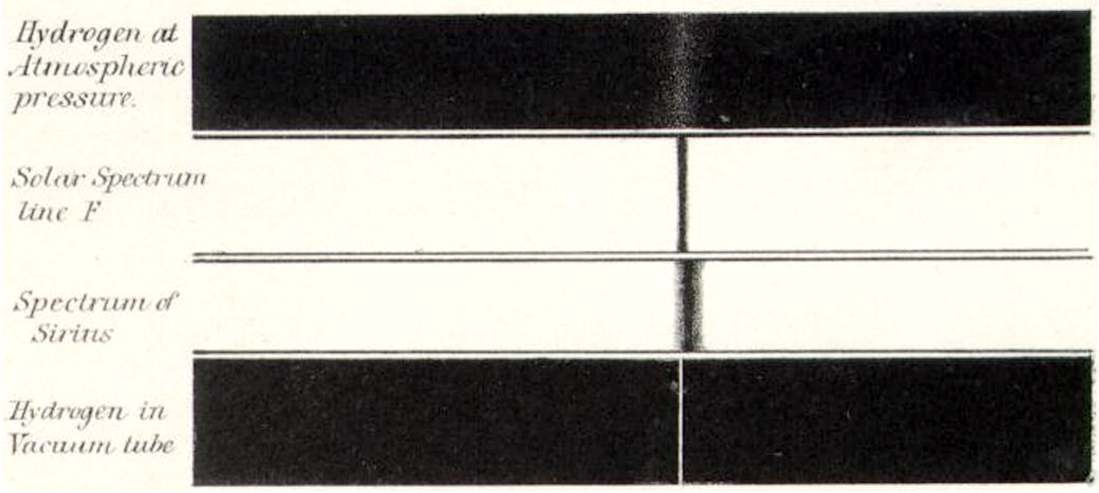

Figure 1.5: Spectra of Sirius, used to determine radial velocity. Reproduced from Huggins (1868), Figure 4.

Despite observing the brightest star in the sky, Sirius, Huggins' experiment was a tremendous feat as he had to measure the spectrum visually (Figure 1.5), before the invention of the dry gelatin photographic plate (Maddox, 1871). Though his

[10] Interestingly, Doppler's principle for sound was verified by Ballot (1845) who designed the following experiment: a horn player was placed on a train and produced a single note, while musicians with perfect pitch stood on the platform and estimated the tone as the train approached and receded.

[11] See Smyth (1864) for a lovely colour chart, based on observations of more than 100 double stars.

value was out by an order of magnitude, Huggins' efforts piqued the interest of other astronomers who would go on to record spectra on photographic plates and hence determine more accurate velocities for stars (Vogel, 1873, 1889; Maunder, 1885, 1892; Keeler, 1890b) and nebulae (Keeler, 1890a). But it would be many years until astronomers calculated stellar velocities in star clusters; first in open clusters (Trumpler, 1935; Smith & Struve, 1944; Struve, 1944; Feast, 1958), and later for globulars (Wilson & Coffeen, 1954; Feast & Thackeray, 1960)[12].

The invention of photography was key to further astronomical revolutions. Prior to photographic plates and charge-coupled devices, astronomers depended on textual descriptions which were difficult to visualise, or drawings made by hand (e.g. Figure 1.6). Trouvelot was one such artist who was world-renowned[13] for creating hundreds of accurate and evocative depictions of the Universe. As astrophotography

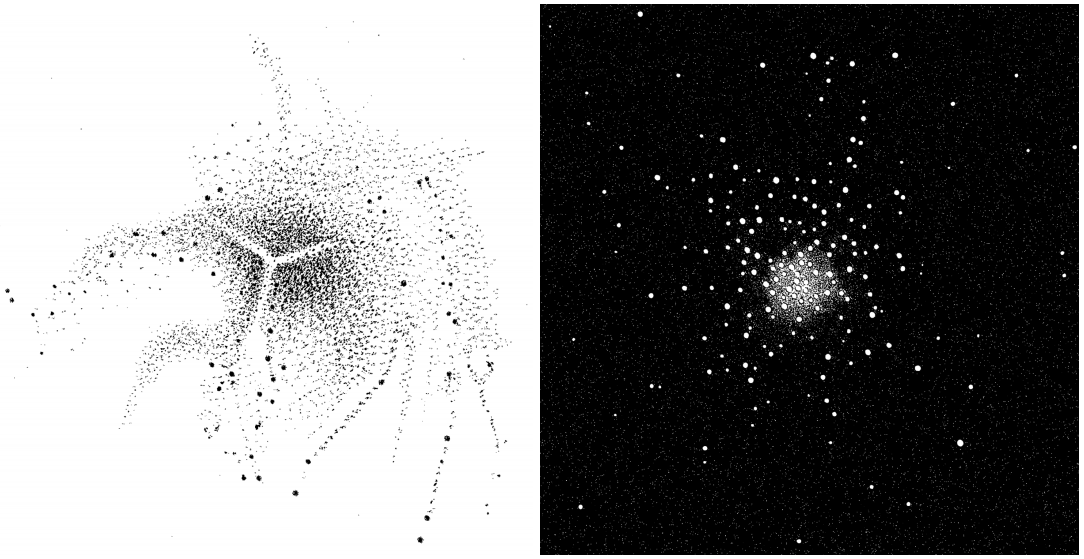

Figure 1.6: Drawings of the Herculean globular cluster, M13. Illustrated by Bindon Stoney in 1855 (left) and Trouvelot in 1874 (right). Reproduced from Rosse (1861) and Winlock & Trouvelot (1876).

grew in popularity, Isaac Roberts and Dorothea Klumpke became two of the most distinguished experts in the practice. They photographed hundreds[14] of star clusters

[12]The radial velocities catalogued by Adams et al. (1929) and Moore (1932) also deserve to be mentioned, where a few of the measurements listed belong to star clusters.

[13]This is the same, unfortunate Trouvelot who is infamous for accidentally releasing gypsy moths in Massachusetts. The moths have devastated millions of hardwood trees throughout the eastern United States.

[14]Roberts is reported to have taken more than 200 images of objects beyond the Solar System within the year 1885 alone (Hockey et al., 2007).

(e.g. Figure 1.7) and nebulae over several years and their work was of great value to the scientific community (Roberts, 1893, 1899; Klumpke-Roberts, 1929, 1931):

> *Every astronomical reader is familiar with Dr. Roberts' celestial photographs... He may be said to have continued with the photographic plate the work that the Herschel's accomplished visually with their giant telescopes. Dr. Roberts has not only nobly enriched astronomical science, but has a monument to himself which will last as long as astronomy has any interest for mankind. This handsome book, besides being a most valuable mine of information, serves as a demonstration of the success that has rewarded his efforts after an infinite amount of most skilful instrumental adjustment and working.*
>
> William Lockyer (1900)

So far, the aforementioned work has primarily focused on the Northern Hemisphere and the need for cataloguing the Southern skies was becoming evermore apparent. Edward Pickering, the fourth director of the Harvard College Observatory, was keen to achieve worldwide coverage of the sky and advance his *Harvard Photometry* catalogue. Pickering seemed to have a natural ability to secure funding; through procuring a ~$238,000 bequest[15] left by Uriah A. Boyden (Bailey, 1931), in combination with additional funds from the New England elite, he was able to undertake an ambitious quest — the construction of a Southern observatory at high altitude.

In 1889, Solon Irving Bailey, Pickering's closest and most trusted collaborator, embarked on an expedition to the Andes to scout for an elevated site worthy of astronomical research. Bailey travelled with his wife, three-year-old son, and brother (Ruth, Irving, and Marshall), reaching as far south as Santiago. After two years of arduous search, Bailey settled on a site near Arequipa in Peru, at 8,055 feet. The Boyden Station would remain in active operation until the end of 1926[16]; Ruth and Solon Bailey went on to visit Arequipa five times in total, alternating between the Station and Cambridge (MA).

[15] Which would now be worth ~ 6.5 million US dollars (assuming inflation since 1887). In spite of the handsome sum, almost all the money was exhausted before 1893 (Gingerich, 2010).

[16] Regretfully, the Peruvian workers who helped to construct and maintain the Arequipa Observatory have not received the credit that they so rightly deserve (McGrath, 2019).

Figure 1.7: M13, taken on 22nd May, 1887 with an exposure of 60 minutes. One of the first photographs of a globular cluster. 'Dark lanes' can be seen in the shape of a Y. These lanes were also noticed by previous artists (Figure 1.6). Reproduced from Roberts (1893).

> *In Peru and on his various trips through tropical wilds, Bailey encountered many exciting situations, including rapids, earthquakes, a revolution, and a mild naval battle. He passed through all these vicissitudes with his usual alert serenity.*
>
> Edward S. King (1931)

Over the years spent at Arequipa, Bailey made thousands of photographs, never wasting a moment of clear sky. Every plate was sent back to Cambridge and analysed by the Harvard Computers, led by Williamina Fleming. Their detailed investigations revealed thousands of unseen astronomical objects, including nebulae, variable stars, novae, asteroids, satellites, and more (Bailey, 1931). Bailey's plates of

the Magellanic Clouds enabled Henrietta Leavitt's discovery of the Cepheid period-luminosity relationship. It was Bailey who discovered the existence of a new type of variable star (RR Lyraes). Undoubtedly, his observations built the foundations upon which Shapley would later become so famous (Cannon, 1931). In particular, Bailey also partook in exciting and novel work in the realm of globular clusters. Bailey (1893) was the first to try and quantitatively infer the distribution of stars within a globular cluster (Figure 1.8). Further work was carried out by Palmer (1899); Pickering & Fleming (1897); Bailey (1916) and included the first radial density profiles.

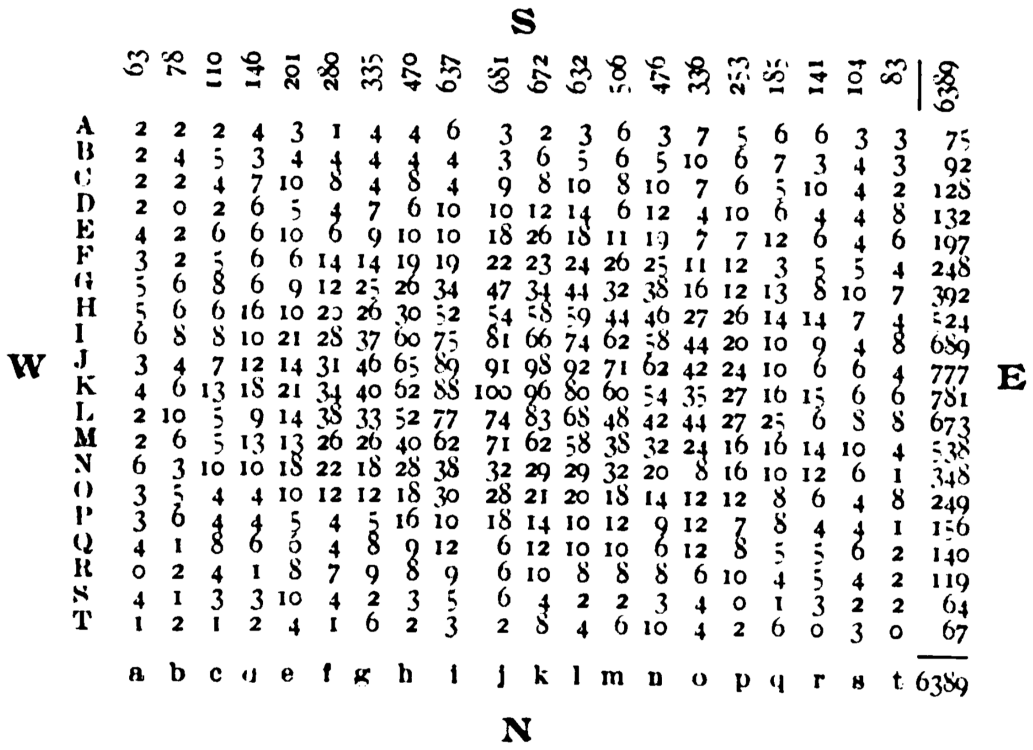

Figure 1.8: The mean number of stars distributed in Omega Centauri as counted by Solon and Ruth Bailey. The data was obtained from a two-hour exposure taken on a photographic plate in Arequipa, Peru. Reproduced from Bailey (1893), Figure 2.

To this end, I conclude a brief history of star clusters with an aim to cover the discoveries which eventually led to the field of kinematics. There is much more globular-related science that has not been discussed; for an excellent overview which extends to chemistry, distance measurements, proper motions, binaries, stellar populations, Leavitt's period-luminosity relation, the Hertzprung-Russell diagram, etc. see Shapley (1930) and Sawyer Hogg (1959). A current understanding of star clusters follows in the next Section.

For the fascinated reader who wishes to delve deeper, see Archinal & Hynes (2003) for a historical study of star clusters; Hockey et al. (2007) for a splendid encyclopedia of astronomers; Hoskin (2008, 2011a, 2012) for all things William and Caroline Herschel; Hearnshaw (2009, 2014) for the cultural and social history of astronomical spectroscopy; Steinicke (2010) for the making of the New General Catalogue; Gingerich (2010) for the birth of astrophysics (*c.*1850 – *c.*1920); Dick (2013) for discussion on the concept of 'extended discovery' as the engine of progress; and Nasim (2013) for the production and reception of hand-drawn images of nebulae in the 19th century.

1.2 Star clusters today

In the present day, we know that the historically so-called 'nebulae' in fact take on a variety of forms: from distant galaxies to star-forming regions to star clusters. The Milky Way (MW) and its local neighbourhood are ideal locations for the detailed study of star clusters (SCs) at different evolutionary times. Young star-forming regions and open clusters appear in the Galactic plane, while ancient globular clusters (GCs) are located in the Galactic halo and bulge — these GCs are some of the oldest structures in the Universe, at an age of ~12 Gyr. The Magellanic Clouds (MCs), on the other hand, are habitats to clusters of all ages, ranging from ~ 1 Myr to ~ 10 Gyr.

This thesis focuses on the study of star clusters — and the internal motions of the stars within them — in different environments and stages of life. Kinematics is the observational study of the motions of objects through space. The observational techniques used to determine the movements of stars within clusters depends on the context. For example, stars in star-forming regions are invisible to optical instruments, but their motions can be inferred via radio observations. Stars in local GCs can be observed optically, but suffer from crowding, especially at the cluster centre; it is easier to spectroscopically resolve stars in the outer regions. These radio and optical aspects are introduced in the upcoming sections.

The remaining chapters in this thesis include an investigation into the internal kinematics of a recently ionised star-forming region in the Galactic disc (Chapter 2).

This is followed by a study of the mass-to-light ratios of Galactic globular clusters (Chapter 3). To conclude, kinematical studies of Magellanic Cloud star clusters and the discovery of new, low-mass and ancient clusters — at the boundary between open and globular clusters — is discussed in Chapter 4 as an avenue for future work. First, an overview of our current understanding of star-forming region dynamics is explored (Section 1.2.1), followed by Milky Way star clusters (Section 1.2.2) and Magellanic Cloud star clusters (Section 1.2.3).

1.2.1 The dynamics of star-forming regions

When we look at the stars in the Milky Way and in nearby galaxies, we find that the vast majority of newly-formed stars ($t \approx 10$ Myr) appear in groups. The size and compactness of the stellar grouping ranges over wide scales and their distribution depends upon the initial conditions of the star-forming region (Elmegreen & Efremov, 1997; Lada & Lada, 2003; Kruijssen, 2012). At one extreme, stars are found in low-mass, unbound clusters (e.g. stellar associations); in the Local Group more than 90% are found in small collections like these (e.g. Gouliermis 2018; Ward et al. 2020, and references therein) and they will eventually disperse into the Galactic field. At the other extreme, a much smaller proportion (5 – 10%) are located in bound clusters, like young massive clusters and low-mass compact clusters (e.g. Krumholz et al. 2019; Krumholz & McKee 2020, and references therein).

At early evolutionary times, however, there remain great unknowns in the shaping of star-forming regions (see Motte et al. 2018 for a recent review). Two main scenarios have been proposed: (1) "monolithic" collapse, whereby stars are born *in situ*, out of a single molecular cloud core; and (2) "hierarchical" merging — gas collapses to form small, individual stellar groups which combine to form a larger cluster. In recent years, the evidence has been very much in favour of the latter scenario (Sabbi et al., 2012; Longmore et al., 2014; Getman et al., 2019; Vázquez-Semadeni et al., 2019; Wright & Parker, 2019; Krumholz & McKee, 2020), but further tests are needed to conclude the dichotomy (Kuhn et al., 2019).

One way to constrain the evolutionary scenario is through the dynamical study of young stellar systems. Simulations which follow hierarchical assembly have shown

that rotation should be visible in the gas component for young ($t = 1 - 2$ Myr) clusters (Mapelli, 2017). Yet, these findings are difficult to confirm at optical wavelengths, as stars still tend to be obscured by natal dust and gas at these ages. Alternatively, radio observations of the ionised gas of young star-forming regions could serve as a valuable test for hierarchical assembly. This is exemplified in Chapter 2, which explores the possible rotation of an H II region. First, read on for a description of the physics behind such radio measurements.

Probing H II region kinematics with radio recombination lines

With the onset of hydrogen burning in OB stars ($M_\star > 8\ M_\odot$), vast amounts of highly energetic UV photons are released. These photons, with $h\nu > 13.6$ eV, ionise the surrounding neutral hydrogen (H I) gas, hence the term H II region. The H II region expands up to the Strömgren (1939) radius, where the ionisation and recombination rates become balanced. Recombination is the process by which free electrons and hydrogen ions recombine, and form a hydrogen atom in a highly energised state. The atom quickly cascades down to the ground level by emitting photons which we observe as emission line spectra; $n \rightarrow n-1$ transitions produce lines with the highest intensity. For transitions from high principal quantum numbers ($n \geq 85$), the emission lines are detected at centimetre (cm) wavelengths. Analogous to this, millimetre (mm) radio recombination lines (RRLs) occur for $28 \gtrsim n > 85$, and so on.

Initial debates regarding the detectability of RRLs were heated (Gordon & Sorochenko, 2002). Numerous works agreed that RRLs should be undetectable (van de Hulst, 1945; Reber & Greenstein, 1947; Wild, 1952) until Kardashev (1959) predicted that RRLs should be visible at infrared to decimetre wavelengths. Kardashev's prediction was soon confirmed by multiple RRL detections originating from the brightest H II regions in the sky, such as the Omega Nebula (Hoglund & Mezger, 1965; Sorochenko & Borodzich, 1966; Dravskikh & Dravskikh, 1967).

RRL surveys have since highlighted the existence of many new H II regions, unobservable by optical surveys (e.g. Mezger & Hoglund 1967; Dieter 1967; Reifenstein et al. 1970; Wilson et al. 1970; Caswell & Haynes 1987b; Lockman 1989; Lockman et al. 1996; Bania et al. 2010, 2012; Anderson et al. 2011, 2015, 2018;

Wenger et al. 2019). As radio telescopes increased in sensitivity and resolving power, smaller and denser H II regions began to appear, known as compact H II regions (e.g. Mezger et al. 1967; Wink et al. 1982; Aliakberov et al. 1985; Giveon et al. 2005a,b). Increasingly compact regions continued to emerge, along with two new definitions: ultracompact (UC), and hypercompact (HC) H II regions (Table 1.1).

Region type	d [pc]	n_e [cm^{-3}]	N
Hypercompact[a]	$\lesssim 0.05$	$\gtrsim 10^6$	16[d]
Ultracompact[b]	$\lesssim 0.15$	$\gtrsim 10^4$	~ 600[e]
Compact[c]	$\lesssim 1.00$	$\gtrsim 5\times10^3$	$\gtrsim 100$[f]
Classical	$\lesssim 10$	$\gtrsim 100$	$\gtrsim 750$[f]

Table 1.1: Physical parameters of H II regions, including size (d), electron density (n_e), and the number of currently known Milky Way regions for each category (N).
References: (a) Kurtz (2002); (b) Habing & Israel (1979); (c) Mezger et al. (1967); (d) Yang et al. (2019); (e) Urquhart et al. (2013b); (f) rough estimates based on the WISE catalogue (Anderson et al., 2014).

Since H II regions trace areas of active star formation, RRLs are invaluable for modelling the large-scale structure of the Galaxy and the location of its spiral arms (Figure 1.9; Georgelin & Georgelin 1976; Taylor & Cordes 1993). Similarly, molecular maser emission lines — also observed at radio wavelengths — can be used to measure line-of-sight velocities, and therefore kinematic distances[17], to high-mass star-forming regions (e.g. Churchwell et al. 1990; Reid et al. 2009, 2014, 2019). Masers are also useful for probing the internal kinematics of an H II region, since they tend to trace hot, dense molecular gas found in close proximity to high-mass protostars (see Hunter et al. 2018 and references therein).

The full width at half maximum (FWHM) of a RRL reveals additional information about the kinematics of an H II region. Three main physical mechanisms contribute to RRL broadening[18]:

1. thermal (Doppler) broadening;
2. pressure/collisional (Stark) broadening, caused by high electron densities; and

[17] When the radial velocity of an H II region is known, its distance can be calculated based on the kinematics (i.e. rotation curve) of the Galaxy.
[18] Natural broadening would be a fourth contributing factor, but is negligible for RRLs.

3. dynamical broadening, due to macroscopic gas motions e.g. large-scale turbulence, rotation, expansion, inflows or outflows, shocks, and jets.

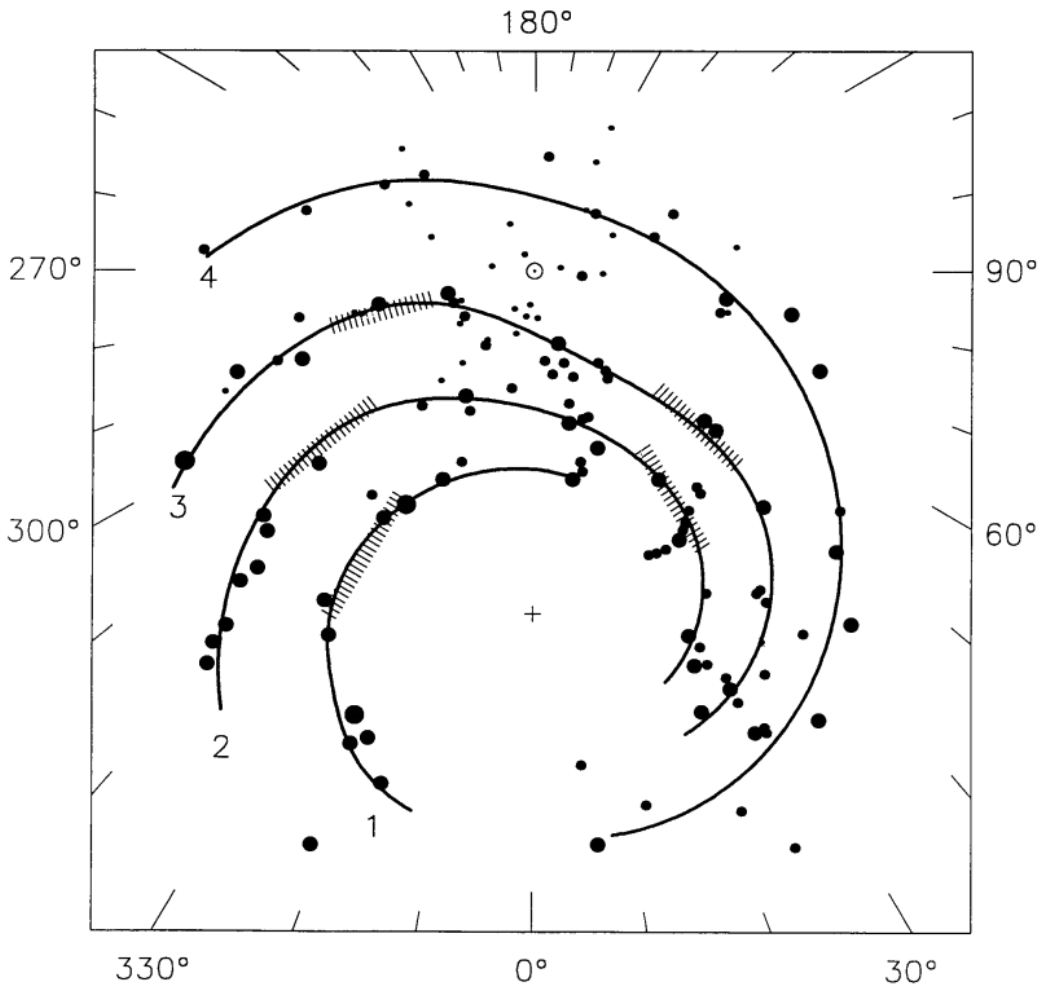

Figure 1.9: A Milky Way model originally proposed by Georgelin & Georgelin (1976). H II regions are depicted by full circles; spiral arms are represented by solid lines; intensity maxima in the radio continuum and neutral hydrogen are shown by hatched areas; the cross and open circle with a dot correspond to positions of the Galactic centre and Sun, respectively. Reproduced from Taylor & Cordes (1993), Figure 1.

Pressure broadening dominates the line widths of cm-RRLs, but no longer contributes at mm wavelengths (Gordon & Sorochenko, 2002). Thus, studies have looked to mm-RRLs to probe the intrinsic motions and physical properties of H II regions more easily (Sewiło et al., 2008; Keto et al., 2008; Galván-Madrid et al., 2012; Kim et al., 2017; Klaassen et al., 2018). Line widths of 20 – 30 km/s are expected for mm-RRLs, so it came as a surprise when Altenhoff et al. (1981) reported a 50 km/s line width for the UC H II region, MWC 349. Less than 20 broad recombination line objects (BRLOs)

have since been found (e.g. Shepherd et al. 1995; Gaume et al. 1995; de Pree et al. 1996, 1997, 2004; Johnson et al. 1998; Jaffe & Martín-Pintado 1999; Sewiło et al. 2004; Zhang et al. 2014; Kim et al. 2017).

Jaffe & Martín-Pintado (1999) explored several models to try and explain the BRLO phenomenon — i.e. ionised outflows, disc winds, bow shocks, champagne flows, or inflows — yet the exact underlying cause is often unknown. In order to disentangle the different dynamical mechanisms at play, observations with higher spatial resolution, as well as complementary molecular gas and maser observations, have proved to be very beneficial (e.g. Moscadelli et al. 2018). Observations of the macroscopic motions of star-forming regions is covered in greater detail in the following Section. Chapter 2 then focuses on the study of one H II region in particular — G316.81–0.06 — whereby RRL analysis presents a strong case for rotation.

1.2.2 The dynamical evolution of globular clusters

Globular clusters (GCs, or globulars) are collections of gravitationally bound stars. They come in many varieties, and can be grouped according to age, size, density, chemistry, location, rotation, relaxation time, and more. GCs provide further opportunities for probing the evolution of stars and galaxies. They are relatively simple objects; self-gravitating, isolated systems containing roughly 10^5–10^6 stars all of similar age and chemical composition.

GC dynamical evolution occurs on much shorter timescales than the Hubble time, by a factor of 10–10^3. This is significantly less than galaxy dynamical evolution timescales, and thus, globulars are ideal laboratories for the study of dynamical phenomena. These dynamical processes are driven from within (via two-body relaxation, mass segregation, and core collapse for example), as well as externally (e.g. due to the Galactic tidal field), as described in further detail below.

Dynamical evolution due to internal and external effects

One way to improve our understanding of GCs and how they evolve is through the study of a cluster's internal kinematics, which is influenced by internal and external

processes. Internally, stars interact and scatter off one another — known as two-body relaxation — as the system converges toward thermal equilibrium. When all stars have lost the memory of their initial orbits, the cluster has reached dynamical relaxation (Spitzer, 1987). This process occurs on timescales of 10^8–10^{10} years and is the driving force of cluster evolution in the long-term (Binney & Tremaine, 2008).

Two-body interactions also lead to other processes like mass segregation and core collapse. When two bodies scatter, they exchange energy in order to equalise the kinetic energy between the different masses, i.e. they evolve towards equipartition (Spitzer, 1969). More massive stars have lower velocities and sink towards the cluster core, while lighter, faster moving stars drift outwards — or escape, if their velocity exceeds the escape velocity of the cluster. Stellar evaporation occurs on the order of the relaxation timescale (Davies, 2013).

Mass segregation has been observed in several globular clusters. Since the launch of the *Hubble Space Telescope* (*HST*) — and later, with the *Very Large Telescope* (*VLT*) — it has been possible to resolve individual stars within a cluster's core. Photometric studies can determine how a stellar population varies with radius; Table 1.2 lists several examples where mass segregation has been detected.

As more massive stars sink to the core and less massive stars migrate to the cluster halo, the core becomes energetically hotter and the halo cooler. Since a self-gravitating system has negative heat capacity, energy flows from the hot core to the cool halo via two-body scattering, and the core contracts (e.g. Gieles et al. 2011, and references therein). This is known as gravothermal instability (a term coined by Lynden-Bell & Wood 1968). In combination with mass segregation, the core tends toward collapse.

The collapsed core phenomenon had been theoretically predicted by Hénon (1961, 1965) and Lynden-Bell & Wood (1968) long before it was ever observed. Two decades later, Djorgovski & King (1986) studied 113 globulars at the Lick Observatory; they combined their results with previous literature and found that at least 21 of 123 GCs showed bright surface brightness power-law cusps, i.e. a sign that the cluster has undergone core collapse (see Figure 1.10).

As a core collapses, an injection of energy is required to prevent the central stellar density tending to infinity. Heggie (1975) and Stodolkiewicz (1986) were some of

GC name	Also known as	Location	References
Hodge 14		LMC	Kerber & Santiago (2006)
NGC 104	47 Tucanae	MW	Paresce et al. (1995); Anderson (1997)
NGC 1805		LMC	Kerber & Santiago (2006)
NGC 1818		LMC	Kerber & Santiago (2006)
NGC 1831		LMC	Kerber & Santiago (2006)
NGC 1868		LMC	Kerber & Santiago (2006)
NGC 5466		MW	Sollima et al. (2017)
NGC 6218		MW	Sollima et al. (2017)
NGC 6341	M 92	MW	Anderson (1997); Andreuzzi et al. (2000)
NGC 6397	Caldwell 86	MW	King et al. (1995); Andreuzzi et al. (2004); Martinazzi et al. (2014)
NGC 6656	M 22	MW	Albrow et al. (2002)
NGC 6752		MW	Shara et al. (1995); Ferraro et al. (1997)
NGC 6981		MW	Sollima et al. (2017)
NGC 7078	M 15	MW	de Marchi & Paresce (1996); Sosin & King (1997)
NGC 7099	M 30	MW	Sosin (1997)
Palomar 5		MW	Koch et al. (2004)
Palomar 14	Arp 1	MW	Frank et al. (2014)

Table 1.2: Evidence for mass segregation in globular clusters.

the first to investigate how the existence and creation of binaries in high-density environments can counteract collapsing cores. They found that primordial binaries, and the creation of new stellar pairs, are key in the post-core-collapse process: (1) As a binary system scatters a passing star, the binary becomes more bound and the lone star receives a velocity kick; (2) Three unbound bodies can interact to create a binary, and the remaining star carries away the excess energy. Both result in the injection of energy to the cluster core, offsetting the loss of energy to the halo.

As binaries allow the cluster to regulate itself against core collapse, binary heating then drives the core to expand. When the core comes into contact with the cooler cluster halo, energy transfers outwards again, re-initiating gravothermal collapse — this process repeats itself, and are called gravothermal oscilliations. First predicted by Sugimoto & Bettwieser (1983), these cycles have since been seen in numerous

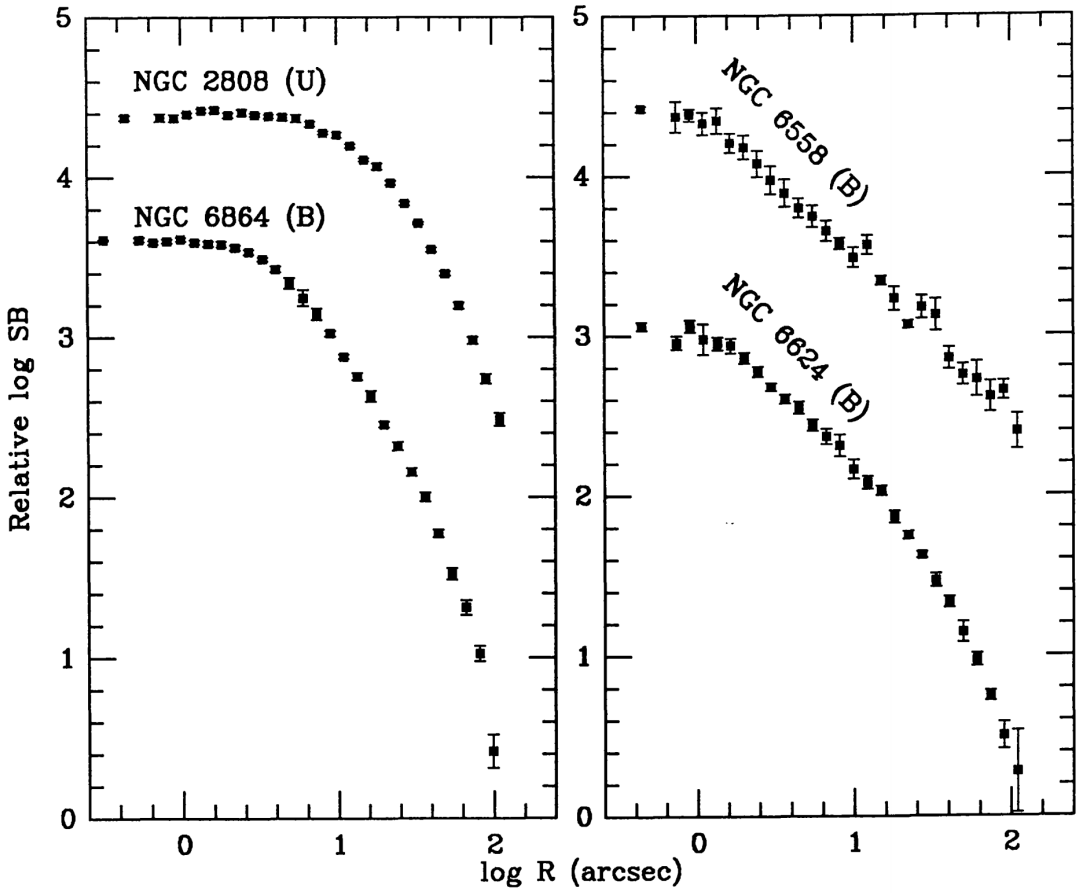

Figure 1.10: Surface brightness profiles of globular clusters: flat cores (left) and power-law cusps (right). The latter implies that the GC has undergone core collapse. Reproduced with permission from Djorgovski (1988), Figure 4.

simulations: Fokker-Plank (Gao et al., 1991); *N*-body (Makino, 1996); and Monte Carlo (Fregeau et al., 2003; Heggie & Giersz, 2008).

Binaries may also help to retain exotic objects. Neutron stars and stellar-mass black holes are expected to receive natal kicks when they form, expelling them from the cluster. If a newly formed relic is bound to a companion star, its speed will be greatly reduced, thus increasing its chances of remaining within the GC (Davies, 2013). Despite this, for many years it was thought that black hole populations should be heavily depleted, ejected via scattering between binaries and lone stars (see e.g. Morscher et al. 2013, and references therein).

However, recent theoretical and computational analyses have demonstrated that the rapid evaporation of black holes is false (e.g. Morscher et al. 2015). This is further supported by several observations of black holes (e.g. Strader et al. 2012; Chomiuk

et al. 2013; Shishkovsky et al. 2018; Giesers et al. 2018). Hence, the existence of stellar-mass BH candidates implies that GCs retain higher numbers of black holes than previously thought.

In addition to GC mass-loss caused by internal two- or three-body interactions, the loss of mass can be accentuated by Galactic tidal fields. With increasing proximity to the Galactic disc or bulge, outer stars are stripped away from the cluster halo, accelerating the rate of stellar evaporation. Using N-body calculations — which take into account mass-loss due to stellar evolution, two-body relaxation, and an external tidal field — Baumgardt & Makino (2003) predicted that 53–67% of all Galactic globulars will be destroyed within the next Hubble time.

Other external influences include passing through the Galactic disc (Ostriker et al., 1972) or near the bulge (Spitzer, 1987) which causes gravitational shocks. This means that stars in the cluster halo become heated, and as they become stirred up they evaporate more quickly (Madrid et al., 2017). This is supported by observational evidence: more centrally located GCs have smaller and denser cores (Djorgovski & Meylan, 1994).

Stellar velocities and the construction of velocity dispersion profiles

Kinematic data reveal ample information on the internal properties of globular clusters, but for most of the 20$^{\text{th}}$ century progress was hindered by many obstacles. Data collection was a tedious and arduous process, and greatly limited by magnitude (Table 1.3). Many velocities came with large uncertainties (on the order of ~ 10 km/s) and were unsuitable for analyses of the internal dynamics, given that clusters have velocity dispersions down to ~ 1 km/s. These challenges made it difficult to constrain dynamical models, which depend on the construction of accurate density[19] and velocity dispersion profiles.

Velocity dispersion profiles can be constructed from three different types of data: stellar velocities, integrated-light spectra, or proper motions[20]. With respect to

[19] Density profiles are built from star counts or surface brightness measurements. See e.g. Oort & van Herk 1959; King et al. 1968; Illingworth & Illingworth 1976; Trager et al. 1995; McLaughlin & van der Marel 2005; Miocchi et al. 2013; Saracino et al. 2015.

[20] Proper motions provide more dynamical information than radial velocities alone, since

Spectrograph	Star cluster	N_{stars}	M_V [mag]	Errors [km/s]	Literature
Long-slit	NGC 2264 (OC)	12	$\lesssim 10$	1	Trumpler (1935)
Long-slit	Pleiades (OC)	71	$\lesssim 10$	$\sim 1-12$	Smith & Struve (1944)
Long-slit	NGC 6341 (GC)	15	–	$\sim 1-3$	Wilson & Coffeen (1954)
Long-slit	NGC 104 (GC)	32	$\lesssim 13$	–	Feast & Thackeray (1960)
Long-slit	NGC 6397 (GC)	11	$\lesssim 11$	$\sim 1-3$	Da Costa et al. (1977)
Long-slit	NGC 5272 (GC)	111	$\lesssim 14$	~ 1	Gunn & Griffin (1979)
Long-slit	NGC 7078 (GC)	120	$\lesssim 14.5$	~ 1	Peterson et al. (1989)
Long-slit	NGC 5139 (GC)	471	$\lesssim 14$	~ 1	Mayor et al. (1997)
MOS	NGC 6121 (GC)	2469	$\lesssim 17.5$	~ 1	Sommariva et al. (2009)
IFS	NGC 6397 (GC)	12,307	$\lesssim 20.0$	~ 1	Husser et al. (2016)

Table 1.3: The evolution of spectroscopic observations in terms of number of stars observed, absolute magnitude, and uncertainties. Some values have not been listed in the papers. Improvements occurred as larger telescopes were built in combination with the development of advanced spectrographs and cross-correlation techniques.

stellar velocities, significant advances came with the development of cross-correlation techniques. The pioneering works of Fellgett (1955), Griffin (1967) and Simkin (1974) showed that cross-correlation of a stellar spectrum with a template reduced velocity errors by more than an order of magnitude. Further advances followed with the construction of 4-metre telescopes in the seventies, and as charge coupled devices (CCDs) became more widely available in the eighties. At the turn of the century, fibre-fed multi-object spectrographs (MOS; e.g. Cote et al. 1994; Soderberg et al. 1999; Reijns et al. 2006; Sommariva et al. 2009) enabled greater numbers of stars to be observed over shorter exposure times. MOS observations are restricted to the outer regions, however, as they are easily contaminated by nearby, brighter, stars.

Despite these advances, stars located in a cluster's crowded centre remained inaccessible. Without kinematic data from the core, theories on dynamical evolution — such as core collapse — could not be tested (Elson et al., 1987a). Instead, the broadening of integrated-light spectra were used to produce central velocity dispersions for tens of galactic GCs (Illingworth, 1976; Zaggia et al., 1992; Dubath et al., 1993). This method is not ideal, however, as slits containing too few stars lead to large uncertainties and a spectrum can easily become dominated by a single star

they are two-dimensional. See e.g. van Leeuwen et al. (2000); McLaughlin et al. (2006); Anderson & van der Marel (2010); D'Souza & Rix (2013); Bellini et al. (2014, 2017); Libralato et al. (2018); Sollima et al. (2019).

(Dubath et al., 1997; Lanzoni et al., 2013)[21]. As such, Dull et al. (1997) and van der Marel et al. (2002) tried alternative methods, such as stepping observations across the crowded field with a long-slit spectrometer, but it was inefficient, consumed too much valuable telescope time, and blending due to unresolved stars was a significant issue. In contrast, a scanning technique using Fabry-Pérot interferometers (Gebhardt et al., 1995, 1997, 2000) showed greater promise — reaching high spectral resolution and extracting radial velocity information more accurately — but it was still very expensive time-wise.

Since then, integral-field spectrographs (IFS) have taken the spotlight, opening up many new possibilities for the study of star cluster kinematics. Integral-field data provide radial information for dynamical models and it means that rotation and escaping stars can be detected and quantified. Binary stars can also be found (assuming multi-epoch observations are available).

Conceived by Vanderriest (1980) and Courtes (1982), IFS perform 3D-spectroscopy of crowded fields within a single integration, whereby each pixel is associated with one full spectrum. This drastically reduces systematic noise, and makes it possible to acquire spectra of fainter, main-sequence stars in the innermost cluster regions for the first time. One of the first IFS studies of GCs[22] was carried out with the PMAS at Calar Alto, with the aim to place stringent mass limits on possible intermediate-mass black holes (Kamann et al., 2014). The authors obtained stellar velocities for 225 stars within the central $\sim 10''$ of M3, M13, and M92, with uncertainties ≤ 1 km/s. This dataset anticipated MUSE's first light in 2014, when Husser et al. (2016) yielded spectra for more than $10,000$ stars, reaching I-band magnitudes as high as 20 mag, using an integration time of only 95 minutes. MUSE has been the driving force behind several more kinematic studies — including Kamann et al. (2016, 2018a, 2020) and Giesers et al. (2018, 2019) — which explore dynamical topics ranging from rotation to binaries to the first radial velocity discovery of a stellar mass black hole. Now that MUSE has recently gained adaptive optics (AO) capabilities, even further advances are on the horizon (Leibundgut et al., 2019).

[21] On the other hand, integrated-light spectra is well suited to determining the velocity dispersions of extra-galactic GCs (see e.g. Strader et al. 2011).

[22] More specifically, Kamann et al. (2014) were the first to incorporate PSF-fitting into the analysis of GC IFU data.

With IFS and AO the collection of data has increased tenfold, yielding higher accuracies, greater sensitivities, and shorter integration times. Ultimately, this improves velocity dispersion measurements for which quantities like mass and the mass-to-light ratio depend (see Chapter 3). This new technology also creates a clearer picture of star clusters in the Magellanic Clouds, initiating dynamical studies of younger SCs in more detail than ever before.

1.2.3 Magellanic Cloud star clusters

Young and high-mass star clusters ($M \gtrsim 10^4$ $M_\odot$) are believed to be globular progenitors (de Grijs, 2009). If true, this presents a unique opportunity to observe GCs in their youth and to reveal insights to the evolutionary processes and conditions required for star (cluster) formation. SCs located in the Milky Way's satellite galaxies, the Large and Small Magellanic Clouds, serve as excellent laboratories for testing dynamical theories at younger times. The MCs are nearby ($\sim$ 50 and $\sim$ 60 kpc, respectively), hence they are close enough to be able to resolve the constituent stars. In addition, MC properties cover a wide range of ages, metallicities, and sizes, etc. — regions of parameter space can be probed which are otherwise nonexistent in the MW. Thus, with modern day instruments it is possible to provide much needed constraints on cluster models over cosmic time (Santiago, 2009).

The MCs contain at least 3740 star clusters[23] (Bica et al., 2008); $\sim$ 150 have masses analogous to MW GCs (Mackey, 2009), with metallicities spanning across $\sim$ 2 dex ($-2.5 <$ [Fe/H] < -0.5 dex; Beasley 2020). Unlike MW globulars, the MCs contain massive star clusters younger than 9 Gyr, divided between two categories: intermediate-age clusters (IACs) aged $2 < t < 9$ Gyr, and young massive clusters (YMCs) aged 1 Myr – 2 Gyr. Some of the most studied clusters are included in Table 1.4, but this is by no means an exhaustive list. The star formation histories of the two Clouds are quite different, however (Weisz et al., 2013; Rezaeikh et al., 2014; Gallart et al., 2015). Star clusters in the SMC appear to have formed continuously over the past 10.5 Gyr, whereas LMC SCs have ages distributed between three main epochs:

[23] For the latest catalogue of star clusters in the SMC and the Magellanic Bridge, see Bica et al. (2020). LMC catalogue in prep.

	SMC	LMC
GC	N 121	Hodge 11, N 1466, N 1754, N 1786, N 1835, N 1841, N 1898, N 1928, N 1929, N 1939, N 2210, N 2257, R136, Reticulum
IAC	K 28, K 44, L 1, L 7, L 8, L 19, L 27, L 110, L 113, N 339, N 361, N 416	N 1856, N 1978, ESO 121-SC3
YMC	L 106, L 114, N 152, N 222, N 256, N 269, N 294, N 330, N 411, N 419, N 458, N 643, N 796	N 1693, N 1695, N 1698, N 1704, N 1711, N 1755, N 1772, N 1782, N 1783, N 1793, N 1805, N 1815, N 1818, N 1831, N 1846, N 1847, N 1850, N 1866, N 1890, N 1916, N 2004, N 2005, N 2019, N 2031, N 2095, N 2100, N 2136, N 2137, N 2154, N 2157, N 2159, N 2160, N 2164, N 2172, N 2249

Table 1.4: Examples of massive clusters in the Small and Large Magellanic Clouds, specifically globular clusters ($t > 9$ Gyr), intermediate-age clusters ($2 < t < 9$ Gyr), and young massive clusters ($t \lesssim 2$ Gyr). K ≡ Kron; L ≡ Lindsay; N ≡ NGC; R ≡ RMC.

> 9 Gyr; 3 – 4 Gyr; and < 1 Gyr, with an age-gap between 4 – 9 Gyr (Glatt et al., 2010).

Similar to Galactic GC studies, the first structural parameter analyses of MC clusters were derived by counting stars and constructing surface brightness profiles (Kontizas et al., 1982; Elson et al., 1987b, 1989a; Mateo, 1988; Elson, 1991, 1992). Similar star count studies have continued to this day, for high-mass (Dias et al., 2014; Piatti & Mackey, 2018; Lanzoni et al., 2019) and low-mass ($M \lesssim 10^4$ $M_\odot$) clusters (Maia et al., 2014, 2019). There have also been a number of dynamical studies of old- and intermediate-age LMC clusters based on integrated spectra (Elson & Freeman, 1985; Mateo, 1989; Dubath et al., 1990; Meylan et al., 1991).

One study found something unexpected: the appearance of a spread of cluster core radii with an increase in age (Elson et al. 1989b; Figure 1.11). Subsequent observations with the HST revealed the same relationship (Mackey & Gilmore, 2003a,b). Many studies tried to explain the trend, exploring effects due to binaries; tidal fields; low number statistics; remnants; and primordial mass segregation, but on the whole, were inconclusive (Wilkinson et al., 2003; Hunter et al., 2003; Merritt et al., 2004; Mackey et al., 2008). The most promising explanation thus far has been illustrated by Ferraro et al. (2019) — they suggest that looser systems are not visible at young

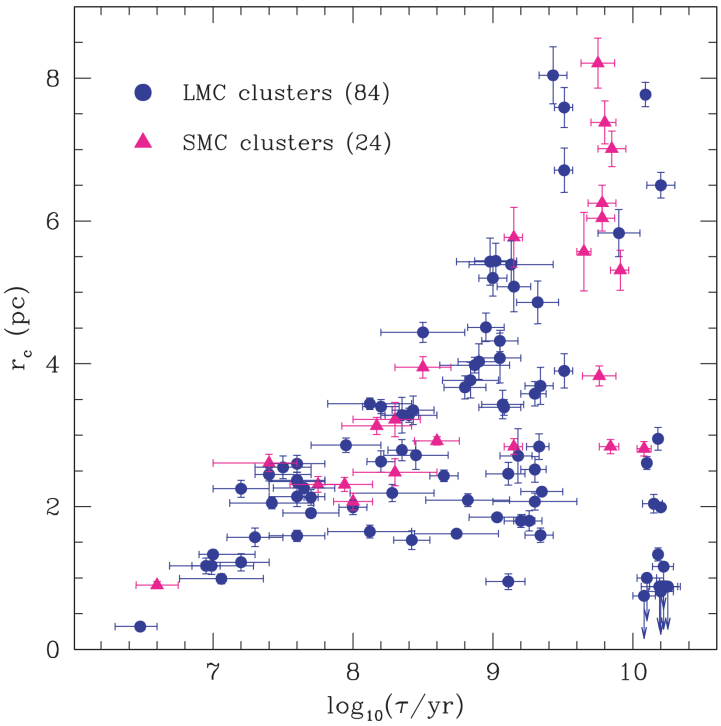

Figure 1.11: Core radii versus age for LMC and SMC massive star clusters. Reproduced from (Mackey et al., 2008), Figure 1.

ages because they are quickly destroyed. Older clusters, on the other hand, portray a range of core radii for the same reasons that Galactic GCs do: (1) they foster different initial properties at cluster formation, and (2) they exhibit different dynamical ages, depending on their current stage of internal evolution (see Section 1.2.2). Future IFS studies (e.g. with MUSE) will soon allow us to test some of the proposed explanations directly, by searching for black holes, for example.

In summary, star clusters in the MW and its satellites are ideal laboratories for probing the dynamical evolution of stellar systems; we have come a long way since the invention of spectroscopy and photography in the 19th-century (Section 1.1.2). Since then, instrumentational and technical developments have increased our capacity to examine the internal kinematics of clusters in exquisite detail. Using this newfound technology, this thesis aims to provide much-needed constraints on theoretical models, while highlighting new areas for further investigation, from radio observations of star-forming regions (Chapter 2) to IFS studies of globulars (Chapter 3) and YMCs (Chapter 4). There is also much to look forward to with the construction of new integral field units, particularly in the infrared (Chapter 5).

Chapter 2

A rotating H II region?

Regions of lucid matter taking forms,
Brushes of fire, hazy gleams,
Clusters and beds of worlds, and bee-like swarms
Of suns, and starry streams. Alfred Lord Tennyson

2.1 Introduction

Feedback from high-mass stars (i.e. OB stars with $M_\star \geq 8\ M_\odot$) is fundamental to the shaping of the visible Universe. From the moment star formation begins, stellar feedback commences, injecting energy and momentum into the natal environment. This feedback can both hinder and facilitate star formation; negative feedback restrains or can even terminate star formation, whereas positive feedback acts to increase the star formation rate and/or efficiency. Many different physical mechanisms contribute to feedback by varying degrees, each depending on a variety of factors (e.g. initial conditions), resulting in an intricate and interdependent series of processes. In a recent review on this topic, Krumholz et al. (2014) groups feedback processes into three main categories: momentum feedback (e.g. protostellar outflows and radiation pressure); "explosive" feedback (e.g. stellar winds, photoionising radiation, and supernovae); and thermal feedback (e.g. non-ionising radiation).

Stellar feedback encompasses many astrophysical processes, moderating star formation from stellar scales ($\ll$ 1 pc) to cosmological kpc-scales (e.g. driving Galactic outflows; Murray et al. 2011; Girichidis et al. 2016). Despite our growing knowledge of these processes, the overarching interplay between them remains uncertain. Observationally, limited spatial resolution makes it difficult to disentangle the effects of each feedback mechanism which all operate simultaneously. Other additional factors, such as the role of magnetic fields (for which the strength and orientation are difficult to measure) and feedback from surrounding low-mass stars, complicate the process further. Moreover, limited observations of the earliest stages of high-mass star formation means that the large samples needed for a robust statistical analysis are lacking. With observatories like ALMA and the EVLA, which have sufficient angular resolution to resolve and detect individually forming high-mass stars, our understanding is continually improving.

Meanwhile, in the past few decades, there have been considerable efforts attempting to simulate the vast range of stellar feedback effects. It has been clearly demonstrated that without feedback, simulations fail to replicate the galaxies that we observe in the Universe today (e.g. Katz et al. 1996; Somerville & Primack 1999; Cole et al. 2000; Springel & Hernquist 2003; Kereš et al. 2009; Girichidis et al. 2011; Kennicutt & Evans 2012; Scannapieco et al. 2012; Hopkins et al. 2014; Peters et al. 2017) and often produce galaxies that are much more massive than observed. Consequently, simulations have looked to feedback for answers, with promising results. Yet it remains a great challenge to create a model which includes all feedback processes over a vast range of scales. Often only one or two types of feedback are included (e.g. Krumholz et al. 2010; Myers et al. 2011; Dale et al. 2013; Agertz et al. 2013; Kim et al. 2013; Peters et al. 2014; Tasker et al. 2015; Muratov et al. 2015; Agertz & Kravtsov 2016; Butler et al. 2017; Núñez et al. 2017). In order to improve simulations and implement more feedback effects, better understanding of the relevant physical processes is needed. This will help to provide the observational constraints needed for parameterising simulations.

2.1.1 H II regions

The study of H II regions can allow us to explore how high-mass stars impact their environment via the aforementioned feedback mechanisms. H II regions are bright in the radio regime, particularly with radio recombination lines (RRLs) and thermal bremsstrahlung, both clear diagnostics of high-mass star formation. See Haworth et al. (2018) for a review on synthetic observation studies, particularly regarding feedback and the global structure of H II regions.

Predominantly, the study of H II regions has focused on surveys examining morphologies, sizes and densities (e.g. Helfand et al. 2006; Hoare et al. 2012; Urquhart et al. 2013a,b; Kim et al. 2017; Giannetti et al. 2017). In terms of morphology, ultracompact (UC; $\lesssim 0.15$ pc) H II regions can be categorised as either spherical, cometary, core-halo, shell, or irregular (Wood & Churchwell, 1989)[1]. The authors found that too many UCH II regions are observed considering their short apparent lifetime, which became known as the 'lifetime debate'. Peters et al. (2010b) have proposed a solution based on their synthetic radio continuum observations of young high-mass star formation regions: H II regions 'flicker' as they grow, due to a fluctuating accretion flow around the high-mass star (fragmentation-induced starvation; Peters et al. 2010a, hereafter P10). This is a possible resolution to the lifetime problem since the young H II regions shrink and grow rapidly as they evolve. Short (several year) variations in the flux density of the high-mass star forming region Sgr B2 have been observed (de Pree et al., 2014, 2015), which the authors attribute to 'flickering'.

There have also been detailed studies on the kinematics of H II regions on (proto)stellar scales ($\lesssim$ 10,000 AU). This includes the accretion of ionised material onto forming high-mass stars (e.g. Keto et al. 1988; Keto & Klaassen 2008; Sollins et al. 2005; Keto & Wood 2006; Keto 2002, 2003, 2007; Galván-Madrid et al. 2008; Klaassen et al. 2018); the gravitational collapse and rotation of turbulent molecular clouds (e.g. Klessen et al. 2000; Klaassen et al. 2009); ionised outflows (e.g. de Pree et al. 1994; Klaassen et al. 2013; Tanaka et al. 2016); and the rotation of ionised gas on

[1] de Pree et al. (2005) later modified the classification scheme to also include bipolar morphologies.

stellar scales (e.g. Rodriguez & Bastian 1994; Sewiło et al. 2008).

However, to date, fewer studies have been devoted to measuring the ionised gas kinematics of H II regions on cloud scales ($\sim$ 0.1 pc), pertinent to understanding the effect of feedback of high-mass stars on their natal clouds. Instead, most studies focus on understanding the kinematics of cometary H II regions in order to deduce which model (e.g. bow shock or champagne) applies. This is often done via the analysis of velocity ranges or gradients of the ionised gas (e.g. Lumsden & Hoare 1996, 1999; Veena et al. 2017). Intriguingly, G34.3+0.2, G45.07+0.13 and Sgr B2 I and H all show velocity gradients (from 10-35 km s^{-1}), perpendicular to the axis of symmetry of the cometary H II region (Garay et al., 1986; Gaume & Claussen, 1990; Gaume et al., 1994; Immer et al., 2014).

The velocity gradients of other H II region morphologies, however, could present new interpretations on our understanding of feedback. In particular, bipolar H II regions are at the earliest evolutionary stages of an H II region, where ionisation has only recently begun to occur (e.g. Battersby et al. 2010). Newly ionised material flows outwards with velocities up to 30 km s^{-1} (Deharveng et al., 2015) and neutral material (usually in the form of a molecular disc) lies perpendicular to the outflows, often showing signs of accretion towards a central (proto)star. When viewed approximately edge-on, the H II region appears as bipolar. Velocity gradients within the ionised gas will typically correspond to infall, outflow, rotation or a combination, which will be influenced by the viewing angle. This can have different implications on feedback depending on which motion truly occurs.

In this chapter, I present observations of a young, bipolar H II region, G316.81–0.06. The results show a velocity gradient in the ionised gas at 0.1 pc scales, perpendicular to the bipolar axis. In conjunction with the P10 simulations, I aim to understand the origin of the velocity structure in the ionised gas and its relation to feedback. Section 2.2 describes the observations and simulations in more detail, followed by the data analysis in Section 2.3. The results and discussion are in Sections 2.4 and 2.5, concluding with a summary in Section 2.6.

2.2 Data

2.2.1 Observations

Figure 2.1 illustrates multi-wavelength images of G316.81–0.06, located 2.6 kpc away in the Galactic Disc (Green & McClure-Griffiths 2011; note that this is a newer distance estimate as opposed to the measurement of 2.7 kpc used in previous literature). Various authors have discussed the kinematic distance ambiguity in relation to this source (Shaver et al., 1981; Busfield et al., 2006; Hou & Han, 2014), and conclude it is at the near kinematic distance.

The top infrared (IR) image of Figure 2.1 is a *Spitzer* GLIMPSE/MIPSGAL image in the 3.6, 8.0, and 24.0 micron IRAC bands (Benjamin et al., 2003; Churchwell et al., 2009; Carey et al., 2009; Gutermuth & Heyer, 2015; Christensen et al., 2012). On the bottom-right a close-up of G316.81–0.06 is shown, of the same GLIMPSE/MIPSGAL image. The region is enlarged further in the bottom-left; a mid-infrared (MIR; 3.6, 4.5, and 8.0 microns) GLIMPSE image.

On large scales, strong absorption is featured roughly SE-NW in both IR images due to the presence of an infrared dark cloud (IRDC; e.g. Egan et al. 1998), namely the G316.75 ridge (Watkins et al., 2019a). Emission features (MIR bright bubbles) are seen to the north and south, with one distinct and bright MIR central source found at the apex of these two bubbles. Using the *Australian Telescope Compact Array (ATCA)*, two radio continuum sources classified as UCH II regions in Walsh et al. (1997, 1998) are overlaid with red contours (bottom-left image) showing the 35-GHz free-free continuum emission (Longmore et al., 2009). The left-hand source (Region 1), shows two distinct lobes elongated roughly NE-SW. The continuum data were taken in addition to the H70α RRL with a compact antenna configuration (12.5″ angular resolution) and thus, spatial filtering is not a major issue (see Longmore et al. 2009 for further details).

Region 1 has many more significant features. Numerous masers — hydroxyl, class II methanol, and water — have been detected (see Appendix A.1 for a complete list). For clarity, only the masers listed by Breen et al. (2010b) are marked (bottom-left of

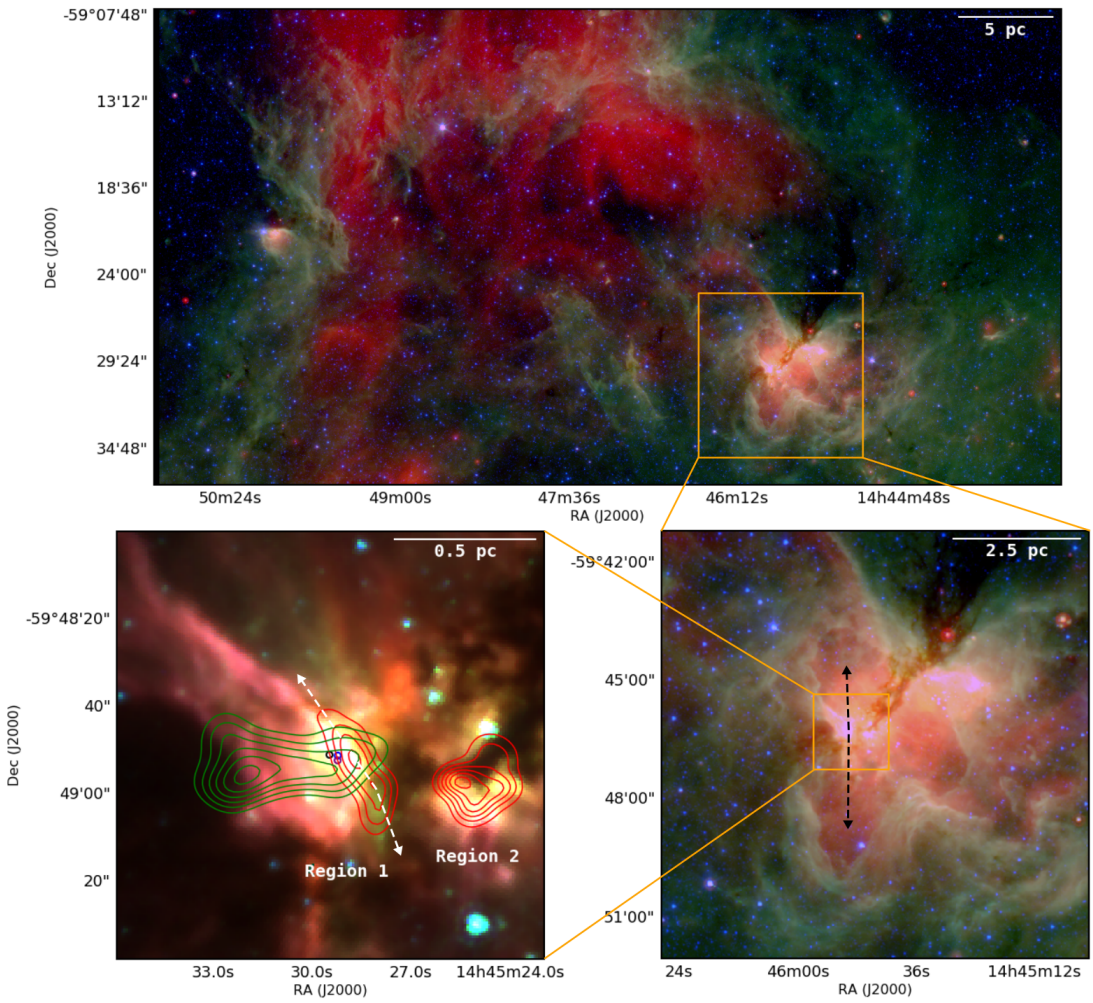

Figure 2.1: Multi-wavelength images of G316.81–0.06. Top and bottom-right: *Spitzer* GLIMPSE/MIPSGAL image in 3.6, 8.0, and 24.0 micron IRAC bands (Benjamin et al., 2003; Churchwell et al., 2009; Carey et al., 2009; Gutermuth & Heyer, 2015; Christensen et al., 2012). The dashed black arrows indicate an outflow in the direction of the two north-south MIR bubbles. Bottom-left: GLIMPSE image in 3.6, 4.5, and 8.0 micron IRAC bands (Benjamin et al., 2003; Churchwell et al., 2009). Red and green contours show the 35-GHz continuum (Longmore et al., 2009) and integrated $NH_3(1,1)$ (Walsh et al., 1997) respectively. Two separate H II regions are labelled Region 1 and 2 accordingly. Masers from Breen et al. (2010b) are depicted as circles: blue (hydroxyl); black (water); purple (methanol). Dashed white arrows indicate the direction of an ionised outflow, aligned with the 35-GHz continuum of Region 1 and the "green fuzzy".

Figure 2.1): blue, purple, and black circles are hydroxyl, class II methanol, and water masers respectively. Ammonia emission (green contours; Walsh et al. 1997) coincides with the three masers, and NH_3 (1,1) shows a clear inverse P-Cygni profile towards the cm-continuum source which extends eastwards from Region 1 and peaks towards the IRDC (Longmore et al., 2007). Other features include 4.5 μm excess emission, i.e. a

"green fuzzy" (otherwise known as an extended green object, EGO; Cyganowski et al. 2008) in the MIR (bottom-left of Figure 2.1; Beuther et al. 2007, 2009).

Overall, G316.81–0.06 is a very complex region, affected by contributions from multiple feedback mechanisms. The aforementioned features can be interpreted as follows: (a) Two MIR bright sources are two separate H II regions (Regions 1 and 2) — formed out of the IRDC filament — which drive the MIR bubbles. It appears as though these cavities have been driven by an older outflow (indicated by the black dashed arrows; bottom-right of Figure 2.1) in a north-south direction, perpendicular to the elongated ammonia emission. (b) Masers indicate youth (class II 6.7-GHz maser emission suggests a possible age of 10-45 kyr; Breen et al. 2010a). (c) The inverse P-Cygni profile implies infall towards Region 1. (d) A more recent outflow is inferred from the presence of the "green fuzzy" (Chambers et al., 2009). In combination with the elongated 35-GHz continuum, the outflow appears to be bipolar, possibly in the form of an ionised jet (indicated by the white dashed arrows; bottom-left of Figure 2.1). In contrast, Region 2 lacks masers and ammonia emission. This implies that Region 2 is older than Region 1, as concluded by Longmore et al. (2007).

2.2.2 Numerical Simulations

To help interpret the data I looked for numerical simulations of young H II regions which match Region 1 as closely as possible. As described in more detail below, I identified the simulations of P10 as having similar global properties to G316.81–0.06 in terms of density, size and cloud mass — the simulations have not been fine-tuned to the observations. While comparisons between the observations and P10 simulations provide a good foundation for further analysis, it would be beneficial to make additional comparisons with a suite of simulations. Such simulations could be fine-tuned to match the observations and model the formation and evolution of H II regions with the same global properties and in the same environment, with a range of different initial conditions. However, this is outside the scope of this analysis.

Given a limited knowledge of G316.81–0.06's history, and with only a single observational snapshot of the region's evolution, it is impossible to know how closely the initial conditions of the P10 simulations are matched to the progenitor gas cloud of

G316.81–0.06. For that reason I have tried to identify general trends in the evolution of the simulations in the hope that the underlying physical mechanisms driving this evolution will be applicable to the largest number of real H II regions. I avoided focusing on detailed comparison of observations to individual (hyper-/ultra-compact) H II regions around forming stars in the simulation, for which the evolution is much more stochastic.

The hydrodynamical simulations of P10 describe the gravitational collapse of a rotating molecular gas cloud to form a cluster of massive stars. The 3D model takes into account heating by ionising and non-ionising radiation using an adapted FLASH code (Fryxell et al., 2000). The synthetic RRL maps of the simulation data are produced using RADMC-3D (Dullemond et al., 2012) as described in Peters et al. (2012). Both local thermodynamic equilibrium (LTE) and non-LTE simulations of H70α emission are run for a total of 0.75 Myr. I have used RRL data corresponding to 730.4, 739.2, 746.3, 715.3 and 724.7 kyr for which an ionised bubble has already emerged.

Summarising Peters et al. (2010a,c), the simulated box has a diameter of 3.89 pc with a resolution of 98 AU. The initial cloud mass is 1000 $M_\odot$, with an initial temperature of 30 K, and core density $3.85{\times}10^3$ cm^{-3}. Beyond the flat inner region of the cloud (0.5 pc radius), the density drops as $r^{-3/2}$. The initial velocities are pure solid-body rotation without turbulence, with angular velocity 1.5×10^{-14} s^{-1}, and a ratio of rotational energy to gravitational energy, $\beta = 0.05$. Sink particles (of radius 590 AU) form when the local density exceeds the critical density, $\rho_{\rm crit} = 2.12 \times 10^8$ cm^{-3} and the surrounding region around the sink particle, $r_{\rm sink} = 590$ AU, is gravitationally bound and collapsing. The sink particles accrete overdense gas that is gravitationally bound, above the threshold density, and within an accretion radius. The accretion rate varies with time and is different for each sink particle. Within the first 10^5 years since the formation of the first sink particle, the original star has accreted 8 $M_\odot$ and many new sink particles have formed. In the next 3×10^5 yr, the initial three sink particles have masses of 10-20 $M_\odot$ and no star reaches a mass greater than 25 $M_\odot$ overall.

Figures 2.2 and 2.3 show density slices of the simulation, for the last 100 kyr. The vectors indicate velocity and the white points represent sink particles. Figure 2.2

shows four snapshots equivalent to the initial evolutionary stages before the H II region forms, occurring at 614.0, 624.3, 652.7 and 668.2 kyr. Initially, the cloud looks square as a consequence of not including turbulence in the initial conditions and the use of a grid-based code. The central rarefaction, and surrounding dense, ring-like structure may be a result of the cloud undergoing a rotational bounce (i.e. when the core — formed after the collapse of a rotating cloud — continually accretes from the envelope and then expands due to rotation and the increased gas pressure gradient, resulting in a ring at the cloud's centre; Cha & Whitworth 2003). Figure 2.3 shows the snapshots at the final stages of the run after the H II region has formed, at 730.4, 739.3, and 746.3 kyr. The thin white border encloses a region that has surpassed a 90% ionisation fraction.

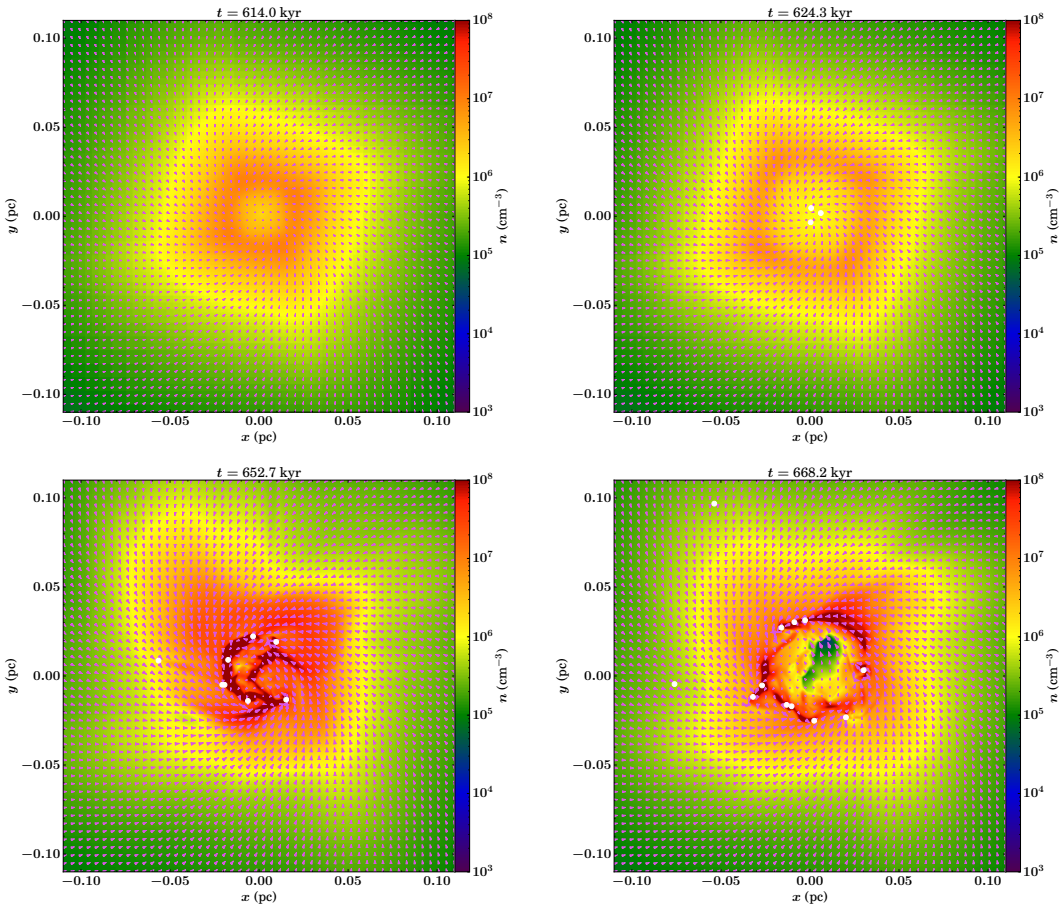

Figure 2.2: Snapshot density slices through the simulations of P10 depicting the stages prior to the formation of an H II region in the xy-plane. The time-steps shown reflect four initial evolutionary stages of the simulation occurring at 614.0, 624.3, 652.7, and 668.2 kyr. The arrows are velocity vectors and the white points are sink particles.

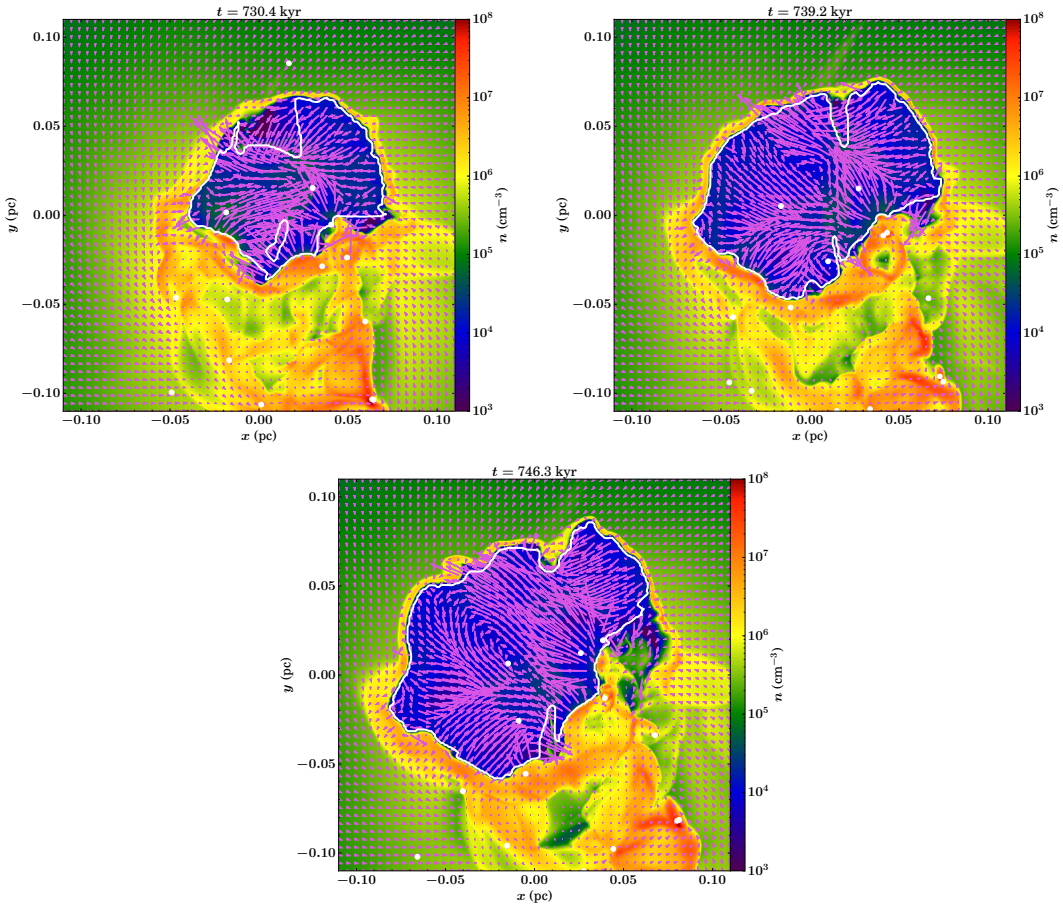

Figure 2.3: Snapshot density slices through the simulations of P10 after the formation of an H II region in the xy-plane. The time-steps reflect later evolutionary stages which occur at 730.4, 739.2, and 746.3 kyr. The arrows depict velocity vectors and the white points are sink particles. The thin white border marks the boundary of 90% ionisation fraction.

2.2.3 Observations and Simulations Compared

It is difficult to make an exact comparison between the observations and simulations, since G316.81–0.06 cannot be observed in its initial, molecular form. Juvela (1996) calculated the density and cloud mass of G316.81–0.06 in their multi-transition CS study, finding a mass of 1060 $M_\odot$ and number density 10^4 cm^{-3} which is in excellent agreement with the simulations[2].

The mass and size of the region can also be estimated from the IRDC. Longmore et al. (2017) calculated the mass of G316.752+0.004, an IRDC which encompasses

[2]The author also identifies a velocity gradient across the CS core. Unfortunately, the value is not specified.

G316.81–0.06. They found a mass of 1.5×10^4 $M_\odot$, however, their distance to the IRDC is highly uncertain. Of the two distances they derive, they adopt the farther distance of 9.8 kpc as opposed to the nearer distance of 2.6 kpc (the latter distance is used here). Using the nearer distance estimate, the mass of the IRDC is $\sim$ 1150 $M_\odot$ which is also in agreement with the initial molecular mass of the simulated cloud (1000 $M_\odot$). Assuming a distance of 2.6 kpc, the masses of the observed and simulated clouds are therefore similar.

The sizes of the observed and simulated regions are also similar. The area encompassing Regions 1 and 2 is $\sim$ 0.9 pc in diameter, although the IRDC from which the H II regions formed is certainly larger than this. The initial central condensed structure at 500 kyr of the simulations is 1.3 pc in diameter. Consequently, the density of the observations and simulations will also be on the same order of magnitude, in agreement with the aforementioned result of Juvela (1996). Given the similarity between the mass and size of the H II regions, it is reasonable to compare the observations to the simulations (bearing in mind the caveats in Section 2.2.2).

2.3 Data Analysis

The data analysis was performed using the Common Astronomy Software Applications (CASA; McMullin et al. 2007) package and the Semi-automated multi-COmponent Universal Spectral-line fitting Engine (SCOUSE; Henshaw et al. 2016). CASA was used to calculate 2nd moment maps (velocity dispersion, σ), and Gaussians were fit to the spectra using SCOUSE in order to determine centroid velocity (v_0). The input parameters for SCOUSE fitting are found in Table 2.1, according to Henshaw et al. (2016).

2.3.1 Observations

The H70α RRL spectra taken and reduced by Longmore et al. (2009) have been used for the data analysis. With CASA, the 2nd moment map was created between velocities –9.3 and –70.7 km s^{-1} including only pixels above 26 mJy beam^{-1} in order to

Parameter	Observations	Simulations
R_{SAA}	0.°001	0.°0003
RMS (K)	0.02	0.06
σ_{rms} (K)	3.0	3.0
T_1	5.0	5.0
T_2	2.5	2.5
T_3	2.5	1.7
T_4	1.0	1.00
T_5	0.5	0.5
v_{res} (km s^{-1})	0.5	1.56

Table 2.1: SCOUSE input. Parameter names according to Henshaw et al. (2016).

optimally exclude a weaker, contaminating second velocity component — toward the south-west of Region 1, the spectra contain an additional component which is broader (by 14.8%) and less intense (by 73.5%) than the primary component. Inspection of the datacubes shows that this emission is offset both in velocity and spatially, and thus, is unassociated with the ionised gas of Region 1.

Figure 2.4 shows Gaussian fits to both components, identified with SCOUSE. Where possible, the contribution of the secondary component was excluded from further analysis, Region 1 is only of interest. At locations where the secondary component is much weaker, it became difficult to distinguish between the two components. This means that we cannot create FWHM maps reliably, and that the results from the area covering the lowest third of Region 1 must be treated with caution.

2.3.2 Simulations

In order to compare the simulations and observations more robustly, the units of the H70α synthetic data have been transformed to be consistent with the observations. Intensity was converted from erg s^{-1} cm^{-2} Hz^{-1} ster^{-1} to Jy beam^{-1}; physical size converted to an angular size using 2.6 kpc; and frequency converted to velocity. Using CASA, the continuum was subtracted using `imcontsub` with the line-free channels: ≤ 6 and ≥ 54 (LTE); ≤ 10 and ≥ 54 (non-LTE).

A major difference between the LTE and non-LTE simulations were narrow absorption lines (LTE) and very bright, compact, and narrow emission lines (non-LTE) which perhaps emulate real maser emission. In non-LTE conditions, RRLs may undergo

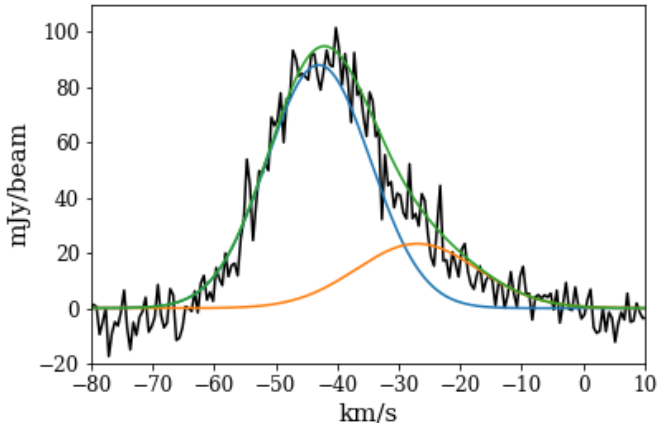

Figure 2.4: H70α spectra of the observational data (Region 1). With SCOUSE, a two-component fit was applied to minimise contamination in further analysis. The primary component (blue) and secondary component (orange) are each fitted by a Gaussian. The combined fit is shown in green.

maser amplification when the line optical depth is negative and its absolute value is greater than the optical depth of the free-free emission (Gordon & Sorochenko 2002, and references therein). The narrow emission dominates over the broad RRL emission, and appears almost as a delta function which prevents SCOUSE from being able to fit the non-LTE simulations. Therefore, a mask was applied to remove the majority of the narrow emission; every value greater than 10 mJy beam^{-1} was replaced with the average of the points either side.

The narrow absorption lines (LTE) also made SCOUSE fitting difficult. Significant portions of the broad RRL emission were often missing, making it challenging to fit the overall structure. Therefore, the absorption lines were removed via the RANdom SAmple Consensus (RANSAC; Fischler & Bolles 1981) method[3]. RANSAC iteratively estimates the parameters of a mathematical model from a set of data and excludes the effects of outliers. In this case, I selected five points at random (blue circles) along each spectrum (red) to make a Gaussian fit (Figure 2.5). Using RANSAC, the best fit is the fit with the most inliers (points with a residual error of less than 5%) out of three hundred iterations. Values of the original spectrum which lay outside the threshold (5%) are replaced by the values from the new fit so as not to entirely eradicate the original data. With this method it was possible to successfully remove

[3]For consistency, RANSAC was also applied to the non-LTE data after the narrow emission lines were removed.

the narrow absorption lines without distorting the data, in order to proceed with the SCOUSE fitting. This was only successful for the last three timesteps (730.4, 739.2, and 746.3 kyr). At earlier times (715.3 and 724.7 kyr), for which synthetic H70α data are also available, the LTE absorption lines are too wide to be accurately removed via the RANSAC method, and thus cannot be successfully fit by SCOUSE.

Finally, Gaussian smoothing was applied to both the LTE and non-LTE synthetic data with a beam size of 2.5 arcsec, using the `imsmooth` tool in CASA. This is the largest beam size possible while still being able to resolve the overall kinematic structure.

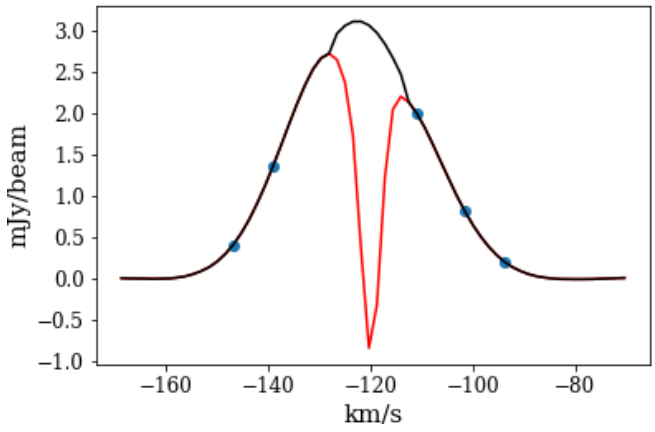

Figure 2.5: RANSAC example applied to the LTE synthetic data. The narrow absorption lines prevented successful fitting with SCOUSE so they were replaced. The original spectrum (red), the new spectrum (black), and the blue circles represent the five points used to make a Gaussian fit. In this example, this fit was chosen to be the best out of three hundred iterations.

2.4 Results

Table 2.2 contains the ranges in velocity (v_0(max)-v_0(min)), velocity gradients and maximum velocity dispersions for both the observational and synthetic H70α RRL data. Where the observations are concerned, Region 1 is the focus of the study, for it is the youngest H II region (Figure 2.6). Note that the measured velocity gradient is observed along the line-of-sight, and does not take into account any inclination that may be present. For the simulations (both LTE and non-LTE), we show the results of the final three ages: 730.4, 739.2, and 746.3 kyr in Figures 2.7 and 2.8.

	Time (kyr)	v_0 range (km s^{-1})	∇v_0 (km s^{-1} pc^{-1})	σ_{max} (km s^{-1})
Region 1	(E-W)	15.78 ± 0.45	47.81 ± 3.21	8.1
Region 1	(N-S)	5.14 ± 1.11	12.23 ± 2.70	8.1
LTE	730.4	14.59 ± 0.01	97.29 ± 12.97	13.1
LTE	739.2	11.64 ± 0.01	77.64 ± 10.35	12.1
LTE	746.3	12.04 ± 0.03	80.25 ± 10.70	12.1
LTE	730.4	10.49 ± 0.05	69.91 ± 9.33	13.0
LTE	739.2	10.40 ± 0.12	69.35 ± 9.28	11.8
LTE	746.3	13.54 ± 0.12	90.28 ± 12.07	11.8

Table 2.2: Values for the range in centroid velocity, v_0, velocity gradient, ∇v_0, and maximum velocity dispersion, σ_{max}, for Regions 1 in G316.81–0.06, in addition to the LTE and non-LTE simulations of P10 for the final three time-steps.

2.4.1 Observed ionised gas kinematics

Figure 2.6 contains the H70α centroid velocity and 2nd moment maps for the two H II regions in G316.81–0.06. Several velocity gradients across each region are visible in the centroid velocity map. Focusing on the younger H II region (Region 1, left), a velocity gradient roughly East-West (across $\sim$ 0.33 pc) can be seen. This is in addition to a less steep gradient North-South (across $\sim$ 0.42 pc) which is aligned with the elongation of the 35-GHz continuum and 'green fuzzy'. The 2nd moment map shows that both H II regions increase with σ towards the centre, and is highest towards the southern end of each region.

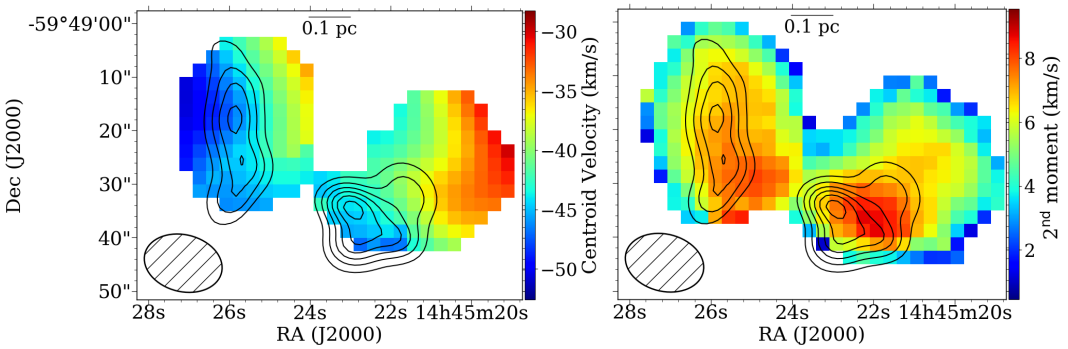

Figure 2.6: Maps of the two H II regions within G316.81–0.06: Region 1 (left) and Region 2 (right). Left: centroid velocity map (SCOUSE); right: 2nd moment map (CASA). The beam is shown at the bottom left of each map. Contours of the 35-GHz continuum are overlaid in black (Longmore et al., 2009).

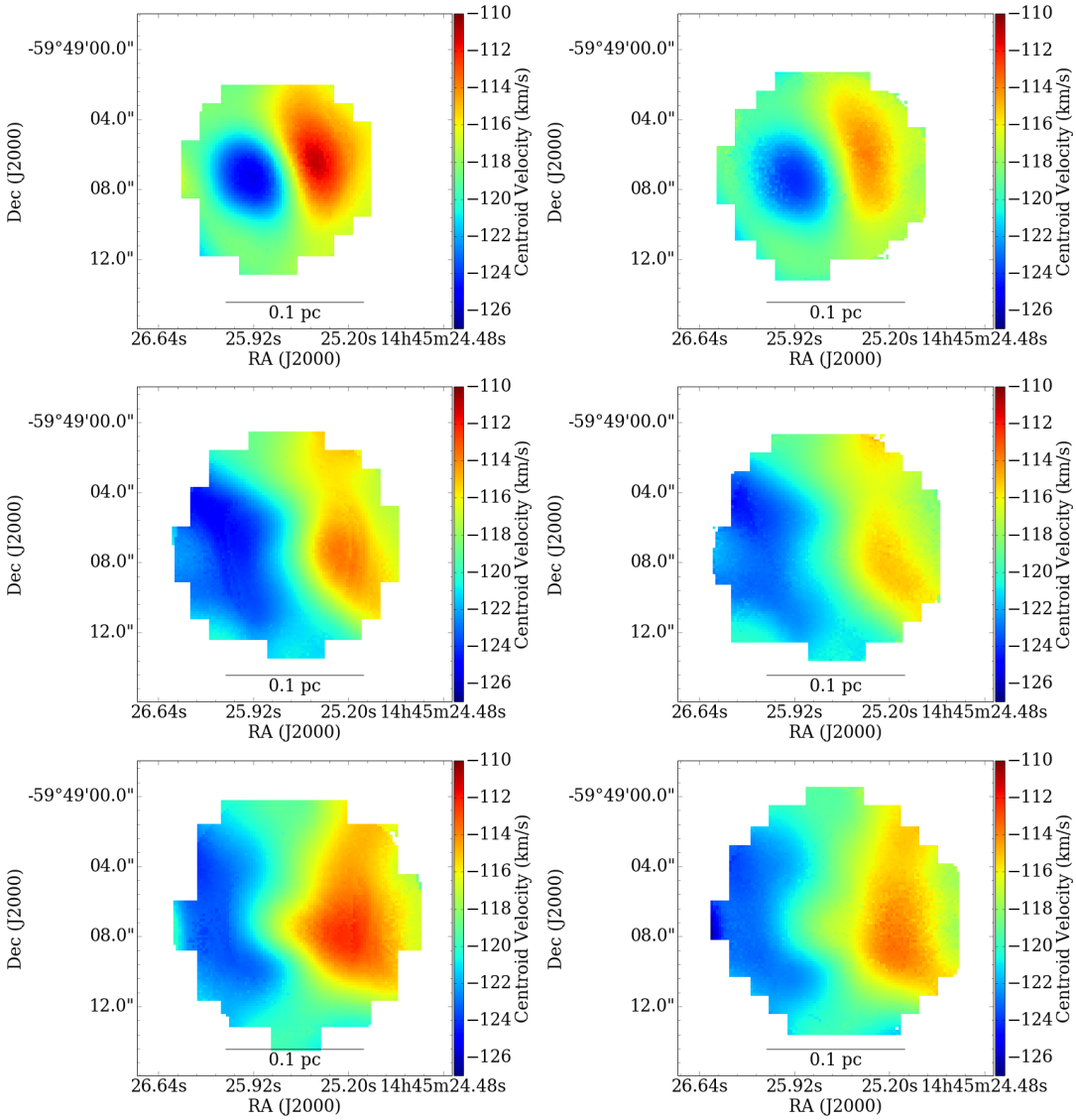

Figure 2.7: SCOUSE outputted centroid velocity of the simulated H70α data. Left: LTE; right: non-LTE, at ages of 730.4, 739.3, and 746.3 kyr increasing from top to bottom.

2.4.2 Simulated ionised gas kinematics

Figures 2.7 and 2.8 show the centroid velocity and 2nd moment maps of the LTE and non-LTE synthetic H70α data, at the final three ages 730.4, 739.2, and 746.3 kyr. The density slices (Figures 2.2 and 2.3) look down on the stars in the xy-plane, i.e. along the outflow axis. The synthetic H70α data have been chosen to be projected perpendicular to the outflow plane (oriented along the xz-plane) in order to compare with the observations. Although the inclination of the observed Region 1 outflow is not known; Figure 2.1 shows it is clearly closer to face-on than along the line-of-sight.

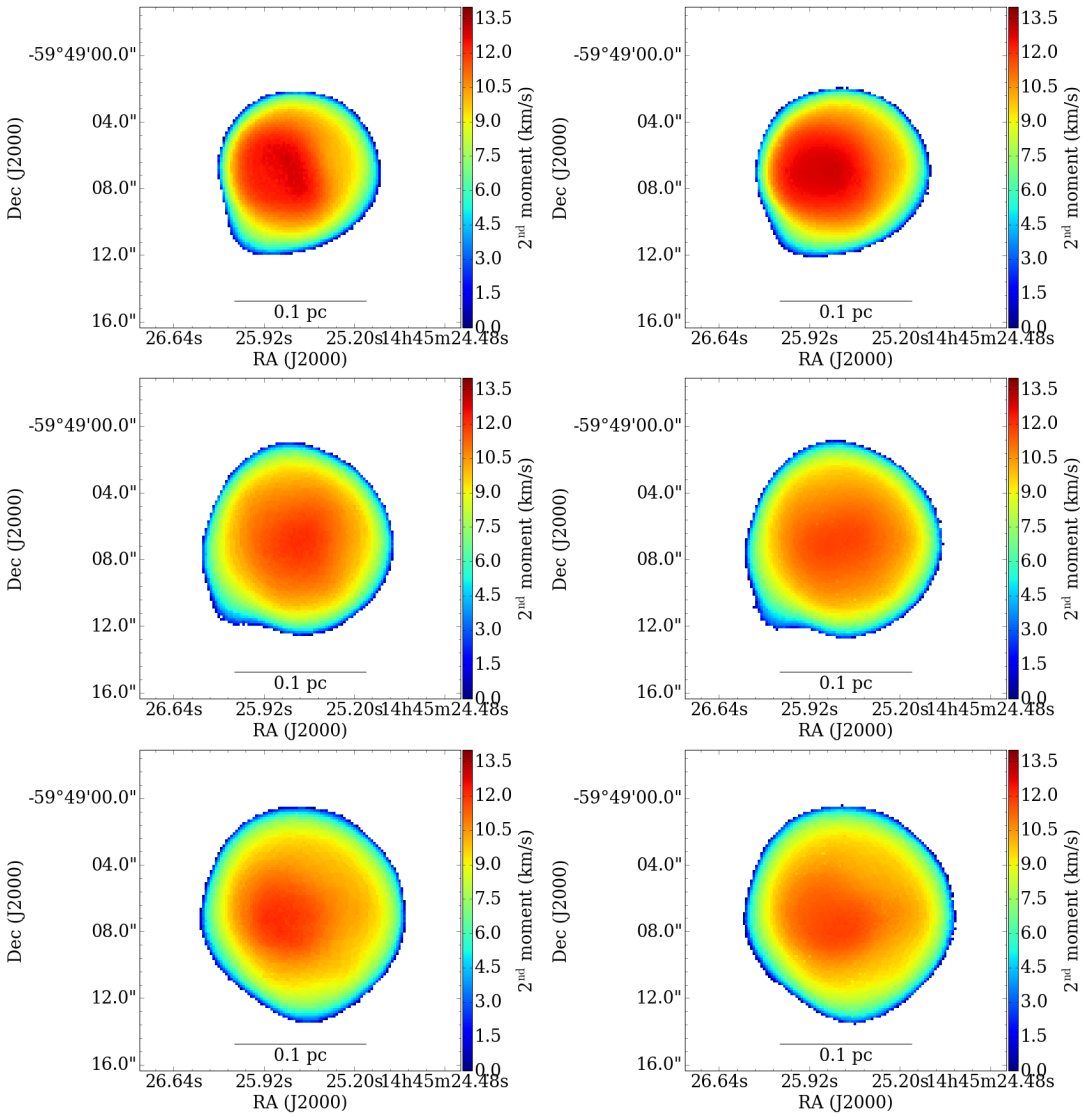

Figure 2.8: 2nd moment maps of the simulated H70α data outputted by CASA, showing the velocity dispersion. Left: LTE; right: non-LTE, at ages of 730.4, 739.3, and 746.3 kyr increasing from top to bottom.

Any inclination will introduce a change in observed velocity motions of order $\sin(\theta)$, where θ is the angle of inclination.

The velocity structure of the simulated ionised gas on 0.05 pc scales changes insignificantly between the different time steps for either the non-LTE or LTE synthetic maps. Given the similar kinematic structure between the non-LTE and LTE synthetic maps, non-LTE effects are not important for the analysis — I have focused on the LTE maps from here on. As this kinematic structure is a robust feature of the simulations, it seems reasonable to make comparisons to the observed ionised gas

kinematics.

The morphology of the centroid velocity and 2nd moment maps are similar to the observations; velocity gradients are oriented roughly east-west and velocity dispersion increases towards the centre. A significant difference is that the simulated H II region is smaller ($\sim$ 0.15 pc versus $\sim$ 0.33 pc), potentially resulting in the steeper velocity gradients compared to the observations, due to the conservation of angular momentum.

2.5 Discussion

As introduced in Section 2.1, prior literature looking at the ionised gas kinematics of H II regions has primarily focused on expansion, accretion, and outflows. There are, however, a small number of H II regions in the literature which display velocity gradients perpendicular to the outflow axis. For these regions, a common interpretation is that rotation in some form is contributing to the velocity structure. Section 2.5.1 summarises previous observations put forward as evidence that rotation is playing a role in shaping the velocity gradient. Section 2.5.2 looks to the P10 simulations to try and uncover the origin of the velocity gradient perpendicular to the outflow axis. Section 2.5.3 refers back to Region 1, discussing whether the velocity structure signifies rotation and what can be inferred with relation to feedback.

2.5.1 Evidence for rotation in young H II regions

W49A/DD. de Pree et al. (1997) find that this UCH II region has a north-south velocity gradient of a few km s^{-1} which they claim may be caused by the rotation of the ionised gas.

K3-50A. The bipolar H II region, K3-50A, shows a steep velocity gradient ($\sim$ 150 km s^{-1} pc^{-1}) along the axis of continuum emission, indicating the presence of ionised outflows (de Pree et al., 1994). There also appears to be an unmentioned perpendicular velocity gradient across the region which I estimate to be $\sim$ 30 km s^{-1} pc^{-1} (see Figure 5a).

NGC 6334A. The velocity gradient of this bipolar H II region was first detected by (Rodriguez et al., 1988). de Pree et al. (1995) confirmed this, finding a gradient of $\sim$75 $\mathrm{km\,s^{-1}\,pc^{-1}}$. They inferred that the signature can be attributed to rotation of the ionised gas, originating from a circumstellar disc. They derived a core Keplerian mass of $\sim$200 $\mathrm{M_\odot}$.

It has also been noted that NGC 6334A, K3-50A, and W49A/A are all alike in terms of their bipolar morphology and the possible presence of ionised outflows (de Pree et al., 1997).

2.5.2 Origin of the velocity structure in the P10 simulations

As models cannot (yet) take into account all of the physical mechanisms involved with the ionisation process, one common simplification is to use static high-mass stars. Such simple analytic models tend to show that ionisation occurs isotropically, for a homogeneous surrounding medium, resulting in no velocity gradient. However, in most simulations it is clear that stars are in motion with respect to each other and the surrounding gas.

In the P10 simulations this motion results in a preferred direction of ionisation, downstream of the stellar orbit. A simple cartoon (Figure 2.9), based on a qualitative examination of the simulated density vector maps (Figures 2.2 and 2.3), proposes an explanation for the red- and blue-shifted spectra of the observed RRL profile. The cartoon illustrates the evolutionary sequence beginning at the formation of the initial molecular cloud up to the formation of the H II region, explained in more detail by the following:

1. The initial molecular gas cloud has some net angular momentum (Ω, red dashed arrows), with increasing density towards the centre.

2. Once the local critical density of the gas is surpassed, stars (black) form with a high star formation efficiency at the centre of the cloud. The first star forms at the centre of the potential well then quickly drifts outwards, soon followed by the formation of more stars (on timescales of kyr). These stars immediately

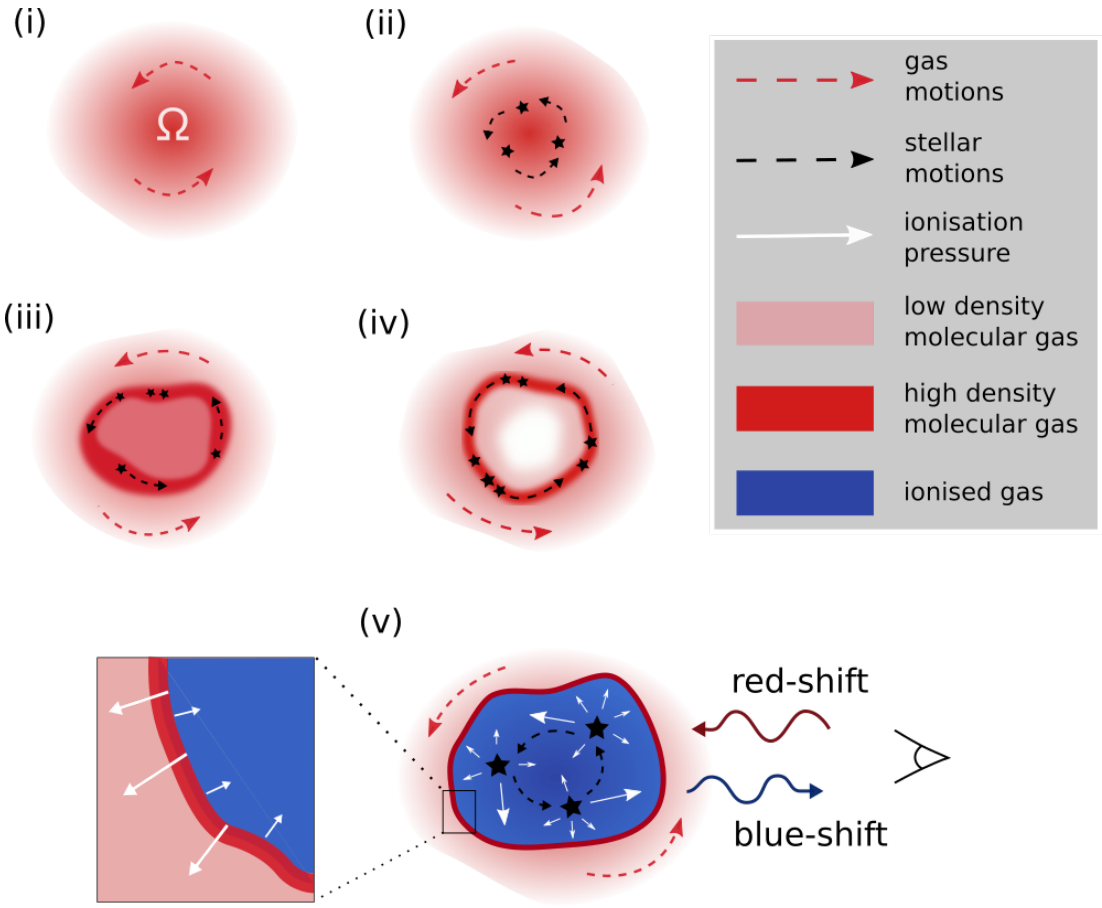

Figure 2.9: A cartoon illustrating the kinematic evolution of a young H II region. (i) The molecular gas cloud forms with some initial net angular momentum (Ω, red dashed arrows), with increasing density towards the centre of the cloud (pink). (ii) Stars (black) form at the centre of the molecular cloud when the critical density is surpassed, then drift outwards. The stars orbit about the cloud's centre, tracing the angular momentum of the cloud (black dashed arrows). (iii) A ring (solid red) forms as a result of rotational bounce (Cha & Whitworth, 2003). Stars continually gain mass and accrete material which gravitationally collects about the stars. The higher density ring initiates the formation of new stars. (iv) The centre becomes rarefied, meanwhile newly ionised material rapidly recombines (also known as flickering). (v) Ionisation dominates over recombination resulting in an H II region (blue). Ionisation is strongest to the front of the star's path where the pressure is lowest (white arrows). This appears as blue-shifted spectra when the star travels and ionises towards us, and red-shifted when the star travels and ionises away from the observer. Molecular material collects about the edge of the ionised region as the bubble expands (thick red solid line).

begin to trace the rotation of its natal cloud, about the centre of mass (black dashed arrows).

3. The central region starts to become rarefied and a ring-like structure appears

(solid red)[4], likely a result of rotational bounce (Cha & Whitworth, 2003). Simultaneously, material accumulates about the stars, and new stars form within the dense material, and in general continue to trace the rotation of the molecular cloud. The first star makes approximately one complete revolution until the simulation ends (across ~ 120 kyr), taking into account that the stars are continually moving outwards as they orbit.

4. In the simulations, the rarefied centre is made up of inhomogeneous regions of lower density and lower pressure (shown as solid white for simplicity). Newly ionised material rapidly recombines (also known as flickering; e.g. P10; Galván-Madrid et al. 2011). The stars continue to orbit about the centre of mass, and also interact with each other, some getting flung outside of the cloud. For a detailed description of stellar cluster formation in this simulation see Peters et al. (2010c).

5. Multiple high-mass ionising stars create one large ionised bubble (solid blue) also containing lower-mass stars. The thermal pressure created by ionisation heating drives the expansion of the H II region (white arrows), sweeping the surrounding neutral material into a dense shell (thick solid red line). The thermal pressure of the ionised gas is two orders of magnitude higher than in the molecular gas, and thus the pressure gradient term of the Euler equation dominates over the advection term at the H II region boundary. Hence, the ionised gas does not trace the rotation of the molecular gas directly. The stars act as mediators, inheriting their angular momentum from the molecular gas out of which they formed, and then create angular momentum in the ionised gas via a different mechanism (described in more detail below). This is shown by the magnitudes and directions of the velocity arrows of the ionised gas (Figure 2.3). If the ionised gas was put in rotation by the surrounding molecular gas, then the arrows on either side of the H II region boundary should always point in the same direction, which is clearly not the case. Furthermore, the varying length of the arrows within the H II region provides evidence for strong dynamical processes inside the H II region that would destroy any such coherent velocity pattern coming from the boundary.

[4]Note the similarity to the ring of H II regions in W49A (§ 2.5.1).

In fact, it is these dynamical processes that generate the rotational signature in the ionised gas as follows. Typically, models use an idealised scenario whereby the star is static and ionises isotropically (e.g. Spitzer 1978). However, in the frame of reference where the star is stationary, consider that upstream of the star's path, the gas flow in the cloud is in opposition to the direction of ionisation. This inhibits expansion of the ionised gas, as it is continually replenished by neutral material and recombines. Whereas downstream of the star's path, the neutral material travels with the direction of ionisation; the pressure is lowest ahead of the star in comparison to all other directions. Therefore, the expansion occurs predominantly in front of the star as it orbits, i.e. the path of least resistance. The velocity of the ionised gas traces the orbit of the stars and gas and hence, red- and blue-shifted spectra are observed along the line-of-sight in the ionised gas of the simulation.

2.5.3 G316.81–0.06: a rotating H II region?

Is the velocity structure in Region 1 solely due to the outflow and/or expansion of ionised gas or is it also rotating? If it is the former, the bipolar H II region would need to be significantly inclined. If it is the latter, Region 1 would need to be (close to) edge-on (i.e. the line of sight is primarily along the disc plane). Since (1) the elongated 35-GHz continuum and 'green fuzzy' clearly align along the axis of bipolarity, and (2) there exists a shallow velocity gradient North-South; Region 1 does indeed appear to be almost edge-on. While it cannot be ruled out that the observed velocity structure is caused only by a combination of expansion and outflow, it is difficult to construct a simple model that explains the velocity structure with only these mechanisms. Therefore, rotation is the most likely explanation for the East-West velocity gradient.

This is further supported when the ionised gas kinematics of the P10 simulations are compared with the observations of Region 1. As shown in Section 2.4, the morphology is similar, both in terms of the centroid velocity and 2$^{\rm nd}$ moment maps. However, the simulated velocity gradient is around a factor of two higher than that of Region 1. This may be due to the simulated region being twice as small ($\sim$ 0.15 pc as opposed to $\sim$ 0.33 pc). Additionally, a non-zero inclination would decrease the perceived radial velocity and so may also contribute.

Further work is needed to explore the significance of rotating gas as opposed to non-rotating gas, especially as it may indicate a preferred scenario for the formation of star clusters (Mapelli, 2017). In the absence of simulations fine-tuned to match the observations, or higher resolution observations to measure the velocities or proper motions of embedded stars it is not possible to test this scenario further. However, bearing in mind the caveats discussed in Section 2.2.2, the simulations remain a useful tool to aid our understanding of the motions of the ionised gas, especially given the simulations were not fine-tuned to the observations. Moreover, the unusual velocity gradients naturally emerge from the P10 simulations which were not designed to study this effect.

Although not included in the P10 simulations, another possible explanation for the rotation of G316.81–0.06 may be due to the IRDC, clearly seen in Figure 2.1. Accretion from the filament would likely induce some net angular momentum onto a central core. Watkins et al. (2019a) have also noted that their observed molecular gas velocity dispersions of the G316.75 ridge may contain contributions generated by rotation. Another interesting interpretation has previously been put forward by Garay et al. (1986). They predict that if the initial angular momentum of the cloud is determined by Galactic rotation, the magnitude of rotation will depend on the location in the Galaxy and the orientation of the angular momentum axis with reference to the Galactic plane. If Region 1 is truly rotating, similar velocity gradients should also be evident in RRLs for other young (bipolar) H II regions, which would provide a better means to test the aforementioned scenarios. For example, if rotation is induced by filamentary accretion, comparative studies between the kinematics of H II regions and IRDCs are required.

Overall, one can look to future Galactic plane surveys for answers. Upcoming and highly sensitive interferometers (e.g. EVLA- and SKA-pathfinders) will provide a high resolution census of all ionised regions in the Milky Way. These H II regions will be at different locations in the Galaxy, with different orientations and magnitudes of angular momentum with respect to Earth. We will have an invaluable test-bed at the earliest and poorly understood phases of star formation, allowing for the study of RRLs in H II regions across a large range of ages, sizes, and morphologies. Future high resolution observational surveys in combination with

suites of numerical simulations will also further our understanding of the differing contributing feedback mechanisms at early evolutionary stages and may help to constrain different star/cluster formation scenarios.

For example, the P10 simulations examined in this study give an idea of which feedback mechanism(s) have an important effect in G316.81–0.06. The simulations include both heating by ionising and non-ionising radiation, where the latter's only effect is to increase the Jeans mass (see discussion in Peters et al. 2010c). Therefore, all dynamical feedback effects in the simulation are due to photoionisation. This may imply that ionisation pressure is the dominating feedback mechanism required for the formation of a rotating ionised gas bubble and that radiation pressure and protostellar outflows are not needed to explain the dynamical feedback. This is potentially present in all H II regions and needs to be studied further in other simulations which incorporate different feedback mechanisms. Although the formation and evolution of galaxies will not be significantly different whether or not the outflowing gas is rotating, the potential to use the ionised gas kinematics as a tracer to identify very young H II regions represents an opportunity to understand feedback at the relatively unexplored time/size scales when the stars are just beginning to affect their surroundings on cloud scales.

2.6 Summary

I have studied a rare example of a young, bipolar H II region which shows a velocity gradient in the ionised gas, perpendicular to the bipolar continuum axis (Dalgleish et al., 2018). Comparisons between the H70α RRL observations and P10 synthetic data show that they both share a similar morphology and velocity range along the equivalent axes.

I have inferred that the velocity gradient of G316.81–0.06 is due to the rotation of ionised gas, and that the simulations demonstrate that this rotation is a direct result of the initial net angular momentum of the natal molecular cloud. Further tests are required to deduce the origin of this angular momentum, whether it is induced by Galactic rotation, filamentary accretion, or some other physical process.

If rotation is a direct result of some initial net angular momentum, this observational signature should be common and routinely observed towards other young H II regions in upcoming radio surveys (e.g. SKA, SKA-pathfinders, EVLA). Further work is required to know if velocity gradients are a unique diagnostic.

If rotation is seen to exist in many more H II regions, and we can uncover its true origins, this may help to parameterise the dominating feedback mechanisms at early evolutionary phases, in great demand by numerical studies. This should be achievable through systematic studies of many H II regions, combined with comparisons to a wider range of numerical simulations, likely offering a new window to this investigation.

Chapter 3

M/L of Galactic globular clusters

It was as if a globe had been filled with moonlight and hung before them in a net woven of the glint of frosty stars.

J. R. R. Tolkein

3.1 Introduction

Globular clusters (GCs) contain large numbers ($10^5 - 10^6$) of stars of roughly the same age and metallicity. For this reason, GCs are ideal laboratories for the study of the formation and evolution of stars and their host galaxies (e.g. Ashman & Zepf 1998). In particular, internal cluster kinematics have a key role in our understanding of GCs and their origins.

When research on this topic began in the late 1970s, studies depended on limited radial velocity information to derive velocity dispersions, dynamical masses, and other important cluster parameters (Pryor & Meylan 1993, and references therein). King (1966) models — and variations thereof — have commonly been used for this work, however static models such as these suffer limitations; they cannot account for cluster relaxation, a result of gravitational interactions of their member stars. Therefore, phenomena such as mass segregation, mass loss, or core collapse cannot be understood using these one-component static models. Multicomponent static models,

on the other hand, can take such evolutionary dynamical processes into account (see e.g. Torniamenti et al. 2019). They can be analytical, like the radially anisotropic multimass King-Michie models (Gunn & Griffin, 1979), `LIMEPY` models (Gieles & Zocchi, 2015), N-body models (Zonoozi et al., 2011; Heggie, 2014; Wang et al., 2016; Baumgardt, 2017; Baumgardt & Hilker, 2018), or Monte-Carlo models. Most recently, Baumgardt et al. (2019a) have used N-body models to determine masses, structural parameters, and mass-to-light ratios of 144 GCs, where they also included *Gaia* DR2 proper motions besides radial velocities.

The available kinematic data are often a significant limitation when constraining cluster parameters via evolutionary models. *Gaia* and most ground-based multi-object spectrographs like VLT/FLAMES or Keck/DEIMOS are unable to observe a large number of stars within the core radii of GCs because of the strong stellar crowding in those regions. Given the short relaxation times and expected overdensities of stellar remnants near the centres (due to mass segregation), it is likely a key area of parameter space has been missed. Now with *HST* and the development of integral-field units (IFUs) like MUSE, studies can measure the motions of thousands of stars — including those in the cluster centres — for the first time (e.g. Bellini et al. 2014, 2017; Kamann et al. 2018a; Ferraro et al. 2018). This has opened up new avenues to uncover the populations of central stellar remnants, like stellar-mass black holes (e.g. Giesers et al. 2018, 2019; Baumgardt et al. 2019b), which can further aid our understanding of the internal structures of GCs.

One puzzle yet to be solved is the notable discrepancy between theoretical predictions and observations of GC M/L ratios. Simple stellar population (SSP) models predict that the mass-to-light ratio in the V-band ($M/L_{\rm V}$) should increase with metallicity — given a constant initial mass function (IMF) — as a result of line blanketing (e.g. Bruzual & Charlot 2003; Maraston 2005; Conroy & Gunn 2010). However, Djorgovski et al. (1997) and Strader et al. (2009, 2011) found that for the globular clusters in M31, M/L decreases with [Fe/H]. In the Milky Way, the situation appears to be similar; Kimmig et al. (2015) showed that M/L is $\gtrsim 2$ times lower than expected for clusters at the metal-rich end. Equally, Baumgardt (2017) found that the observed M/L-[Fe/H] relation also disagrees with SSP models: they find no change of M/L with cluster metallicity. Very few metal-rich Galactic clusters ([Fe/H] > -0.5 dex) were included

in the studies of Kimmig et al. (2015) and Baumgardt (2017), however, so it is unclear if the discrepancy for MW clusters is as pronounced as it is for M31 towards solar metallicity. This is further emphasised by Shanahan & Gieles (2015), who discuss the challenges of reliably measuring the M/L of star clusters from integrated light.

Understanding where the discrepancy between observed M/L and SSP model predictions originates is key. SSP models are used to determine a wide range of important properties — including stellar masses, star formation histories and metallicities — from the integrated light of galaxies and extragalactic star clusters (e.g. Gallazzi & Bell 2009; Conroy 2013; Martins et al. 2019). Furthermore, the mismatch between observed stellar M/L and SSP model predictions has been used to constrain the IMF (e.g. Cappellari et al., 2012; Newman et al., 2013). Hence, more high-resolution observations of metal-rich clusters are needed to confirm the discrepancy between theory and observation.

WAGGS, the WiFeS Atlas of Galactic Globular cluster Spectra survey (Usher et al., 2017, 2019) has already significantly extended GC observations to include younger and more metal-rich clusters. The survey is also particularly advantageous since it covers the central regions of all clusters ($\lesssim$ 20 arcsec). Our study uses the WAGGS survey to fill this gap in the literature, with newly-determined central velocity dispersions, dynamical masses, and $M/L_{\rm V}$ for 59 globular clusters in the Milky Way. For twelve of these GCs, $M/L_{\rm V}$ have never before been derived, due to the lack of kinematic information.

The chapter is organised as follows: the observations are described in Section 3.2, followed by a description of the data reduction and analysis (Section 3.3). The results and discussion are presented in Sections 3.4 and 3.5 respectively, concluding with a summary in Section 3.6.

3.2 Observations

For this work, I have studied a subset of 59 GCs taken from the WAGGS survey (Figure 3.1). The clusters were selected on the basis that they either have *HST* photometry and imaging publicly available, they are metal-rich (i.e. NGCs 6528 and 6553), or

there are fewer than 25 radial velocity measurements in the Baumgardt et al. (2019a) sample.

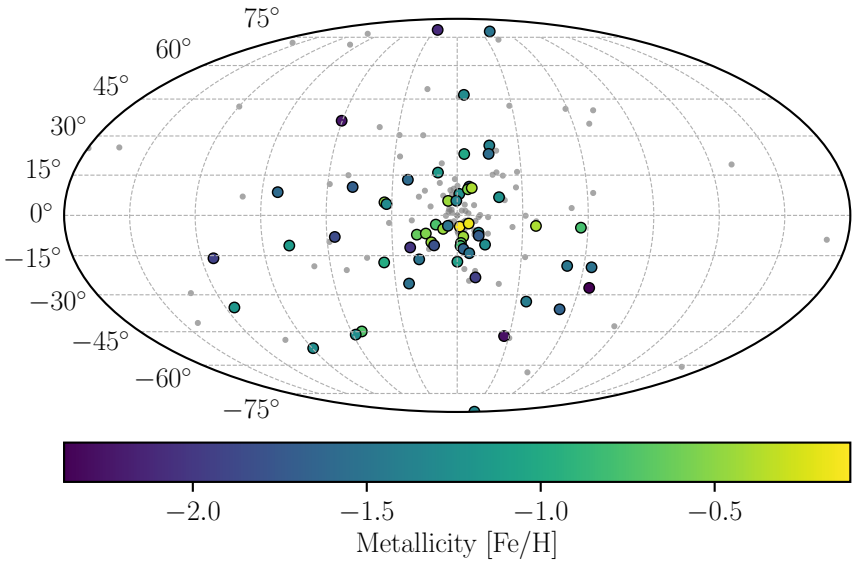

Figure 3.1: Milky Way globular clusters projected in Mollweide space in Galactic coordinates. The subset of 59 globular clusters from the WAGGS survey used in this study are highlighted: the most metal-rich clusters appear yellow and are found towards the bulge, and the most metal-poor clusters are in purple, typically found towards the halo. Any remaining Milky Way GCs are shown as grey dots (Harris, 1996, 2010).

WAGGS observations were made between 2015 and 2018 using WiFeS, the Wide-Field Spectrograph, on the 2.3-m ANU telescope (Dopita et al., 2007, 2010). WiFeS is an IFU spectrograph with a field-of-view of 38×25 arcsec. I used the four higher resolution gratings (U7000, B7000, R7000, and I7000) in two setups to cover the wavelength range 3300 – 9000 Å with spectral resolution, R $\sim$ 6800. Further details regarding the observations and data reduction can be found in Usher et al. (2017). In addition to the observations described in Usher et al. (2017, 2019), new observations of NGCs 6325, 6355, 6380, 6453, 6528, 6553, and 6760 have been included, carried out between September 10th–13th 2018. Of these, NGC 6528 and NGC 6553 had already been observed before. Unlike most WAGGS observations, which had only a single pointing toward the GC centre, the new NGC 6528 and NGC 6553 observations were tiled with four pointings. The September 2018 observations were reduced using PyWiFeS (Childress et al., 2014b,a) in the same manner as described in Usher et al. (2017).

3.2.1 Photometry

Photometry for the clusters is required to extract the spectra from the WAGGS datacubes (see Section 3.3.1) and comes from previous literature wherever possible. For the majority of GCs, I obtained existing *HST* photometry from the UV Legacy Survey (Soto et al., 2017). NGC 6528 photometry was sourced from the Hubble Legacy Archive, in programs 5436 (PI: Ortolani), 8696 (PI: Feltzing), 9453 (PI: Brown), 11664 (PI: Brown), and the photometry for NGC 6356 and NGC 7006 were obtained from Piotto et al. (2002) and Dotter et al. (2011), respectively. For eight of the clusters, photometry was not available (i.e. NGCs 5946, 6325, 6342, 6355, 6380, 6453, 6517, and 6553). These remaining clusters were reduced using *HST* observations as shown in Table 3.1.

Cluster	Camera	Filter	Exposures	Program ID	Epoch
NGC 5946	WFC3/UVIS	F438W	3×500 s	11628	2009.6
		F555W	3×80 s		
NGC 6325	WFC3/UVIS	F438W	3×435 s	11628	2010.3
		F555W	3×85 s		
NGC 6342	WFC3/UVIS	F438W	3×420 s	11628	2009.6
		F555W	3×80 s		
NGC 6355	WFC3/UVIS	F438W	3×440 s	11628	2009.6
		F555W	3×80 s		
NGC 6380	WFC3/UVIS	F555W	3×440 s	11628	2010.2
		F814W	3×80 s		
NGC 6453	WFC3/UVIS	F438W	3×450 s	11628	2010.4
		F555W	3×80 s		
NGC 6517	WFC3/UVIS	F555W	3×420 s	11628	2010.3
		F814W	3×100 s		
NGC 6553	ACS/WFC	F435W	3×340 s	10753	2006.3
		F555W	1×300 s		
		F814W	1×60 s		

Table 3.1: List of newly analysed *HST* observations used for this project.

The reduction of all *HST* exposures is based on `_flc` images. These images have been corrected for the flat-field and charge-transfer efficiency effects (Anderson & Bedin, 2010; Anderson & Ryon, 2018) and bias-subtracted via the standard *HST* pipelines, and contain the unresampled pixel data for stellar-profile fitting. For more detail see Dalgleish et al. (2020).

3.3 Data Reduction and Analysis

3.3.1 Stellar spectra

PampelMuse (Kamann et al., 2013) was used to extract the stellar spectra from the WAGGS data cubes. The software optimally extracts the spectrum of each resolved star from a cube using an analytical model of the point-spread function (PSF). The model parameters can be wavelength-dependent and are optimised during the fit. The coordinates of each resolved source are inferred from the source catalogues described in Section 3.2.1. The PSF-fitting technique allows one to de-blend clean stellar spectra even in crowded stellar fields such as the centres of GCs. This process, however, will always yield a fraction of spectra with a signal-to-noise (S/N) that is too low ($\lesssim 5$ Å^{-1}) for a meaningful analysis. This problem often affected the spectra of red giant branch stars observed with the U7000 and B7000 gratings, in particular for clusters with high extinctions. Example spectra of an asymptotic giant branch star from NGC 6752 (*Gaia* DR2 ID: 6632372787224214912) can be seen in Figure 3.2. The S/N per pixel is higher than the typical observed spectra, and is as follows: 14.3 (U7000), 24.4 (B7000), 26.1 (R7000), and 29.6 (I7000).

For each spectrum, effective temperature (T) and surface gravity ($\log g$) were determined by over-plotting MIST (MESA Isochrones & Stellar Tracks) isochrones (Dotter, 2016; Choi et al., 2016; Paxton et al., 2011, 2013, 2015) on a colour-magnitude diagram (CMD). I assumed an age of 12.59 Gyr for each cluster and adopted the metallicities in the 2010 edition of the Harris (1996, 2010) catalogue. An example $m_{\mathrm{F606W}} - m_{\mathrm{F814W}}$ versus m_{F606W} CMD for NGC 6752 can be seen in Figure 3.3. The stellar spectra were cross-correlated against a grid of T and $\log g$ values corresponding to a synthetic PHOENIX template spectrum (Husser et al., 2013). GC α-element abundances (either $[\alpha/\mathrm{Fe}] = 0.2$ or 0.4) were, in the first instance, taken from Carretta et al. (2010). In the second instance, I used Dias et al. (2016) in the absence of Carretta et al. (2010) data. For the clusters lacking $[\alpha/\mathrm{Fe}]$ measurements, $[\alpha/\mathrm{Fe}] = 0.4$ was used.

I determined radial velocities using `FXCOR` in PyRAF (Greenfield & White, 2000, 2006; de La Peña et al., 2001; Science Software Branch at STScI, 2012); a task based on the Fourier cross-correlation method developed by Tonry & Davis (1979). The wavelength

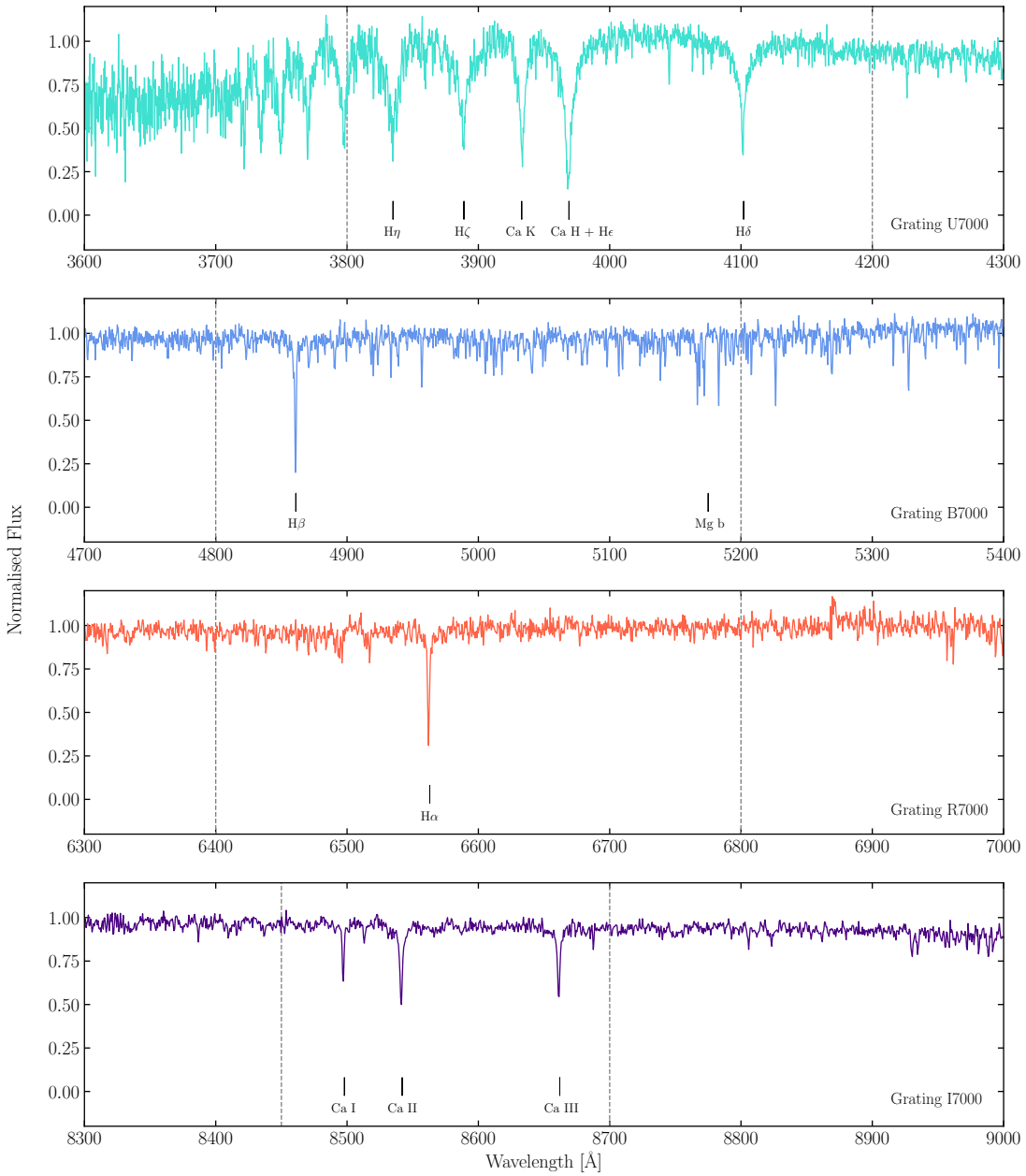

Figure 3.2: Example spectra (*Gaia* DR2 ID: 6632372787224214912) of an asymptotic giant branch star in NGC 6752 extracted by PampelMuse across four different gratings (U7000, turquoise; B7000, blue; R7000, red; I7000, purple). The grey dashed lines mark the wavelength ranges used to cross-correlate against the PHOENIX template spectra. The wavelength ranges were chosen to avoid telluric lines. Prominent hydrogen and calcium lines are also marked.

ranges used for the cross-correlation were selected in order to include important lines (e.g. Calcium triplet, Hα) while avoiding telluric lines. I used wavelength ranges as follows: I7000 grating ($\lambda\lambda$ = 8450–8700 Å); R7000 grating ($\lambda\lambda$ = 6400–6800 Å); B7000 grating ($\lambda\lambda$ = 4800 – 5200 Å); and U7000 grating ($\lambda\lambda$ = 3800 – 4200 Å), shown by the

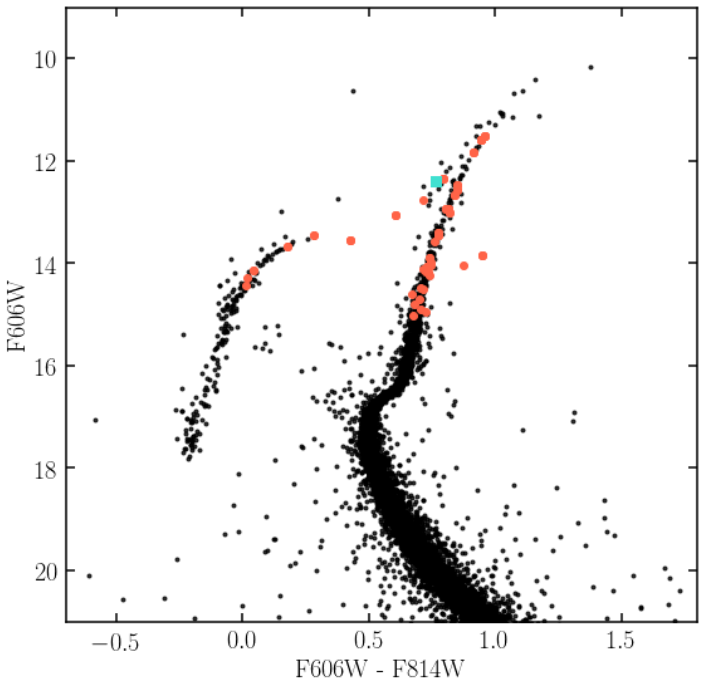

Figure 3.3: An example colour-magnitude diagram of NGC 6752 with photometry from the UV Legacy Survey (Soto et al., 2017). Stars with WAGGS spectra are marked in red. The turquoise square corresponds to the spectrum depicted in Figure 3.2.

grey dashed lines in Figure 3.2. Since each spectrum was cross-correlated against a grid of PHOENIX spectra, the radial velocity with the highest Tonry and Davis Ratio (TDR; a measure of how good the fit is) was used.

Similar to the method of Kamann et al. (2014), I plotted systemic velocities from each grating against S/N in log-log space (Figure 3.4), in order to remove unreliable measurements from the RV sample. $S/N > 8$ and $TDR > 13$ yielded 4136 stars for all 59 clusters, whereas $S/N > 7$ and $TDR > 16$ yielded 4258 stars, thus I chose the latter in order to retain the largest number of stars. The grey dotted line in Figure 3.4 depicts the cut at $S/N = 7$, and spectra shown as small dots have values of $TDR < 16$. The same cut was used for all four gratings. After applying these cuts, a sample of 29, 631, 1169, and 2429 spectra remain in the U7000, B7000, R7000, and I7000 gratings, respectively.

To account for nightly systematic variances between the different gratings, I calculated a shift in velocity between the different gratings, relative to the I7000 grating, per star per night. The I7000 grating was chosen since it contains the greatest number of spectra with the smallest uncertainties. Averaging the shifts for all stars each night, I

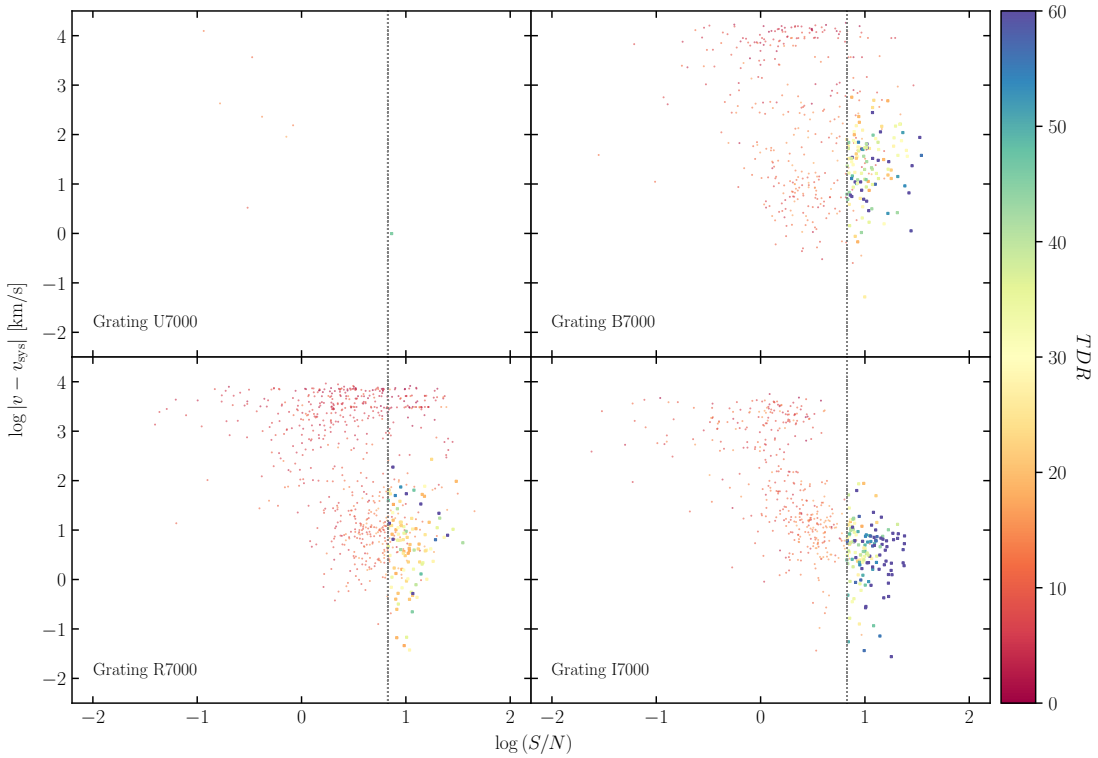

Figure 3.4: Absolute velocity difference (with respect to the cluster systemic velocity) versus S/N for all spectra for each grating in log-log space. The spectra belong to all 59 clusters and are coloured according to their TDR value. Spectra with $TDR < 16$ (shown as small dots) and $S/N < 7$ (grey dotted lines) are deemed unreliable and have been excluded from further analysis. A maximum of $TDR = 60$ has been applied to better see the spectra at lower values.

applied a correction to the radial velocities in the U7000, B7000, and R7000 gratings (Figure 3.5).

After averaging the velocities obtained from the different gratings, I applied sigma clipping ($\sigma = 3$) to exclude any outliers in velocity space. For NGC 6496, for which there are very few stars, two clear outliers were still present (with radial velocities differing by ~ 160 km/s), and were removed by hand. Overall, I only used sufficiently accurate velocity measurements, usually velocity errors less than 1.5–2 km/s, depending on the internal velocity dispersion of the cluster.

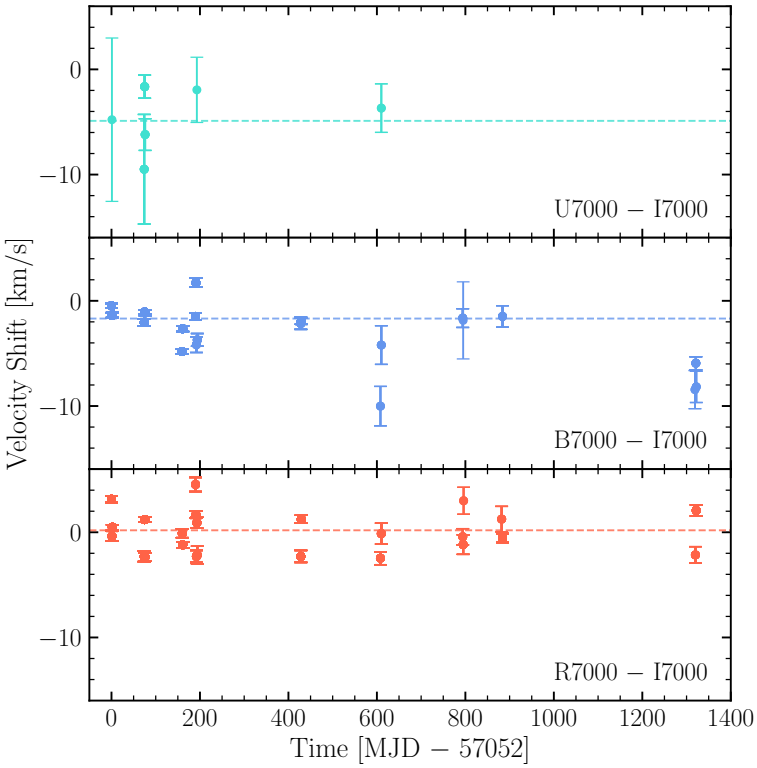

Figure 3.5: The average shift in velocity in the U7000 (turquoise), B7000 (blue), and R7000 (red) gratings with respect to the I7000 grating. The average velocity shift is shown as a dashed line. Shifts are calculated by taking the differences in velocity measurements that are associated with the same star, and then averaging over all the velocity differences from all stars each night.

3.3.2 *N*-body models

The observational data of each globular cluster are compared to a large grid of 2,500 N-body simulations. The simulations of isolated star clusters each contain $N = 100,000$ stars and are run using the GPU-enabled version of the collisional N-body code NBODY6 (Nitadori & Aarseth, 2012). The simulated clusters follow King (1962) density profiles with variations of initial concentrations ($0.2 \leq c \leq 2.5$) and initial radii ($2 \leq r_h \leq 35$ pc). The initial mass function of the star clusters are also varied from those following an initial Kroupa (2001) mass function to clusters highly depleted in low-mass stars.

All simulations are run up to an age of $T = 13.5$ Gyr and final cluster models are calculated by taking 10 snapshots from the simulations centred around the age of each GC. The combined snapshots of the N-body clusters are scaled in mass and

radius to match the density and velocity dispersion profiles of the observed globular clusters — the best-fitting model is determined by interpolating in the grid of N-body simulations. Further details of the performed N-body simulations can be found in Baumgardt (2017) and Baumgardt & Hilker (2018).

3.4 Results

The WAGGS radial velocities are combined with the Baumgardt et al. (2019a) data before fitting the N-body models to each cluster. Each set of velocity measurements are shifted to a common velocity by cross-matching the different datasets against each other to correct for zero-point offsets. All velocity measurements for each star are averaged, and any stars with varying radial velocities are assumed to be binaries and are excluded.

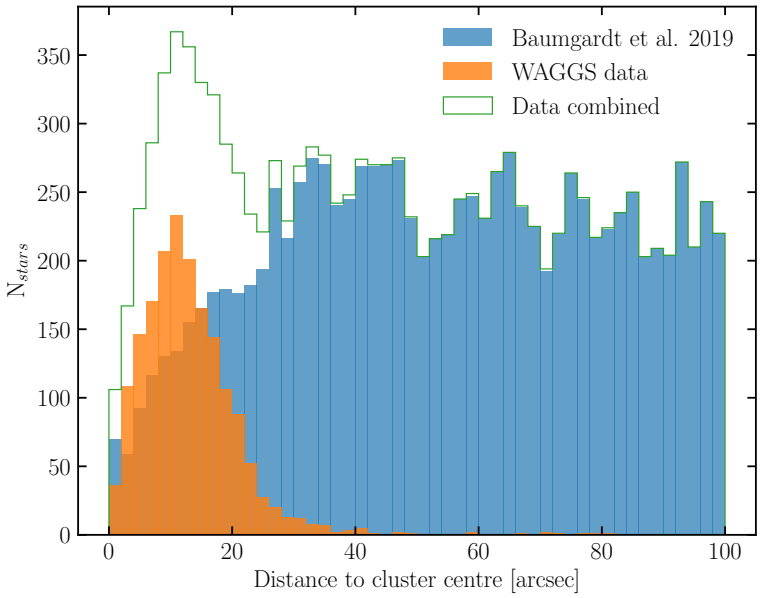

Figure 3.6: The number of radial velocity measurements of the 59 MW GCs in the WAGGS sample. There is a cut at 100 arcsec to emphasize the data in the central regions. Previous values already in the Baumgardt et al. (2019a) sample are in blue. New measurements are in orange; the majority lie within 20 arcsec of the cluster centres, significantly increasing the number of measurements in this area of parameter space. The green outline contains the sum of the total sample used in the N-body modelling.

In the end, the Baumgardt et al. (2019a) dataset is increased by 1,622 WAGGS measurements, within approximately 20 arcsec from the cluster centres (Figure 3.6).

This is smaller than the half-light radii, where the ratio of observed to half-light radius is ~ 0.3 on average, and ranges between 0.1 (for the more dispersed) and 0.8 (for the more compact GCs). The dataset can be found online[1]. For 16 of the clusters, the number of velocity measurements has increased by more than 50%.

Velocity dispersion profiles are determined by combining velocity measurements with *Gaia* proper motions (where available). The stars are ordered according to central distance before calculating velocity dispersion (using a maximum likelihood approach, see Pryor & Meylan 1993) and χ^2 for each member — those with too large χ^2 are removed. This process is repeated until a stable solution is found. Velocity errors have also been taken into account. Each velocity dispersion profile is combined with the corresponding surface density profile and stellar mass function in order to derive cluster mass. This is done by fitting a grid of N-body simulations to the combined data as described in Baumgardt (2017); Baumgardt & Hilker (2018) — examples of which can be seen in Figure 3.7.

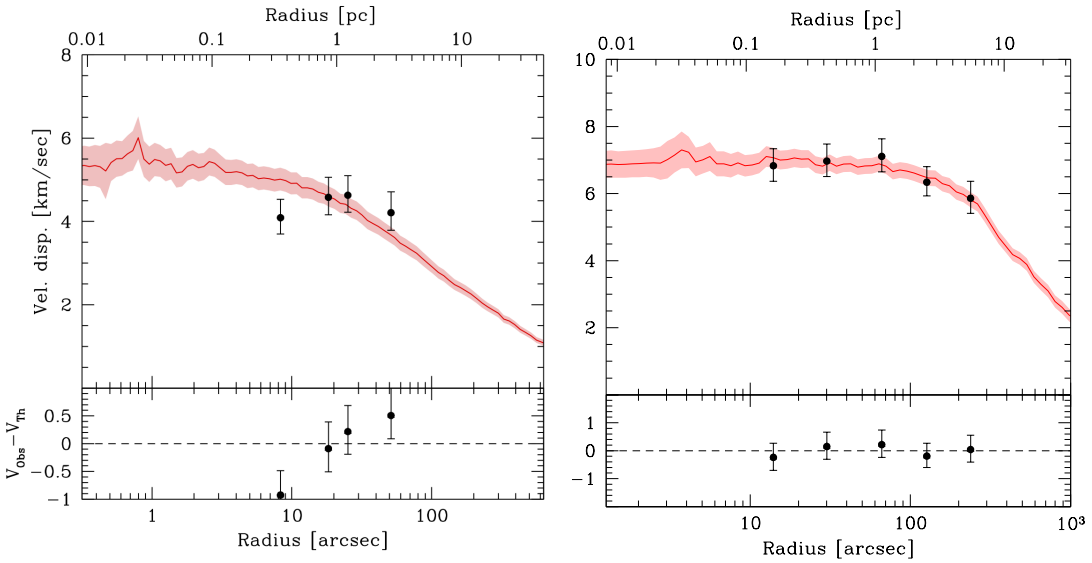

Figure 3.7: N-body fits for NGC 6528 (left), and NGC 6553 (right) radial velocities (not including proper motions). The reduced chi-squared values are 1.60, and 0.14, respectively.

Cluster M/L_V ratios are calculated using the mean cluster luminosity from Harris (1996); McLaughlin & van der Marel (2005); Dalessandro et al. (2012) in addition to luminosity determinations from Baumgardt & Hilker (2018). The results are

[1] https://people.smp.uq.edu.au/HolgerBaumgardt/globular/

presented in Table 3.2.

3.4.1 Comparisons to Previous Work

The derived central velocity dispersions and masses are compared to previous work in Figure 3.8: 20 clusters overlap with the Kimmig et al. (2015) sample; and ten can be compared to Ferraro et al. (2018). The central velocity dispersions derived by each study are (King) model predictions based on velocity dispersions further out. For completeness, I also compare the results of Baumgardt et al. (2019a) to this work. Twelve clusters (NGCs 5946, 6325, 6333, 6342, 6355, 6356, 6380, 6453, 6517, 6642, 6760, 7006) are previously little studied, and thus cannot be compared.

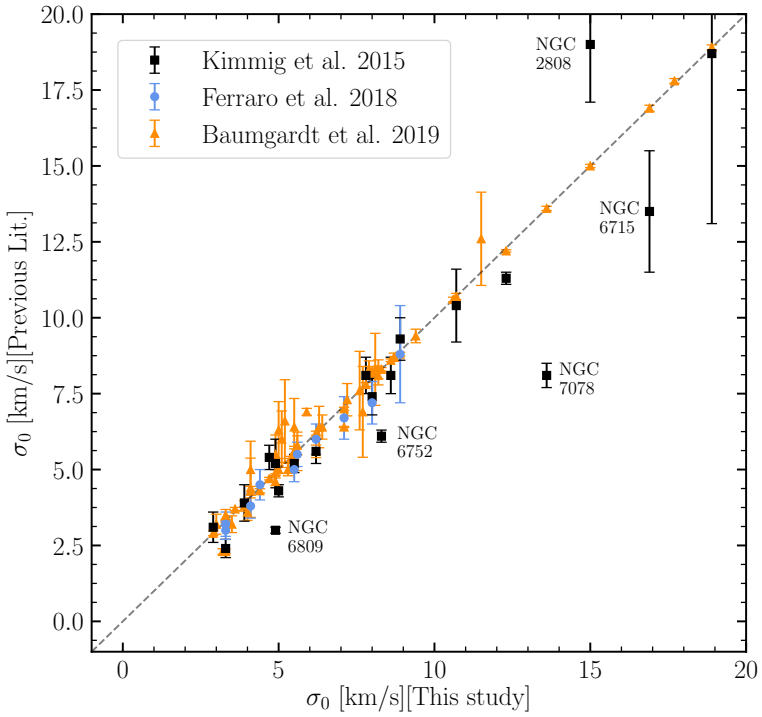

Figure 3.8: The (1D) central velocity dispersions of 59 WAGGS Milky Way globular clusters compared to Kimmig et al. (2015, black squares), Ferraro et al. (2018, blue circles), and Baumgardt et al. (2019a, orange triangles). Some of the most discrepant GCs from Kimmig et al. (2015) are labelled.

The most significant discrepancies lie with the results of Kimmig et al. (2015), particularly for NGCs 2808, 6715, and 7078. Whereas the central velocity dispersions of Ferraro et al. (2018) are all slightly lower than the values derived here. As their results are based on multi-object spectroscopy, this could be caused by differences in

GC Name	[Fe/H] [dex]	Mass [$\times 10^5$ $M_\odot$]	Δ Mass	M/L_V [$M_\odot/L_\odot$]	Δ M/L_V	σ_0 [km/s]	N_{total}	N_{WAGGS}
NGC 104	-0.72	8.07	0.05	1.82	0.17	12.3	3254	78
NGC 288	-1.38	1.21	0.03	2.39	0.17	3.3	528	1
NGC 362	-1.26	3.37	0.05	1.7	0.25	8.9	479	19
NGC 1261	-1.27	1.73	0.15	2.2	0.38	5.6	288	39
NGC 1851	-1.18	2.83	0.04	1.92	0.14	10.6	669	58
NGC 2298	-1.92	0.54	0.1	2.11	0.42	3.5	40	8
NGC 2808	-1.14	8.18	0.06	1.67	0.12	15.0	1135	88
NGC 3201	-1.59	1.46	0.05	2.46	0.42	4.4	721	14
NGC 4590	-2.23	1.29	0.11	2.33	0.46	3.9	248	11
NGC 4833	-1.85	2.03	0.12	1.29	0.25	4.9	162	17
NGC 5024	-2.10	4.28	0.35	1.79	0.21	6.2	334	21
NGC 5272	-1.50	3.61	0.16	1.57	0.22	8.0	668	24
NGC 5286	-1.69	3.79	0.17	1.39	0.13	9.4	523	37
NGC 5904	-1.29	3.66	0.06	1.47	0.19	7.8	827	36
NGC 5927	-0.49	3.44	0.03	2.17	0.3	7.1	395	60
NGC 5946	-1.29	0.75	0.20	1.17	0.35	5.5	33	24
NGC 5986	-1.59	3.31	0.24	1.95	0.27	8.2	237	15
NGC 6121	-1.16	0.90	0.02	1.96	0.11	4.7	2817	11
NGC 6171	-1.02	0.77	0.04	2.19	0.61	4.1	373	22
NGC 6218	-1.37	0.82	0.04	1.51	0.34	5.0	495	13
NGC 6254	-1.56	1.88	0.04	1.8	0.06	6.2	406	16
NGC 6304	-0.45	1.61	0.14	2.12	0.38	5.3	171	5
NGC 6325	-1.25	0.73	0.12	1.65	0.45	6.3	42	34
NGC 6333	-1.77	3.16	0.24	2.28	0.22	8.2	34	25
NGC 6342	-0.55	0.60	0.11	3.64	1.52	5.6	49	33
NGC 6352	-0.64	0.55	0.02	1.79	0.17	3.3	40	8
NGC 6355	-1.37	0.71	0.14	0.57	0.15	5.2	50	32
NGC 6356	-0.40	3.82	0.80	1.55	0.36	7.6	44	23
NGC 6362	-0.99	1.08	0.03	2.25	0.12	3.6	342	3
NGC 6380	-0.75	3.05	0.02	2.06	2.73	8.1	46	36
NGC 6388	-0.55	10.4	0.09	1.87	0.23	17.7	511	26
NGC 6397	-2.02	0.89	0.01	2.23	0.35	5.4	2399	11
NGC 6441	-0.46	11.7	0.11	2.01	0.13	18.9	214	10
NGC 6453	-1.50	2.33	0.02	3.54	0.99	7.7	21	19
NGC 6496	-0.46	0.84	0.12	1.84	1.08	3.3	127	7
NGC 6517	-1.23	3.04	0.55	2.18	0.71	11.5	32	16
NGC 6528	-0.11	0.60	0.07	1.5	0.43	5.0	159	117
NGC 6541	-1.81	2.50	0.08	1.52	0.53	8.7	206	49
NGC 6553	-0.18	3.01	0.16	2.12	0.28	7.9	499	138
NGC 6584	-1.50	1.16	0.02	1.43	0.35	4.1	26	20
NGC 6624	-0.44	0.62	0.02	0.99	0.12	5.9	344	6
NGC 6637	-0.64	1.48	0.16	0.84	0.16	6.4	62	48
NGC 6642	-1.26	0.25	0.07	0.71	0.2	4.1	20	13
NGC 6652	-0.81	0.46	0.08	1.48	0.42	5.1	40	37
NGC 6656	-1.70	4.05	0.04	1.93	0.07	8.6	800	19
NGC 6681	-1.62	1.13	0.02	1.95	0.27	7.1	52	21
NGC 6715	-1.49	15.9	0.19	2.18	0.1	16.9	533	16
NGC 6717	-1.26	0.36	0.08	2.09	0.58	3.2	17	14
NGC 6723	-1.10	1.73	0.11	1.89	0.29	5.5	368	20
NGC 6752	-1.54	2.30	0.03	2.15	0.34	8.3	1184	37
NGC 6760	-0.40	2.57	0.30	2.01	0.27	7.2	80	53
NGC 6809	-1.94	1.87	0.07	2.79	0.55	4.9	492	18
NGC 6838	-0.78	0.53	0.03	2.8	1.04	2.9	256	14
NGC 6934	-1.47	1.40	0.25	1.73	0.31	4.9	45	12
NGC 6981	-1.42	0.68	0.12	1.22	0.23	3.0	21	19
NGC 7006	-1.52	1.47	0.38	1.94	0.52	4.0	43	18
NGC 7078	-2.37	4.94	0.05	1.18	0.11	13.6	1273	6
NGC 7089	-1.65	5.05	0.10	1.68	0.06	10.7	410	21
NGC 7099	-2.27	1.27	0.07	1.8	0.38	5.5	709	6

Table 3.2: Derived structural parameters for the 59 Milky Way globular clusters considered in this work. From left to right we list the GC name; metallicity (Harris, 1996, 2010); mass and associated error; mass-to-light ratio and error; (1D) central velocity dispersion; total number of stars; and total number of WAGGS stars in the sample.

the average distances of the sample stars to the cluster centres. Also, contamination from nearby sources or the unresolved cluster light can be an issue near the centres. However, as this analysis explicitly accounts for these effects, the values in this work are robust against such contamination.

Figure 3.9 shows the derived cluster masses compared to Kimmig et al. (2015); Ferraro et al. (2018); Baumgardt et al. (2019a). As before, three Kimmig et al. (2015) cluster values are largely discrepant, although for different GCs: NGCs 288, 6809, and 6838. The majority of the Ferraro et al. (2018) masses are shifted towards lower masses, which appears to be a consequence of the on-average lower dispersion measurements in the study of Ferraro et al. (2018).

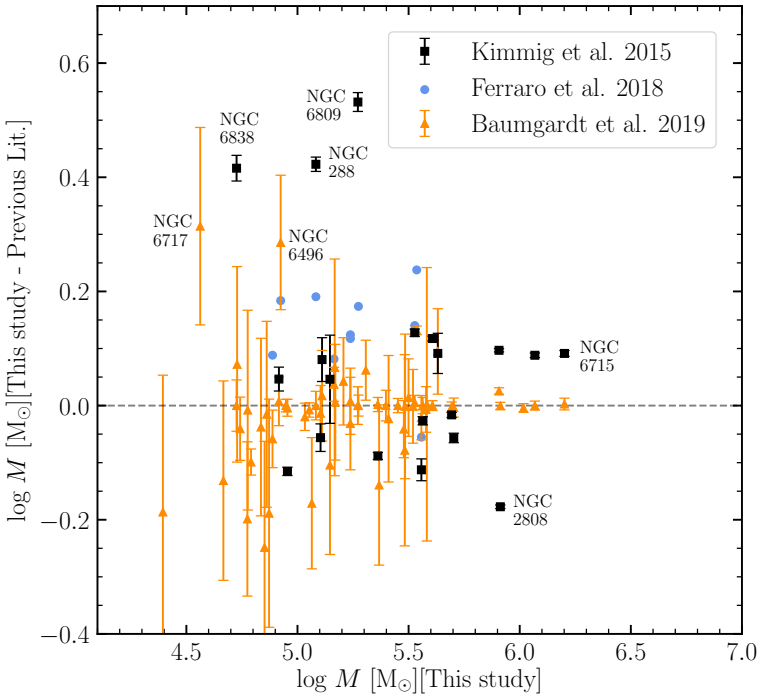

Figure 3.9: The masses of Milky Way globular clusters derived here compared to Kimmig et al. (2015); Ferraro et al. (2018); Baumgardt et al. (2019a) as in Figure 3.8. Some of the most discrepant Kimmig et al. (2015); Baumgardt et al. (2019a) GCs are labelled.

3.5 The mass-to-light ratio

The M/L depends on the proportion of high- to low-mass stars within a cluster. Massive stars contribute most of the light within a cluster, whereas the low-mass stars

and stellar remnants (white dwarfs, neutron stars and black holes) contribute most of the mass. As such, the M/L provides an important insight into stellar evolution and the stellar mass function, and is a very useful tool for checking and constraining SSP models.

The M/L_V–[Fe/H] relation of 59 Milky Way globular clusters is plotted in Figure 3.10, reaching higher metallicities than seen before: [Fe/H] > −0.4 dex. The median M/L_V is shown as a grey dashed line (1.9 $M_\odot/L_\odot$). I found no trend with [Fe/H], with Spearman's rank correlation coefficient, $\rho = -0.01$. However, even after accounting for observational errors, a cluster-to-cluster scatter is clearly visible. In particular, I note five outliers:

1. NGCs 6342 and 6453 ($M/L_V \sim 3.6$ $M_\odot/L_\odot$) both have large uncertainties, which can be explained by uncertain total cluster luminosities. Newly derived luminosities (Baumgardt, in prep) decrease the M/L_V of these clusters.

2. NGCs 6355, 6637, and 6642 have low dynamical M/L_V (< 0.9 $M_\odot/L_\odot$) and small uncertainties, also likely due to unreliable luminosities and underestimated errors. Baumgardt (in prep) finds more reliable luminosities, which lead to $M/L_V > 1$ for all four clusters. Determining accurate luminosities is difficult due to close proximity to the bulge of all three clusters (in galactocentric radius, $1.0 < R_{GC} < 1.7$ kpc).

In addition to the above, measuring M/L itself is known to be model-dependent, often with a scatter of 20% or more (e.g. Zocchi et al. 2017, Table 2, and Bellini et al. 2017, Table 8). However, such errors should not correlate with metallicity; while the errors here do not take into account systematic errors introduced by the N-body models, it is unlikely that they will counterbalance systemic offsets at high metallicity.

The observations are compared to theoretical predictions by over-plotting stellar population models (Figure 3.10; blue line). The models are calculated using version 3.0 of the Flexible Stellar Population Synthesis (FSPS) code (Conroy et al., 2009; Conroy & Gunn, 2010), MIST isochrones (Dotter, 2016; Choi et al., 2016; Paxton et al., 2011, 2013, 2015), a Kroupa (2001) IMF and the MILES spectral library (Sánchez-Blázquez et al., 2006). I also tested the UV-extended E-MILES stellar population

models from Vazdekis et al. (2016), using both the BaSTI (Pietrinferni et al., 2004) and Padova (Girardi et al., 2000) theoretical isochrones, finding good agreement between all predicted M/L_V ratios. Despite using different isochrones and stellar libraries; they all agree within < 10 %.

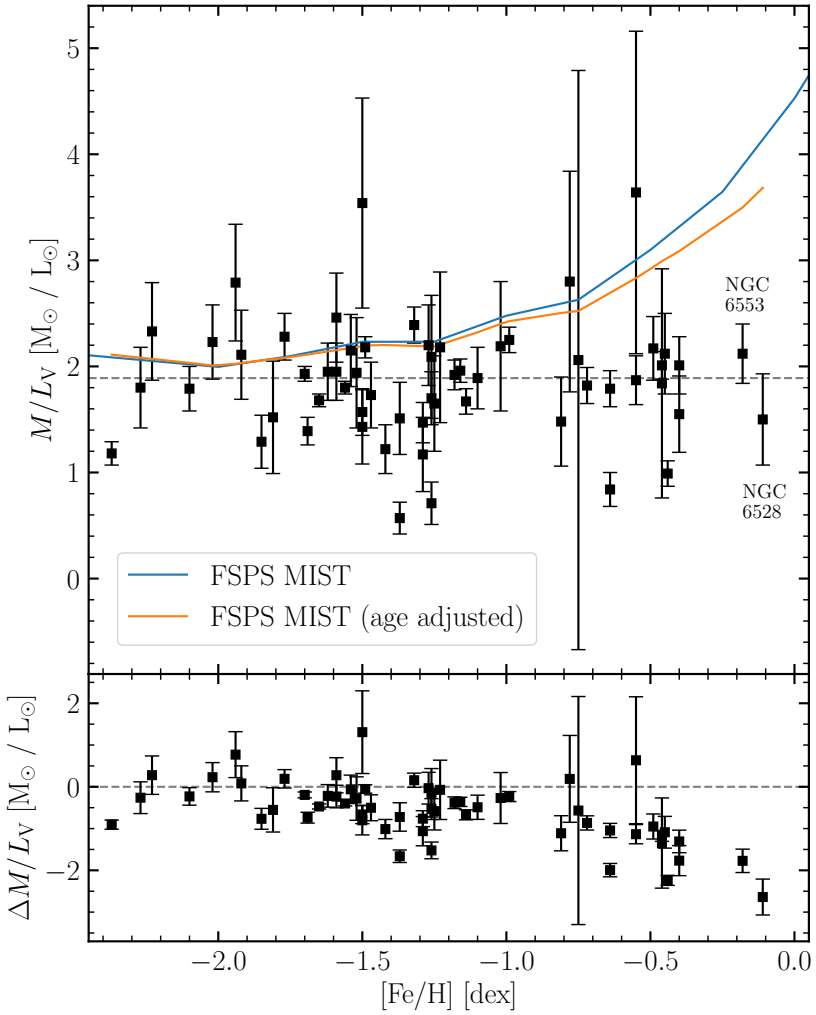

Figure 3.10: The mass-to-light ratio of Milky Way globular clusters versus metallicity. Over-plotted are the original FSPS MIST model at 12.59 Gyr (blue) and a 2D interpolated version which accounts for the age-metallicity relation derived by Kruijssen et al. (2019) (orange). The median M/L ratio is shown as a grey dashed line. The difference in M/L between each GC and the original FSPS MIST model is shown underneath.

SSP models with fixed IMFs predict that M/L increases with metallicity in the V-band, as a result of line blanketing (e.g. Bruzual & Charlot 2003; Maraston 2005). However, as the range of M/L_V versus [Fe/H] has been extended to include two clusters — NGCs 6528 and 6553 — at higher metallicity, it is clear to see that the M/L_V ratio remains

constant. The models and observations are well matched at lower metallicities, until [Fe/H] ~ -1.0 dex when they begin to diverge.

3.5.1 Comparisons to previous work

Since Strader et al. (2009, 2011) first showed the discrepancy between the M/L ratios of stellar population models and globular clusters within M31, several other studies have focused their attention on Galactic GCs (Kimmig et al., 2015; Watkins et al., 2015; Baumgardt, 2017). Kimmig et al. (2015) studied the M/L of 25 Galactic GCs, with metallicities going up to −0.46 dex. They compared their observations to SSP models at an age of 13 Gyr (Mieske et al., 2013), and found no evidence for an increase in M/L with metallicity. Watkins et al. (2015) used HST proper motions of Bellini et al. (2014) to determine dynamical M/L ratios of 15 MW clusters up to ~ -0.5 dex. They observed the same decrease in M/L as Strader et al. (2011) towards the metal-rich end. When compared to the M/L population-synthesis estimates of McLaughlin & van der Marel (2005), the metal-poor clusters agree, but offsets exist for the clusters above [Fe/H] = −1.0 dex. Baumgardt (2017) later included five GCs with $-1.0 <$ [Fe/H] < -0.3 dex, but due to large uncertainties they are uncertain if the SSP models are in fact very different to the observations at higher metallicities. Finally, Voggel et al. (2019) studied the M/L of Ultra Compact Dwarfs (UCDs). The authors showed that four UCDs — with roughly solar metallicity — also lie at a M/L below the theoretical prediction, after accounting for the impact of their supermassive black holes.

The results presented here remain consistent with previous work and add further evidence to the discrepancy between stellar population models and observations. The SSP models are typical of those used in previous literature, however, it is well known that other factors like age or the fraction of compact remnants has an effect on the M/L of a cluster, as explored in further detail in the next section.

3.5.2 Cluster ages

Older clusters have a larger fraction of evolved stars compared to younger clusters, decreasing the light emitted by a GC, and thus increasing M/L. Since the most

metal-rich GCs in the MW are ∼ 2.5 Gyr younger than the most metal-poor GCs (e.g. vandenBerg et al. 2013), one would expect that M/L will decrease at higher metallicity. Haghi et al. (2017) examined an empirical relation between age and metallicity and the effect on M/L for M31 GCs, although they required that the most metal-rich clusters have a significantly younger age than what is observed (e.g. Caldwell et al., 2011).

Here I have followed a different approach, taking the age-metallicity relation derived by Kruijssen et al. (2019) to predict the age of each GC based on its metallicity, and then interpolated to determine the empirical M/L ratio (Figure 3.10; orange line). This decreases the M/L ratio as expected, particularly from [Fe/H] = −1.0 dex and above, but not enough to account for the difference between the models and observations at the metal-rich end i.e. the influence of age is minimal. The GCs would need to be as young as ∼ 6 Gyr in order for the models to agree, similar to what Voggel et al. (2019) find for UCDs, but this is several Gyr younger than the ages measured for metal-rich Galactic GCs (e.g. vandenBerg et al. 2013). As more observations of younger LMC and SMC clusters become available, it will be possible to see how their M/L relates to older MW GCs, which may shed more light on the effect of cluster age (see Chapter 4).

3.5.3 Mass function variations

The M/L ratio of a stellar population strongly depends on its present day mass function (PDMF). Dynamical evolution or a varying IMF could alter the proportions of high- or low-mass stars present within a cluster, therefore changing the PDMF in comparison to a Kroupa IMF.

Strader et al. (2009, 2011) argued that the M/L-[Fe/H] relation cannot be due to dynamical effects since the metal-rich and metal-poor GCs of M31 are of similar mass and size. Instead they proposed different IMFs for the metal-rich and metal-poor clusters to try and explain the discrepancy. Zonoozi et al. (2016) looked at the effects of a varying IMF for M31 GCs in more detail. They found that a top-heavy IMF, in combination with other effects e.g. dynamical evolution and remnant retention (see Section 5.4 for more detail) improved the agreement between SSP models and M/L

observations.

Here, the effect of introducing a bottom-light mass function on the SSP models is explored. Using the MIST isochrones, C3K spectral library (Conroy et al. in prep), and their synthetic V-band photometry, models with three different PDMF are calculated (Figure 3.11; solid lines):

1. Kroupa IMF, $\alpha = -1.3$ ($M < 0.5\ M_\odot$), $\alpha = -2.3$ ($M > 0.5\ M_\odot$) [yellow];
2. bottom-light mass function, $\alpha = -1.3$ ($M < 1.0\ M_\odot$), $\alpha = -2.3$ ($M > 1.0\ M_\odot$) [green];
3. extreme bottom-light mass function, $\alpha = -0.3$, ($M < 1.0\ M_\odot$), $\alpha = -2.3$ ($M > 1.0\ M_\odot$) [red].

For all models the mass function between 0.08 and 100 $M_\odot$ are integrated along with the same prescription for remnant masses (Renzini & Ciotti, 1993).

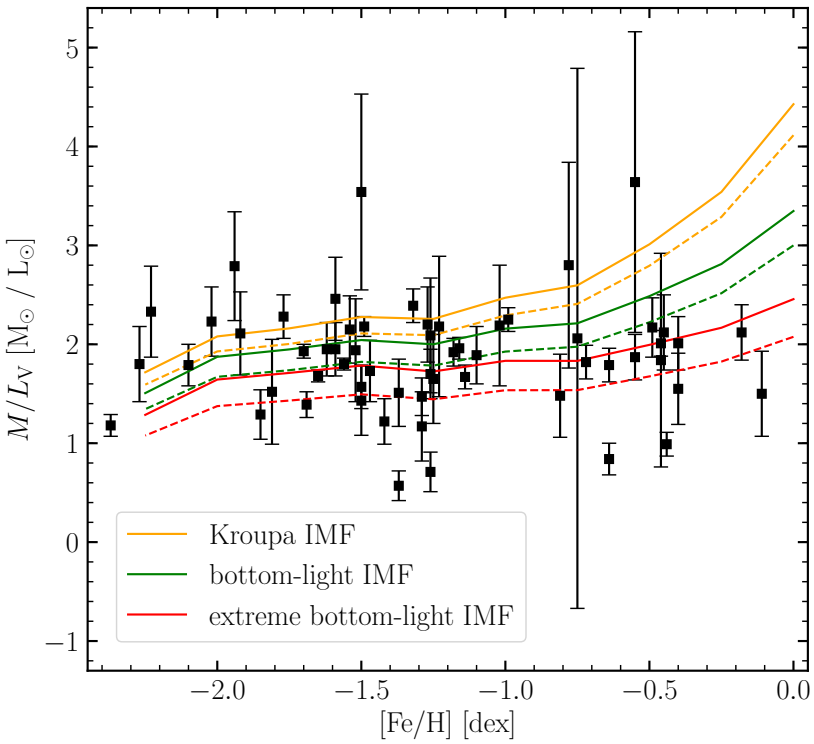

Figure 3.11: M/L of Milky Way globular clusters versus [Fe/H] for a Kroupa IMF (yellow), bottom-light mass function (green), and an extreme bottom-light mass function (red). The solid lines represent 100% retention of remnants (i.e. NSs and BHs), compared to 0% remnant retention (dashed lines).

Only the M/L of the third model are low enough to replicate the observations above −1.0 dex, however, there is strong evidence that it is nonphysical for the IMF to vary so strongly with [Fe/H] (Bastian et al., 2010). A more detailed study of the influence of the mass function is left for future work. Next, the retention of remnants as another possible effect on the M/L is explored.

3.5.4 Remnant retention

As stars evolve into remnants, M/L increases — stellar remnants continue contributing to the mass but no longer to the luminosity of a globular cluster. The strength of this effect depends on the number of remnants that are retained throughout a cluster's lifetime. It is expected that at least some proportion of compact remnants (black holes and neutron stars) will either receive a velocity kick when they form and become immediately ejected, or will eventually be expelled from the cluster as a result of dynamical evolution (e.g. Weatherford et al. 2018; Kremer et al. 2019, and references therein). These compact remnants are removed in conjunction with the evaporation of low-mass stars, a result of mass segregation.

Previous work has shown that a spread in the retention fraction of compact remnants — along with metallicity-dependent mass segregation effects — can explain the M/L-[Fe/H] discrepancy of MW clusters (Shanahan & Gieles, 2015). Other work has found that by reducing the remnant retention fraction to 30% (along with a top-heavy IMF), the discrepancy between the models and observations decreased (Zonoozi et al., 2016). The latter study explored this further by introducing a dependence on cluster mass and metallicity, which improved their SSP predictions for M31 GCs.

By adapting the models from Section 3.5.3 (which follow 100% black hole (BH) and neutron star (NS) retention), the effect of removing remnants upon the SSP models can be seen. The equivalent models for the most extreme case are calculated: 0% BH+NS retention in the range $-2.25 < [\mathrm{Fe/H}] < 0.00$ for each mass function, at an age of 12.59 Gyr (Figure 3.11; dashed lines). As expected, this has the effect of decreasing M/L_{V} for all metallicities. At [Fe/H] = 0 dex, the effect of removing all BHs and NSs is $\sim 7\%$ for a Kroupa IMF [case (i)] or $\sim 20\%$ for the bottom-light mass functions [cases (ii) and (iii)].

While a 0% BH+NS retention fraction alone is not enough to explain the discrepancy, some effect can clearly be seen. In order to better approximate the percentage of remnants retained within a cluster, it is crucial for future studies to determine the remnant fraction, particularly at the metal-rich end.

3.5.5 Other possible effects

As demonstrated in the previous sections, accounting for the younger ages of an increasingly metal-rich cluster population and testing for the effect of removing remnants both serve to decrease M/L. Yet each effect alone is not enough to explain the discrepancy between the observed and theoretically predicted M/L. Therefore, a combination of the explored effects, or some other effects must be at play.

It is already known that a strong correlation is observed between the dynamical age of a globular cluster and the low-mass slope of its mass function (e.g. Sollima & Baumgardt 2017). In other words, mass segregation leads to a preferential loss of low-mass stars in the Galactic tidal fields, impacting on the evolution of a cluster. Therefore, since metal-rich MW clusters are only found in the bulge where they are subject to significant dynamical effects, one expects that they will lose a larger fraction of low-mass stars and have a lower M/L. The N-body models used here take tidal fields into account by adjusting the initial mass function, although this approach may be limited in its accuracy.

Shanahan & Gieles (2015) found that mass segregation leads to a bias in the determination of M/L, which was not taken into account by the models of Strader et al. (2011). This bias is accounted for by the N-body models, however, so it is unlikely that this could explain the discrepancy between the observed M/L ratio and SSP models. This effect may also explain why Strader et al. (2011) find a decrease in M/L with metallicity, compared to the flat relation found here.

The dynamical evolution of a cluster also depends on its radius; GCs with small radii evolve more quickly. This is true both for Milky Way clusters and their extragalactic counterparts (see Usher et al. 2013 and references therein). Since metal-rich GCs have smaller radii on average — smaller galactocentric radii leads to stronger tidal

fields — metal-rich GCs should lose more low-mass stars, i.e. they will have a more bottom-light mass function compared to metal-poor GCs with the same mass. Thus one would expect metal-rich GCs to have lower M/L compared to the predictions of a stellar population calculated using the IMF alone.

The internal configuration of a cluster itself is also of primary importance (e.g. density, initial tidal filling configuration, relaxation time). More compact clusters evolve faster dynamically, decreasing their M/L accordingly. Bianchini et al. (2017) suggest that possible differences in internal configurations between metal-rich and metal-poor clusters (e.g. metal-rich clusters being more dense) could produce a different dynamical evolution of the M/L, thereby decreasing the M/L of metal-rich clusters. This effect could add up to the evolution due to the tidal field.

Another possible cause could lie with the shortcomings of the N-body models e.g. binaries or rotation. However, the effects due to binaries and rotation are expected to be more effectively destroyed in metal-rich clusters, since the inner metal-rich GCs are more compact. In future work, it would interesting to make a more detailed comparison between clusters in the bulge and in the halo, as a more robust test for dynamical effects upon GCs.

Finally, dark matter can be ruled out as a possible effect, as there is no evidence for dark matter in any MW globular cluster thus far (Sollima et al., 2009; Ibata et al., 2011).

3.6 Summary

In this work, I have determined 1,622 radial velocity measurements across 59 Milky Way clusters. The majority of the stars are located in the centres of GCs (within 20 arcsec), extending prior work to a new region of parameter space. Incorporating this new data, dynamical parameters have been recalculated (i.e. central velocity dispersions and masses). Importantly, two new MW clusters with [Fe/H] $\gtrsim -0.4$ dex have been introduced — where previous data had been lacking — allowing us to better understand the M/L_V-[Fe/H] relation at the metal-rich end.

These results confirm previous work by Baumgardt (2017); the mass-to-light ratio of GCs does not change with metallicity for Milky Way clusters. Subsequently, even greater divergence with SSP models is observed, strengthening the need to decipher where this discrepancy originates. Having looked at possible explanations, it seems reasonable to assume that dynamical effects have a significant part to play in the solution. Moreover, globular clusters undergo internal dynamical evolution much more rapidly than galaxies, which is further accelerated for the metal-rich clusters located in the bulge. This suggests that it is not straightforward to compare globular clusters with galaxies, particularly towards higher metallicities. Either more equivalent calibrators need to be found, or we need to improve our understanding of the dynamical processes so that they can be accounted for in the models. Further work in this area has the potential to reveal a new understanding of the dynamics of globular clusters.

Chapter 4

MC star clusters and beyond

As often as the eve returns,
Begemmed with sparkling lights on high,
I view ye in your silent spheres,
Ye lonely prisoners of the sky. George Bettner

The construction of advanced instruments — like MUSE and other IFUs — have opened up new and exciting areas of parameter space. These revolutionary tools are ideal for observing extragalactic star clusters harboured in the Milky Way's satellites, such as the Magellanic Clouds (Section 1.2.3). Spectroscopy of resolved stars within nearby MC star clusters will provide more stringent constraints on dynamical models — since they contain younger clusters, like YMCs — advancing our understanding of how star clusters form and evolve. In Section 4.1, I describe preliminary work which is an extension of the study of globular mass-to-light ratios, as carried out in the previous chapter.

Other observatories have also been catalysts for star-cluster-related discoveries. *Gaia* has triggered an avalanche of new SC-related research, which includes new Milky Way mass determinations calculated from GC orbits (Watkins et al., 2019b); improving cluster member selection at the outskirts of clusters (de Boer et al., 2019); the disruption of globular clusters into tidal streams (Price-Whelan & Bonaca, 2018; Lane et al., 2020); the discovery of new open clusters (Cantat-Gaudin et al., 2018; Cantat-Gaudin & Anders, 2020; Castro-Ginard et al., 2020); and more. One particularly

notable discovery is that of eight new *Gaia* Galactic star clusters. Their nature is so far undefined — are they old open clusters, young globulars, or something else? Are they bound or unbound? Section 4.2 considers the benefits of acquiring spectra of the *Gaia* cluster members, in order to learn how clusters evolve in the unexplored low-density regime.

4.1 The clusters in the Clouds

The Magellanic Clouds are ideal astrophysical laboratories for the study of massive star clusters in their infancy, especially since Galaxy counterparts are extremely rare. At a distance of 50 – 60 kpc, the Clouds are close enough to resolve both spatially and kinematically by modern telescopes. With this data, accurate velocity dispersions and mass-to-light ratios can be derived, which can then be compared to simple stellar population models (as in Section 3.5).

At first, many studies were dedicated to measuring the M/L of MC clusters, driven by the need to test theoretical models at younger times (Section 1.2.3). Derived via dynamical and photometric methods, the results were very difficult to obtain and subject to large uncertainties. Around 20 MC clusters were studied within a timeframe of 20 years[1]. Despite significant technological advances in recent decades, there have been very few MC M/L studies in the past 15 years[2].

Considering the data from the 20$^{\text{th}}$ century literature, Figure 4.1 looks at the change of M/L with metallicity and age (see also Table 4.2). M/L decreases with cluster age as expected, since a cluster contains significantly higher numbers of brighter stars in its youth. Overplotted are M/L predictions made by simple stellar population models (created using the E-MILES BaSTI isochrones; Pietrinferni et al. 2004; Vazdekis et al. 2016). Each line corresponds to the M/L and metallicity of a population of stars,

[1] Hodge 11, NGC 330, NGC 419, NGC 1783, NGC 1786, NGC 1818, NGC 1831, NGC 1835, NGC 1841, NGC 1850, NGC 1866, NGC 1916, NGC 1978, NGC 2005, NGC 2019, NGC 2157, NGC 2210, NGC 2257, and Reticulum (Freeman, 1974; Freeman & Gascoigne, 1977; Chun, 1978; Feast & Black, 1980; Elson & Freeman, 1985; Meylan, 1988; Dubath et al., 1990; Mateo et al., 1991; Seitzer, 1991; Meylan et al., 1991; Suntzeff et al., 1992; Fischer et al., 1993; McLaughlin & van der Marel, 2005).

[2] Kron 3, NGC 339, NGC 419, NGC 1846, NGC 2121, and NGC 2193 (Mackey et al., 2013; Zaritsky et al., 2014; Kamann et al., 2018b; Song et al., 2019).

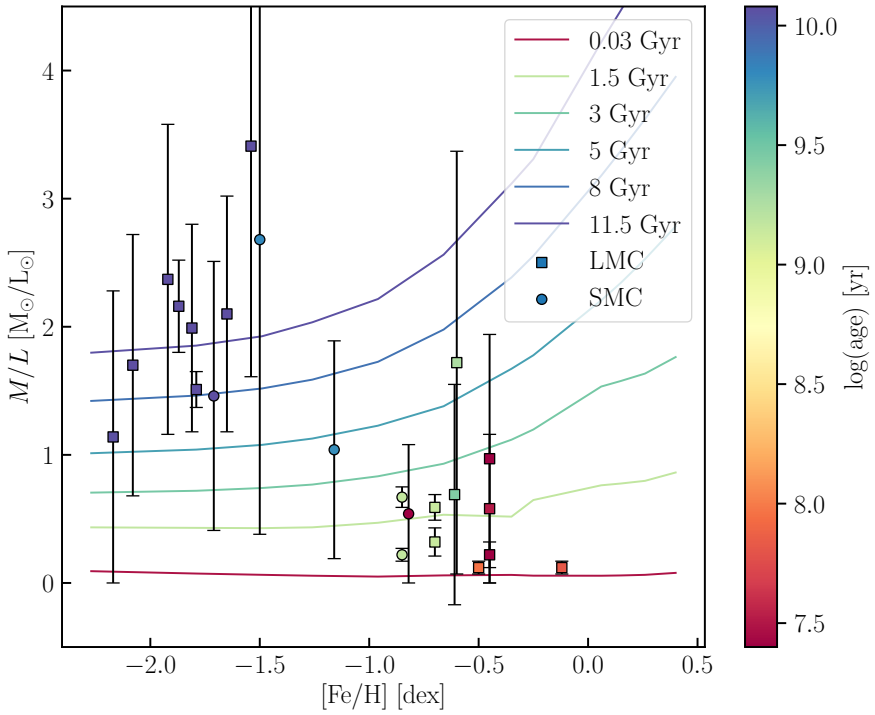

Figure 4.1: Mass-to-light ratios of 22 massive Magellanic Cloud star clusters (NGC 1846 and NGC 419 have been measured twice). NGC 2257 is not shown as it appears to be an outlier with a M/L of 10.21 $M_\odot/L_\odot$. LMC clusters are represented by squares, and SMC clusters by circles. The youngest cluster, NGC 330, has an age of 25 Myr, whereas the oldest clusters are almost 13 Gyr. Overplotted are simple stellar population models at different ages (Pietrinferni et al., 2004; Vazdekis et al., 2016). M/L decreases with age as expected, although the high uncertainties make it difficult to compare to predicted M/L; this highlights the need for more accurate results. Literature values are listed in Table 4.2, obtained from McLaughlin & van der Marel (2005); Mackey et al. (2013); Zaritsky et al. (2014); Kamann et al. (2018b); Song et al. (2019).

increasing with time: 30 Myr, 1.5 Gyr, 3 Gyr, 5 Gyr, 8 Gyr, and 11.5 Gyr, which coincides with the age distribution of Magellanic Cloud star clusters. It is clear to see that the majority of observed mass-to-light ratios come with large uncertainties. Thus it is difficult to confirm whether or not they agree with the expected M/L for a given age, which motivates a strong case for future work in this area. The M/L values for NGC 419 ([Fe/H] = −0.85 dex) are also worth highlighting: despite small errors they contradict one another.

One can also notice that the vast majority of MC SCs have unknown M/L, since the Clouds are expected to contain at least 100 massive clusters (Mackey, 2009). As described in Section 3.2, WAGGS is an integral-field survey of star clusters in the Galaxy and Local Group; the data include several SCs in the Large and Small

Magellanic Clouds. Of these, I selected a sample of fourteen clusters[3] which cover a range of ages, metallicities, and radii from the Cloud centres. The clusters were observed between 2015–2018 with WiFeS (Usher et al., 2017, 2019); additional observations of NGC 1850 were carried out between 10th–13th September 2018 and were reduced in the same way. Figure 4.2 shows the different pointings used — the data from the fields labelled WAGGS, 1, 2 and 3 have been used for this study.

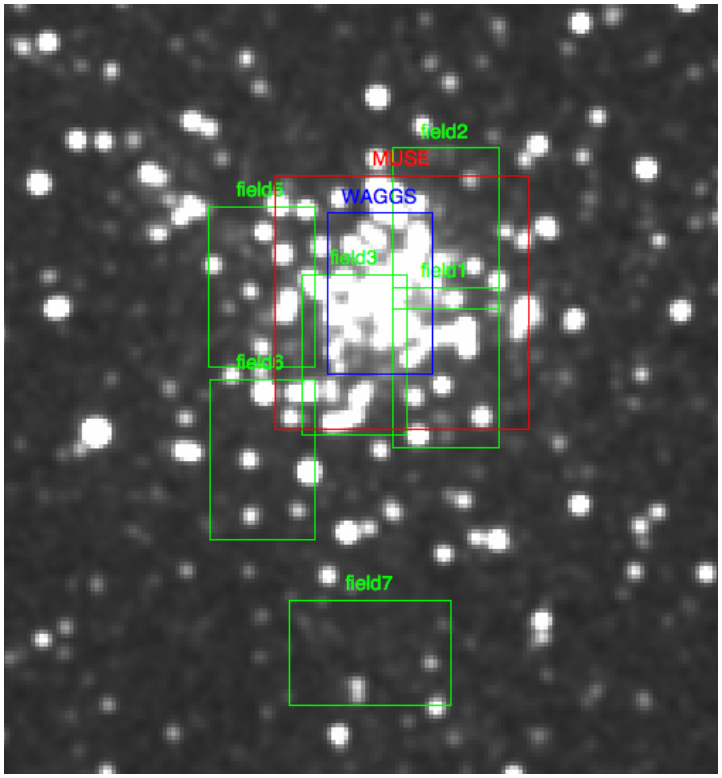

Figure 4.2: Pointings used for the observations of NGC 1850. The fields used in this study are WAGGS, 1, 2, and 3.

HST photometry is available for the selected clusters, required for extracting the spectra from the datacubes (Table 4.1). Several of the photometric catalogues were missing WCS coordinates (NGCs 121, 330, 411, 1831, 1866, 1978, 2100, 2136), so I calculated RA and Dec by cross-correlating the data with stars in the *Gaia* DR2 database using `CataXcorr` (Montegriffo et al., 1995). Following the same procedure as Section 3.3, I extracted spectra from the datacubes using PampelMuse (Kamann et al., 2013). For three of the clusters, the datacubes and/or photometry are of too poor quality to extract reliable spectra; they are excluded from further analysis. The

[3]NGC 121, NGC 330, NGC 411, NGC 416, NGC 419, NGC 1783, NGC 1831, NGC 1846, NGC 1850, NGC 1856, NGC 1866, NGC 1978, NGC 2100, NGC 2136.

remaining eleven clusters and their ages and distributions in the sky are shown in Figure 4.3.

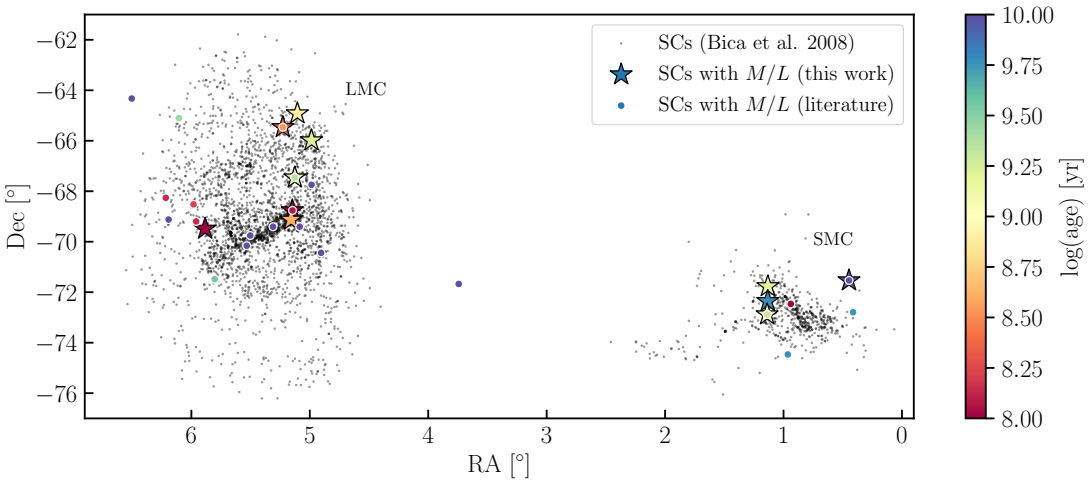

Figure 4.3: Massive star clusters in the Large and Small Magellanic Clouds. Grey dots are all the SCs listed in Bica et al. (2008). Massive star clusters observed by previous M/L studies are labelled as filled circles (see Figure 4.1), and the selected WAGGS sample are highlighted by large coloured stars. The ages of the clusters range from 10 Myr to 10 Gyr.

Next, the extracted spectra are cross-correlated with a model spectra (using the IRAF task `FXCOR`) in order to calculate the radial velocity of each star. Compared to the study of Dalgleish et al. (2020), the new MC sample contains clusters with young stars, and so they reach high effective temperatures ($> 8,000$ K), which lie beyond the limit of the publicly available medium resolution PHOENIX template spectra (Husser et al., 2013). Instead, I employed POLLUX synthetic spectra for the out-of-range stars (Palacios et al., 2010). Further tests are needed to inspect how the radial velocities compare between the two spectral catalogues. After determining radial velocities for the extracted spectra across all clusters, I filtered out the inaccurate data as before. Cuts of $S/N = 6.7$ and $TDR = 18$ yield good results and a total of 361 spectra across all four gratings (Figure 4.4). Then the velocities are shifted across the gratings to correct for systematic night differences (Figure 4.5) before applying a sigma cut ($\sigma = 3$) to remove any outliers. Afterwards, I averaged the velocities for each star (see Appendix B for plots of radial velocity against distance to the cluster centre). Finally, some preliminary velocity dispersions have been calculated for each cluster, using the method of Pryor & Meylan (1993); three clusters have too few stars and so the velocity dispersion cannot be deduced. These values can be found in Table 4.1.

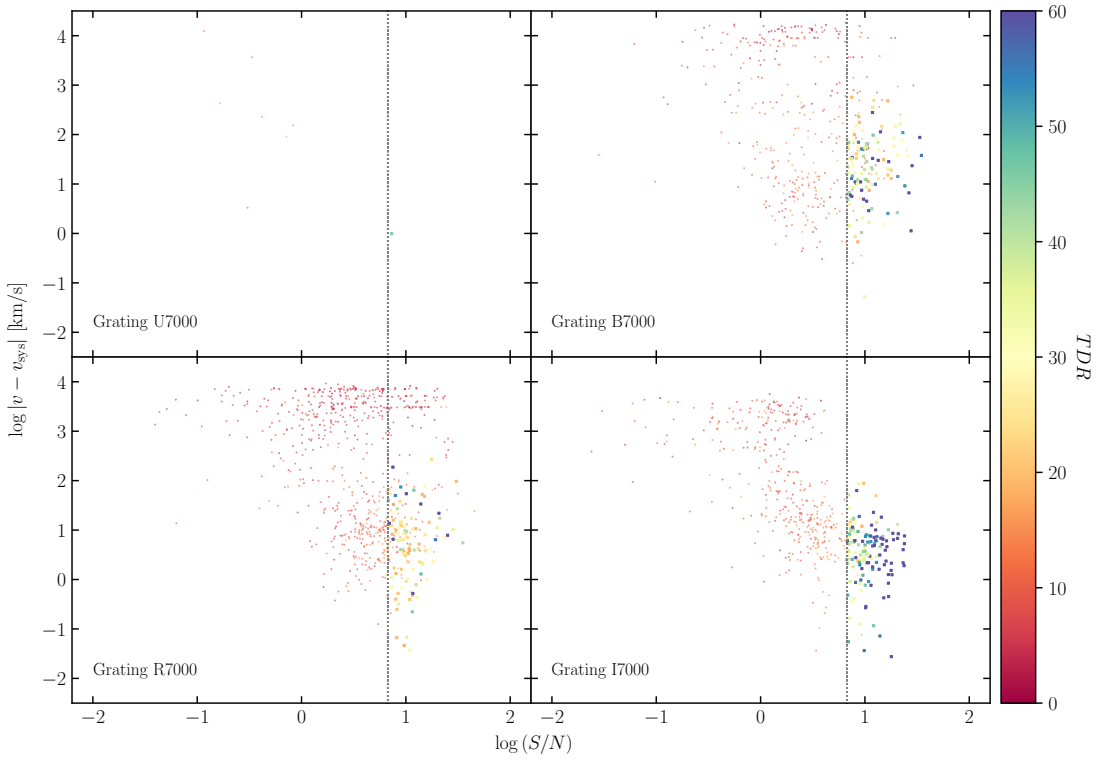

Figure 4.4: The absolute difference in velocity (w.r.t. systemic velocity) versus S/N, for spectra across all clusters, in log-log space. Cutoffs are applied at $S/N = 6.7$ and $TDR = 18$. The dots represent velocities which are deemed unreliable, as opposed to the coloured squares which are kept for further data analysis.

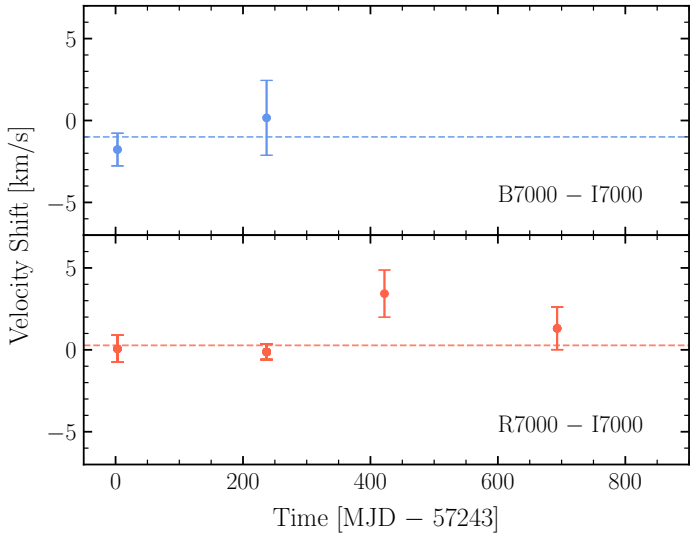

Figure 4.5: The average shift in velocity in the B7000 (blue) and R7000 (red) gratings with respect to the I7000 grating. The average velocity shift is shown as a dashed line. Shifts are calculated by taking the differences in velocity measurements that are associated with the same star and then averaging over all the velocity differences from all stars (irrespective of cluster) for each night.

Comparing these preliminary results to previous literature, the derived velocity dispersions seem to be around twice as high. For NGC 419, Kamann et al. (2018b) and Song et al. (2019) find values of $\sigma_{1D} = 3.10 \pm 0.20$ and 2.44 ± 0.37 km/s, respectively. Song et al. (2019) give a mean velocity of 189.5 km/s which is in very good agreement to the result calculated here. For NGC 1846, $\sigma_{1D} = 2.52 \pm 0.26$ (Mackey et al., 2013) and $\sigma_{1D} = 2.04 \pm 0.28$ (Song et al., 2019). The later authors give a mean velocity of 239.0 km/s.

Name	Photometry source	N_{stars}	$< v >$ [km/s]	σ_{1D} [km/s]
NGC 121	Niederhofer et al. (2017)	42	142.45±0.92	5.38±0.76
NGC 411	Girardi et al. (2013)	15	156.44±0.88	2.72±0.99
NGC 416	Martocchia et al. (in prep)	5	150.38±5.30	–
NGC 419	Martocchia et al. (2017)	19	188.54±1.57	6.58±1.47
NGC 1783	Saracino et al. (2020)	25	278.07±0.90	3.97±0.82
NGC 1831	Niederhofer et al. (2015)	2	–	–
NGC 1846	Martocchia et al. (2018)	16	243.04±1.63	6.44±1.54
NGC 1850	Bastian et al. (2016)	130	248.11±3.62	40.56±2.72
NGC 1856	Correnti et al. (2015)	27	262.65±0.96	3.98±0.96
NGC 1866	Unpublished. Method as in Niederhofer et al. (2017)	60	302.12±0.86	6.35±0.69
NGC 2136	Niederhofer et al. (2015)	6	277.17±6.34	–

Table 4.1: Sources for the reference catalogues used to extract spectra from the WAGGS datacubes. Also included are the number of stars used to calculate the mean velocity of the cluster, as well as the projected velocity dispersion.

Analysis is ongoing; in the future I will combine the data with line-of-sight velocities from previous literature and implement theoretical models using LIMEPY (Lowered Isothermal Model Explorer in PYthon; Gieles & Zocchi 2015). Finally, I will determine masses and mass-to-light ratios from the velocity dispersion, with the aim to analyse the M/L-[Fe/H] relation for the Cloud clusters in more detail. It will also be valuable to see how the data compares to Galactic and M31 GCs, and try to construct a universal understanding of how M/L changes according to age and other physical attributes.

NGC 1850: an extraordinarily high velocity dispersion

Although the mean radial velocity for NGC 1850 is within the errors of previous results ($< v > = 251.4 \pm 2.0$ km/s; Fischer et al. 1993), the velocity dispersion is significantly higher than expected. This value is more than ten times greater than what McLaughlin & van der Marel (2005) find ($\sigma_{1D} = 3.00 \pm 0.70$ km/s, based on star counts and density profiles). Figure 4.6 shows how the stars (and their associated line-of-sight velocities) are distributed, in terms of colour and location.

The most plausible explanation for the high σ_{1D} is the presence of undetected binaries. Previous work has already shown that binaries can dominate the velocity dispersions of YMCs (e.g. Hénault-Brunet et al. 2012 and their study of R136). This is because the binary fraction is a strong function of stellar mass — high-mass stars (which are more frequent in YMCs) have a higher binary frequency. High-mass stars are also more likely to materialise as equal mass binaries, which further exacerbates the radial velocity variations, thereby inflating the velocity dispersion even more.

In order to determine which stars are true binaries, observations are needed across multiple epochs. Fortunately there also exists MUSE data for NGC 1850, therefore, it should be possible to detect the majority of binaries through comparisons to the WAGGS data (and between the different epochs of the MUSE data). Calculating the true fraction of binaries in YMCs like NGC 1850 is also desirable as tests against predictions made by theoretical simulations are needed (e.g. D'Antona et al. 2017).

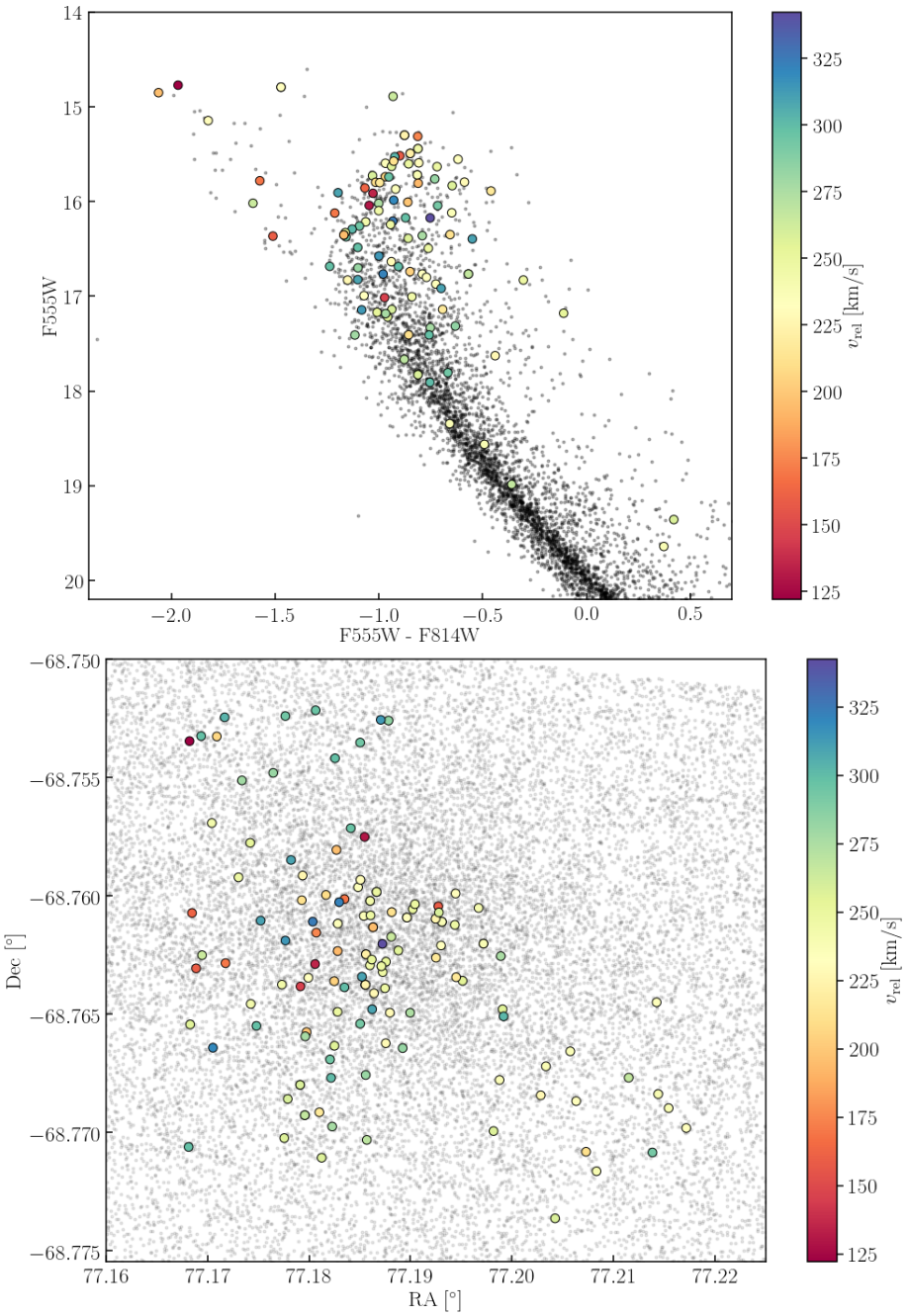

Figure 4.6: The distribution of stars in the centre of NGC 1850 on a CMD (top) and as projected on the sky (bottom). The projection includes only the cluster core. Filled circles are the stars coloured according to radial velocity. Grey dots are stars from *HST* photometry (Bastian et al., 2016).

4.2 Eight newly discovered *Gaia* clusters

Gaia, one of ESA's newest observatories, has uncovered the existence of star clusters in areas of parameter space where sizes and luminosities have never been explored.

Name	Host	RA	Dec	Age	[Fe/H]	M/L_V	Ref.
		[h m s]	[° ′ ″]	[log(Gyr)]	[dex]	[$M_\odot/L_\odot$]	
NGC 1466	LMC	03 44 33.0	-71 40 18	10.10	-2.17	1.14	1
NGC 1754	LMC	04 54 17.0	-70 26 30	10.11	-1.54	3.56	1
NGC 1783	LMC	04 59 08.6	-65 59 16	10.23	-0.50	–	6
NGC 1786	LMC	04 59 07.8	-67 44 43	10.11	-1.87	2.17	1
NGC 1831	LMC	05 06 17.4	-64 55 11	9.90	-0.17	–	6
NGC 1835	LMC	05 05 07.0	-69 24 14	10.11	-1.79	1.54	1
NGC 1846	LMC	05 07 34.9	-67 27 32	9.23	-0.70	0.59	2
	...	...	...	...	...	0.32	5
	...	...	...	...	...	–	6
NGC 1850	LMC	05 08 45.8	-68 45 39	8.00	-0.12	0.12	1
	...	...	...	...	...	–	6
NGC 1856	LMC	05 09 30.3	-69 07 45	9.60	-0.30	–	6
NGC 1866	LMC	05 13 38.9	-65 27 52	8.12	-0.50	0.12	1
	...	...	...	...	...	–	6
NGC 1916	LMC	05 18 37.9	-69 24 23	10.11	-2.08	1.71	1
NGC 2005	LMC	05 30 10.4	-69 45 10	10.11	-1.92	4.03	1
NGC 2019	LMC	05 31 56.5	-70 09 33	10.11	-1.81	2.03	1
NGC 2121	LMC	05 48 11.6	-71 28 51	9.51	-0.61	0.56	3
NGC 2136	LMC	05 53 01.8	-69 29 24	9.00	-0.40	–	6
NGC 2157	LMC	05 57 34.0	-69 11 48	7.60	-0.45	0.22	1
NGC 2164	LMC	05 58 54.0	-68 31 06	7.70	-0.45	0.59	1
NGC 2193	LMC	06 06 17.0	-65 05 54	9.34	-0.60	1.72	3
NGC 2210	LMC	06 11 31.5	-69 07 17	10.11	-1.97	2.12	1
NGC 2214	LMC	06 12 57.0	-68 15 36	7.60	-0.45	0.98	1
NGC 2257	LMC	06 30 12.0	-64 19 36	10.11	-1.63	10.21	1
Kron 3	SMC	00 24 46.4	-72 47 37	9.78	-1.16	1.04	3
NGC 121	SMC	00 26 49.0	-71 32 10	10.08	-1.71	1.46	1
	...	...	...	...	...	–	6
NGC 330	SMC	00 56 18.7	-72 27 50	7.40	-0.82	0.54	1
NGC 339	SMC	00 57 48.9	-74 28 00	9.80	-1.50	2.68	3
NGC 411	SMC	01 07 56.0	-71 46 05	10.18	-0.80	–	6
NGC 416	SMC	01 07 59.0	-72 21 20	10.78	-1.00	–	6
NGC 419	SMC	01 08 17.8	-72 53 03	9.16	-0.85	0.67	4
	...	...	...	...	...	0.22	5
	...	...	...	...	...	–	6

Table 4.2: Mass-to-light ratios of massive star clusters in the Magellanic Clouds. References: (1) McLaughlin & van der Marel (2005); (2) Mackey et al. (2013); (3) Zaritsky et al. (2014); (4) Kamann et al. (2018b); (5) Song et al. (2019); (6) this work.

Koposov et al. (2017) searched for stellar overdensities in Data Release 1, with the aim to find ultrafaint dwarf galaxies. Instead, the authors found two new star clusters in the Milky Way, *Gaia 1* and *Gaia 2*. The discovery of *Gaia 1* is particularly unexpected given its size ($M > 10^4$ $M_\odot$) and proximity (d = 4.6 kpc); the cluster had been concealed for so long because of the bright star Sirius, situated a mere 10 arcmin

away. Since then, eight more *Gaia* clusters have been revealed (Torrealba et al., 2019; Bastian, 2019). Apart from being compact (half-light radius, $r_h < 2$ arcmin) and faint ($M_V > -3$ mag), these objects are difficult to classify: are they old open clusters, or young globulars?

Of the eight new *Gaia* candidates, *Gaia 1* is the only cluster to have been followed up spectroscopically (Simpson et al., 2017). The study confirmed that *Gaia 1* is kinematically distinct, however, they found a significantly different age and metallicity (3 Gyr and [Fe/H] = −0.13 dex) compared to initial estimates (6 Gyr and [Fe/H] = −0.7 dex; Koposov et al. 2017). This emphasises a need for spectra in order to not only confirm if a cluster is genuine, but also to determine its physical parameters more precisely.

One cluster is particularly intriguing: *Gaia 2*. Initial guesses have been made regarding its nature, but it remains unclear whether the star cluster is an old open cluster, a young globular cluster (GC), or even an ultra-faint dwarf (UFD) galaxy.

4.2.1 Determining the nature of *Gaia 2*

Gaia 2 is different to *Gaia 1* in all respects. *Gaia 2* is located in the northern hemisphere, and it is much smaller (r_h = 1.9 vs 6.5 arcmin) and fainter (M_V = −2 vs −5 mag). If initial estimates are correct, its age and metallicity are 8 Gyr and −0.6 dex, respectively. *Gaia 2*'s low brightness and small size makes it a peculiar and interesting system for further study (Figure 4.7). But what is most remarkable, is its close proximity to the Galactic disc. It is surprising to find such a (low-mass) cluster which has survived so long, where tidal interactions are high. If *Gaia 2* is indeed a star cluster, this implies that it is approaching a final stage of dynamical evolution, and it is on the cusp of dissolution. Hence, the first aim would be to acquire radial velocity measurements in order to determine if *Gaia 2* is bound or unbound.

Spectra of *Gaia 2*'s cluster members would enable a study of its origins and the determination of its fundamental parameters. Additionally, spectroscopy allows for more precise measurements of age and metallicity. With this information it would be possible to ascertain whether or not a metallicity spread exists — if a large metallicity

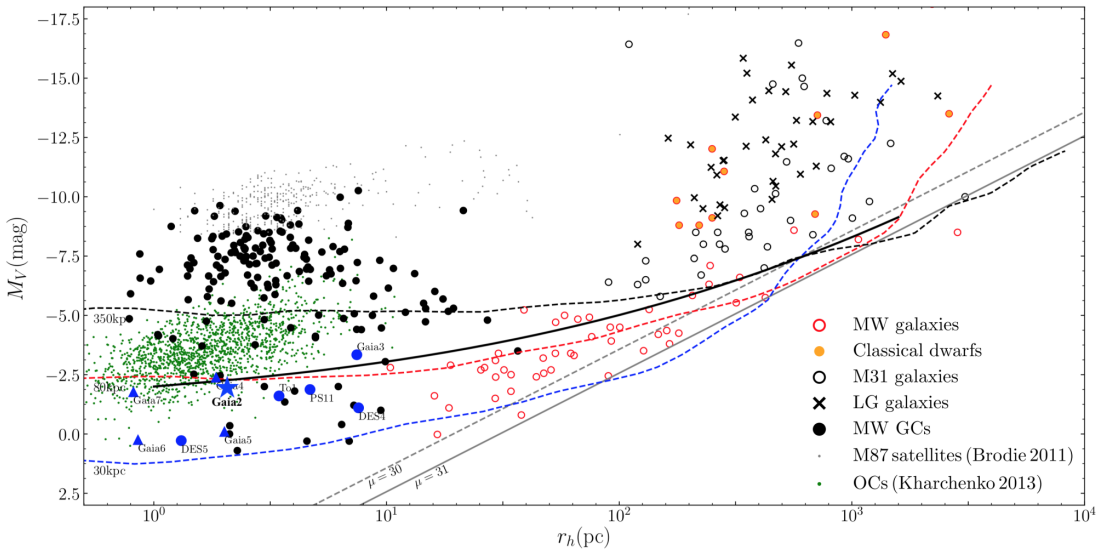

Figure 4.7: Absolute light versus half light radius diagram. *Gaia 2* is overplotted at the bottom left of the diagram (blue star), just beyond the effective detection boundary of known MW satellites by *Gaia* DR1. The newest discoveries are shown in blue, of which those in the Galactic disc are marked as triangles. They comprise the smallest and lowest luminosity star systems in the Milky Way and are thus difficult to classify. Reproduced from Torrealba et al. (2019), Figure 5.

spread is present, this would mean that *Gaia 2* is a UFD (e.g. Kirby et al. 2008), whereas a mono-metallic distribution would indicate a cluster. If *Gaia 2* is indeed an ultra-faint dwarf, this would have strong implications, since it should not be possible for UFDs to exist so close to the Galactic disc. An enhanced metallicity measurement can also pinpoint age and initial mass — the older the cluster, the more massive it must have been to survive in the MW tidal field to today. This information will hold vital clues about the formation history of star clusters in the Milky Way (e.g. Elmegreen & Efremov 1997). Finally, if *Gaia 2* is in fact a GC on the verge of evaporation, a greater understanding of dynamics at this stage will prove useful for understanding clusters as a whole, providing new constraints for dynamical models.

In order to carry out this work and further our knowledge of cluster evolution in the low-mass regime, spectra of the red giant branch and bright main-sequence stars in *Gaia 2* are needed. One such instrument which would be ideal to observe the mystery object is DOLORES, a MOS on the Telescopio Nazionale Galileo (TNG) in La Palma. The wavelength range of the V860 grism covers the calcium triplet (CaT; λ = 8498 Å, 8542 Å, and 8662 Å) with spectral resolution, R = 4000. High resolution is important for (1) reliable metalicity measurements based on the CaT lines (e.g. Usher et al. 2019)

and (2) procuring accurate velocity measurements (within 1 – 2 km/s), needed for the accurate study of cluster kinematics. By isolating *Gaia 2*'s location in proper motion space using DR2, I have identified ∼ 45 of the brightest cluster member candidates ($M_I < 18$), ideal for spectroscopic observations. Figure 4.8 shows the CMD which supports the existence of the cluster; the stellar distribution in space is also illustrated.

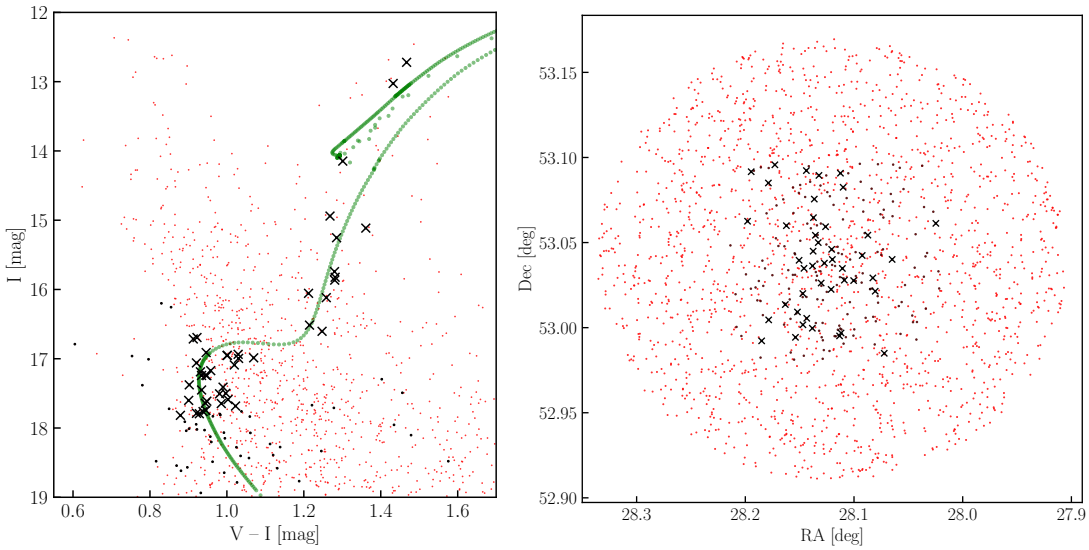

Figure 4.8: *Gaia 2* colour magnitude diagram (left) and as it appears in the sky (right). Black crosses are the target stars. Black dots are other cluster members and red dots are field stars. The green line shows a theoretical MIST isochrone, with an age of 6 Gyr and metallicity of −0.6 dex, as estimated by Koposov et al. (2017).

Overall, with spectroscopic data, this would be the first kinematical study of a cluster in the sparsely populated area of size-luminosity space.

Chapter 5

Summary and Future Outlook

> *The world of learning is so broad, and the human soul is so limited in power! We reach forth and strain every nerve, but we seize only a bit of the curtain that hides the infinite from us.*
>
> Maria Mitchell

Star clusters have captivated astronomers for centuries, and they continue to provide new and exciting avenues of research. Beginning with the advent of the telescope, Chapter 1 describes the discovery of star clusters and how they were not gaseous nebulae as ancient astronomers had originally thought. Followed by the invention of spectroscopy and photography in the late 19th-century, astronomers were able to discern not only what star clusters are made of, but also their radial velocity, leading to the study of kinematics. Our understanding of star cluster dynamics rapidly improved in the 20th-century, aided by new instrumentational techniques like cross-correlation, numerical modelling, and the invention of CCDs.

Developments in radio astronomy and the discovery of radio recombination lines also proved useful for the understanding of star clusters, especially at much earlier evolutionary times. Chapter 2 focuses on the RRLs of a young H II region in the Galactic disc, namely G316.81–0.06. The star-forming regions appears to be rotating, a phenomenon rarely observed at this stage of evolution. To probe further, I compared the observations to hydrodynamical simulations of an H II region with similar physical characteristics, and deduced a possible formation scenario which explains the origin

of the detected rotational signature. Further dynamical studies of star-forming regions at these early times should also help to reveal further insights to the formation of the older star clusters we observe in the Milky Way today.

Another way to uncover information about how star clusters have evolved is through kinematical studies of the star clusters themselves. Making use of new IFS technology, Chapter 3 looks at the mass-to-light ratios of metal-rich GCs in the Milky Way for the first time. The results confirmed a discrepancy between the observed and theoretical M/L–[Fe/H] relation. With this information, I was able to explore several possibilities as to why the observed relationship between M/L and metallicity is in disagreement. I found strong evidence which suggests that dynamical effects are the likely cause, due to the location of the metal-rich MW clusters in the bulge. Here, the clusters are more heavily influenced by internal and external dynamical forces, which have not been included in the stellar population models. With current technology, this can now be further tested through the examination of Magellanic Cloud clusters, via comparisons to GCs in the Milky Way and in M31. Additionally, there have been few observational studies focused on the effect of age on the mass-to-light ratio, making the MCs ideal for such work (Chapter 4).

Looking to the near future, more ambitious star cluster projects will become possible with the development of two new IFUs. The Southern African Large Telescope (SALT) is planning to implement a near-IR IFU in 2021, which will cover the J- and H-bands with medium resolution (Wolf et al., 2018). This is particularly exciting because the IFU will be able to peer through dust and observe stars in the central regions of clusters which are heavily obscured. It has also been suggested that we may be missing several massive clusters in the MW because of high extinction toward the bulge and disc. For example, Glimpse-C01 is a poorly studied massive cluster in the Galaxy disc, and has an age of only 400-800 Myr (Davies et al., 2011). The second upcoming IFU will be HARMONI, under construction for the Extremely Large Telescope (Thatte et al., 2014; Rodrigues et al., 2018). It will also operate in the near-IR and will be ideal for the study of extragalactic star clusters, beyond the Magellanic Clouds (e.g. Gonzalez & Battaglia 2018). Such observations will be crucial to clarify whether or not young massive clusters are truly analogues of young GCs (Renaud, 2020).

Appendix A

Masers in G316.81–0.06

Listed are the literature velocities of hydroxyl, class II methanol, and water masers present near the H II region, G316.81–0.06.

RA (J2000)	Dec (J2000)	Maser Type	v_{peak} (km s^{-1})	References
14 45 26.6	-59 49 14	Hydroxyl	−36.7	McGee et al. (1967)
14 45 27.6	-59 49 49	...	−41.0	Caswell & Haynes (1987a)
14 45 26.3	-59 49 15	...	−44.0	Caswell (1998)
14 45 26.3	-59 49 15	...	−43.5	Breen et al. (2010b)
14 45 27.6	-59 49 49	Class II methanol	−44.0	MacLeod & Gaylard (1992)
14 45 27.9	-59 49 13	...	−42.1	Caswell et al. (1995a)
14 45 27.9	-59 49 13	...	−46.8	Caswell et al. (1995b)
14 45 27.9	-59 49 13	...	−45.7	Caswell et al. (1995c)
14 45 28.0	-59 49 12	...	−46.0	Walsh et al. (1997)
14 45 26.4	-59 49 16	...	−42.2	Walsh et al. (1998)
14 45 26.4	-59 49 17	...	−44.9	Walsh et al. (1998)
14 45 26.4	-59 49 16	...	−45.8	Walsh et al. (1998)
14 45 26.4	-59 49 16	...	−46.9	Walsh et al. (1998)
14 45 26.4	-59 49 16	...	−48.1	Walsh et al. (1998)
14 45 26.4	-59 49 17	...	−46.0	Pestalozzi et al. (2005)
14 45 26.4	-59 49 16	...	−46.3	Caswell (2009)
14 45 26.4	-59 49 16	...	−46.3	Breen et al. (2010b)
14 45 26.4	-59 49 16	...	−45.8	Green et al. (2012)
14 45 30.3	-59 51 52	Water	−48.6	Kaufmann et al. (1976)
14 45 25.0	-59 49 31	...	−46.0	Batchelor et al. (1980)
14 45 26.6	-59 49 14	...	−46.0	Breen et al. (2010b)
14 45 25.5	-59 49 18	...	−47.2	Walsh et al. (2011)
14 45 26.1	-59 49 20	...	−50.6	Walsh et al. (2014)
14 45 26.4	-59 49 15	...	−45.5	Walsh et al. (2014)
14 45 26.4	-59 49 15	...	−40.9	Walsh et al. (2014)
14 45 26.4	-59 49 16	...	−39.2	Walsh et al. (2014)
14 45 26.4	-59 49 15	...	−34.6	Walsh et al. (2014)

Table A.1: Masers found in close proximity to G316.81–0.06.

Appendix B

Stellar velocities in MC SCs

Illustrated below are the distributions of stellar velocities derived from a sample of eleven WAGGS clusters in the Magellanic Clouds.

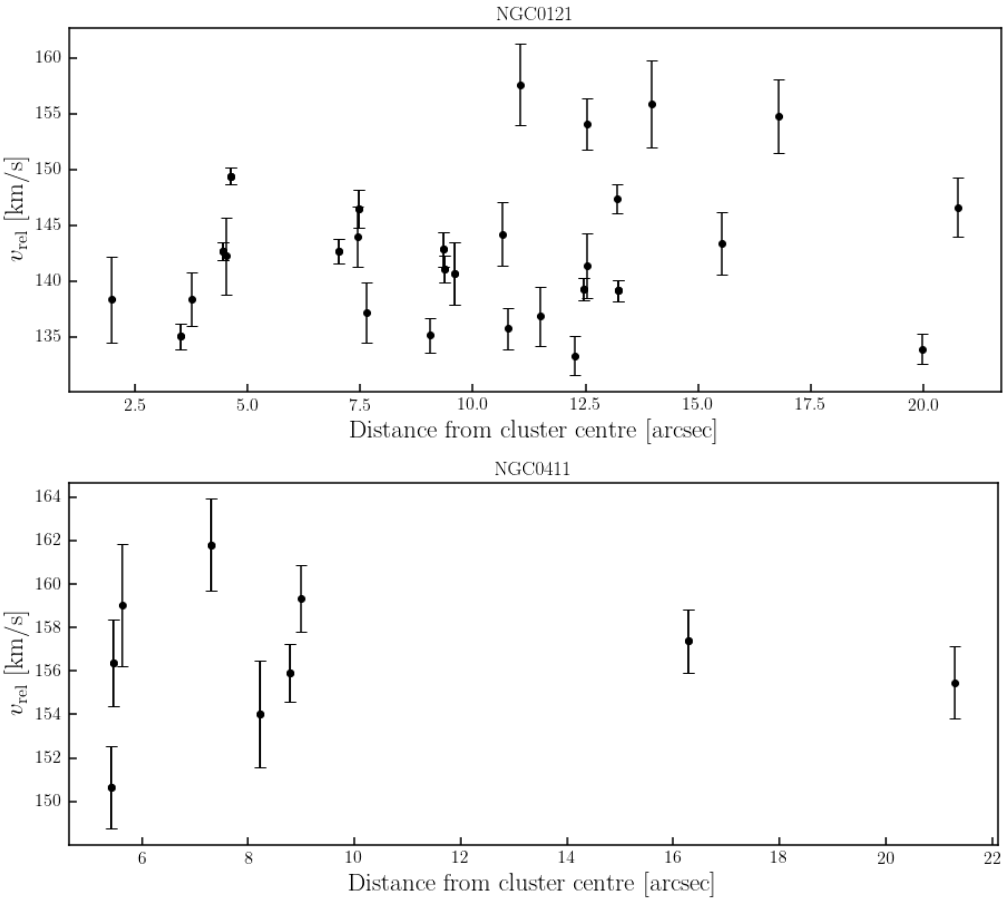

Figure B.1: The distribution of velocities in NGC 121 and NGC 411.

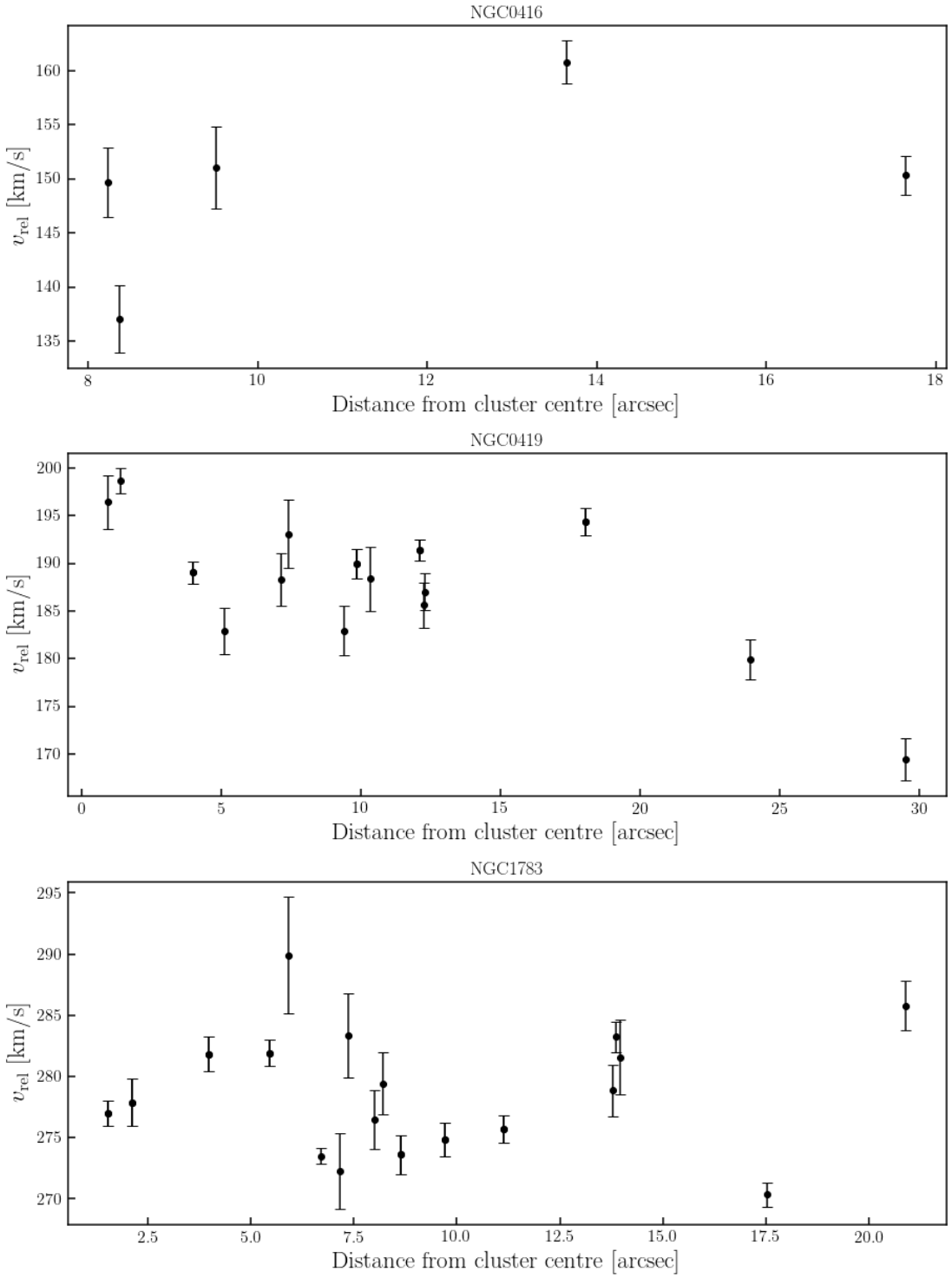

Figure B.1: The distribution of velocities in NGC 416, NGC 419 and NGC 1783.

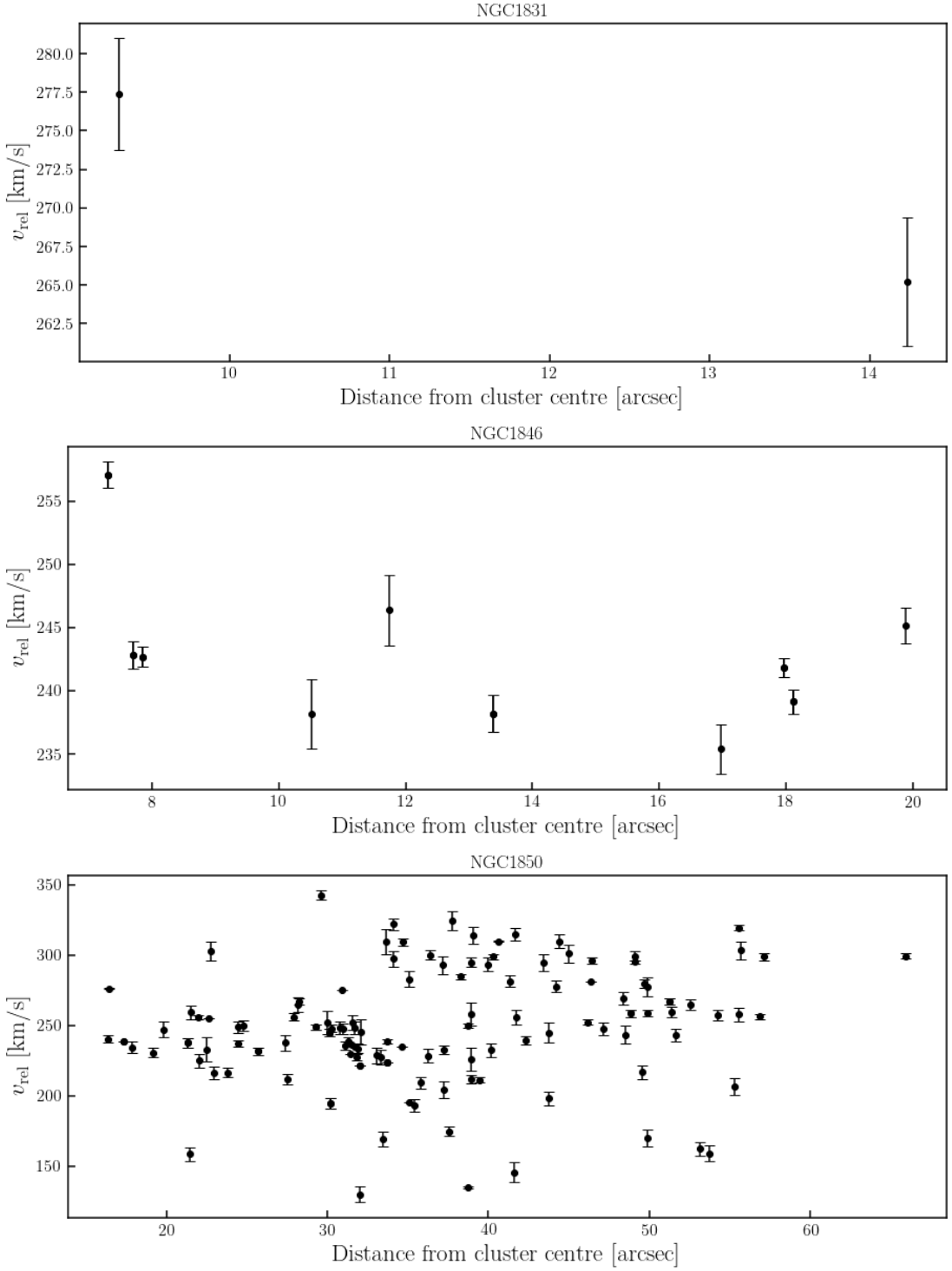

Figure B.1: The distribution of velocities in NGC 1831, NGC 1846 and NGC 1850.

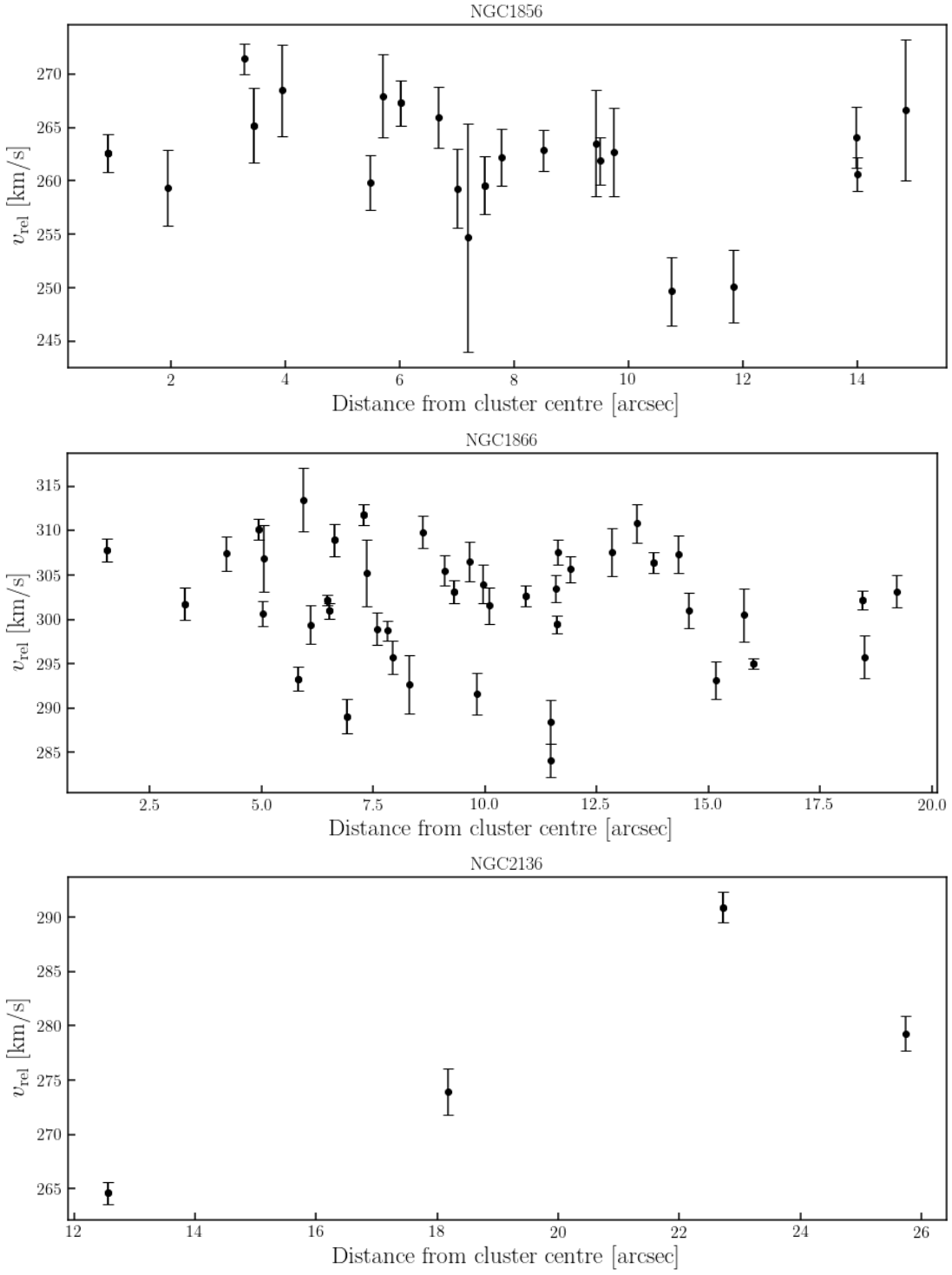

Figure B.1: The distribution of velocities in NGC 1856, NGC 1866 and NGC 2136.

Bibliography

Adams W. S., Joy A. H., Sanford R. F., Stromberg G., 1929, ApJ, 70, 207

Agertz O., Kravtsov A. V., 2016, ApJ, 824, 79

Agertz O., Kravtsov A. V., Leitner S. N., Gnedin N. Y., 2013, ApJ, 770, 25

Albrow M. D., De Marchi G., Sahu K. C., 2002, ApJ, 579, 660

Aliakberov K. D., Berlin A. B., Golnev V. Y., Lipovka N. M., Mingaliev M. G., Nizhelskii N. A., Sharipova L. M., Spangenberg E. E., 1985, Soviet Ast., 29, 281

Altenhoff W. J., Strittmatter P. A., Wendker H. J., 1981, A&A, 93, 48

Anderson A. J., 1997, PhD thesis, University of California, Berkeley

Anderson J., Bedin L. R., 2010, PASP, 122, 1035

Anderson J., Ryon J. E., 2018, Technical report, Improving the Pixel-Based CTE-correction Model for ACS/WFC

Anderson J., van der Marel R. P., 2010, ApJ, 710, 1032

Anderson L. D., Bania T. M., Balser D. S., Rood R. T., 2011, ApJS, 194, 32

Anderson L. D., Bania T. M., Balser D. S., Cunningham V., Wenger T. V., Johnstone B. M., Armentrout W. P., 2014, ApJS, 212, 1

Anderson L. D., Armentrout W. P., Johnstone B. M., Bania T. M., Balser D. S., Wenger T. V., Cunningham V., 2015, ApJS, 221, 26

Anderson L. D., Armentrout W. P., Luisi M., Bania T. M., Balser D. S., Wenger T. V., 2018, ApJS, 234, 33

Andreuzzi G., Buonanno R., Fusi Pecci F., Iannicola G., Marconi G., 2000, A&A, 353, 944

Andreuzzi G., Testa V., Marconi G., Alcaino G., Alvarado F., Buonanno R., 2004, A&A, 425, 509

Archinal B. A., Hynes S. J., 2003, Star Clusters

Ashman K. M., Zepf S. E., 1998, Globular Cluster Systems

Bailey S. I., 1893, A&A, 12, 689

Bailey S. I., 1916, Annals of Harvard College Observatory, 76, 43

Bailey S. I., 1931, The history and work of Harvard observatory, 1839 to 1927; an outline of the origin, development, and researches of the Astronomical observatory of Harvard college together with brief biographies of its leading members. p. 1

Ballot B., 1845, Annalen der Physik, 142, 321

Bania T. M., Anderson L. D., Balser D. S., Rood R. T., 2010, ApJl, 718, L106

Bania T. M., Anderson L. D., Balser D. S., 2012, ApJ, 759, 96

Bastian U., 2019, A&A, 630, L8

Bastian N., Covey K. R., Meyer M. R., 2010, ARA&A, 48, 339

Bastian N., et al., 2016, MNRAS, 460, L20

Batchelor R. A., Caswell J. L., Haynes R. F., Wellington K. J., Goss W. M., Knowles S. H., 1980, Australian Journal of Physics, 33, 139

Battersby C., Bally J., Jackson J. M., Ginsburg A., Shirley Y. L., Schlingman W., Glenn J., 2010, ApJ, 721, 222

Baumgardt H., 2017, MNRAS, 464, 2174

Baumgardt H., Hilker M., 2018, MNRAS, 478, 1520

Baumgardt H., Makino J., 2003, MNRAS, 340, 227

Baumgardt H., Hilker M., Sollima A., Bellini A., 2019a, MNRAS, 482, 5138

Baumgardt H., et al., 2019b, MNRAS, 488, 5340

Beasley M. A., 2020, arXiv e-prints, p. arXiv:2003.04093

Bellini A., et al., 2014, ApJ, 797, 115

Bellini A., Bianchini P., Varri A. L., Anderson J., Piotto G., van der Marel R. P., Vesperini E., Watkins L. L., 2017, ApJ, 844, 167

Benjamin R. A., et al., 2003, PASP, 115, 953

Beuther H., Churchwell E. B., McKee C. F., Tan J. C., 2007, Protostars and Planets V, pp 165–180

Beuther H., Walsh A. J., Longmore S. N., 2009, ApJS, 184, 366

Bianchini P., Sills A., van de Ven G., Sippel A. C., 2017, MNRAS, 469, 4359

Bica E., Bonatto C., Dutra C. M., Santos J. F. C., 2008, MNRAS, 389, 678

Bica E., Westera P., Kerber L. d. O., Dias B., Maia F., Santos João F. C. J., Barbuy B., Oliveira R. A. P., 2020, AJ, 159, 82

Binney J., Tremaine S., 2008, Galactic Dynamics: Second Edition

Breen S. L., Ellingsen S. P., Caswell J. L., Lewis B. E., 2010a, MNRAS, 401, 2219

Breen S. L., Caswell J. L., Ellingsen S. P., Phillips C. J., 2010b, MNRAS, 406, 1487

Bruzual G., Charlot S., 2003, MNRAS, 344, 1000

Burnham Robert J., 1978, Burnham's Celestial Handbook: An Observer's Guide to the Universe Beyond the Solar System, in three volumes.

Busfield A. L., Purcell C. R., Hoare M. G., Lumsden S. L., Moore T. J. T., Oudmaijer R. D., 2006, MNRAS, 366, 1096

Butler M. J., Tan J. C., Teyssier R., Rosdahl J., Van Loo S., Nickerson S., 2017, ApJ, 841, 82

Caldwell N., Schiavon R., Morrison H., Rose J. A., Harding P., 2011, AJ, 141, 61

Cannon A. J., 1931, PASP, 43, 317

Cantat-Gaudin T., Anders F., 2020, A&A, 633, A99

Cantat-Gaudin T., et al., 2018, A&A, 618, A93

Cappellari M., et al., 2012, Nature, 484, 485

Carey S. J., et al., 2009, PASP, 121, 76

Carretta E., Bragaglia A., Gratton R. G., Recio-Blanco A., Lucatello S., D'Orazi V., Cassisi S., 2010, A&A, 516, A55

Castro-Ginard A., et al., 2020, A&A, 635, A45

Caswell J. L., 1998, MNRAS, 297, 215

Caswell J. L., 2009, PASA, 26, 454

Caswell J. L., Haynes R. F., 1987a, Australian Journal of Physics, 40, 215

Caswell J. L., Haynes R. F., 1987b, A&A, 171, 261

Caswell J. L., Vaile R. A., Ellingsen S. P., 1995a, Publications of the Astronomical Society of Australia, 12, 37

Caswell J. L., Vaile R. A., Ellingsen S. P., Whiteoak J. B., Norris R. P., 1995b, MNRAS, 272, 96

Caswell J. L., Vaile R. A., Ellingsen S. P., Norris R. P., 1995c, MNRAS, 274, 1126

Cha S.-H., Whitworth A. P., 2003, MNRAS, 340, 91

Chambers E. T., Jackson J. M., Rathborne J. M., Simon R., 2009, ApJS, 181, 360

Chapin S. L., 1957, Isis. Journal of the History of Science Society, 48, 13

Childress M., Vogt F., Nielsen J., Sharp R., 2014a, PyWiFeS: Wide Field Spectrograph data reduction pipeline, Astrophysics Source Code Library (ascl:1402.034)

Childress M. J., Vogt F. P. A., Nielsen J., Sharp R. G., 2014b, Ap&SS, 349, 617

Choi J., Dotter A., Conroy C., Cantiello M., Paxton B., Johnson B. D., 2016, ApJ, 823, 102

Chomiuk L., Strader J., Maccarone T. J., Miller-Jones J. C. A., Heinke C., Noyola E., Seth A. C., Ransom S., 2013, ApJ, 777, 69

Christensen L. L., Nielsen L. H., Nielsen K. K., Johansen T., Hurt R., de Martin D., 2012, FITS Liberator: Image processing software, Astrophysics Source Code Library (ascl:1206.002)

Chun M. S., 1978, AJ, 83, 1062

Churchwell E., Walmsley C. M., Cesaroni R., 1990, A&AS, 83, 119

Churchwell E., et al., 2009, PASP, 121, 213

Cole S., Lacey C. G., Baugh C. M., Frenk C. S., 2000, MNRAS, 319, 168

Conroy C., 2013, Annual Review of Astronomy and Astrophysics, 51, 393

Conroy C., Gunn J. E., 2010, ApJ, 712, 833

Conroy C., Gunn J. E., White M., 2009, ApJ, 699, 486

Cook A., 1998, Edmond Halley. Charting the heavens and the seas

Correnti M., Goudfrooij P., Puzia T. H., de Mink S. E., 2015, MNRAS, 450, 3054

Cote P., Welch D. L., Fischer P., Da Costa G. S., Tamblyn P., Seitzer P., Irwin M. J., 1994, ApJS, 90, 83

Courtes G., 1982, An Integral Field Spectrograph (IFS) for Large Telescopes. p. 123, doi:10.1007/978-94-009-7787-7˙16

Cyganowski C. J., et al., 2008, AJ, 136, 2391

D'Antona F., Milone A. P., Tailo M., Ventura P., Vesperini E., di Criscienzo M., 2017, Nature Astronomy, 1, 0186

D'Souza R., Rix H.-W., 2013, MNRAS, 429, 1887

Da Costa G. S., Freeman K. C., Kalnajs A. J., Rodgers A. W., Stapinski T. E., 1977, AJ, 82, 810

Dale J. E., Ercolano B., Bonnell I. A., 2013, MNRAS, 430, 234

Dalessandro E., Schiavon R. P., Rood R. T., Ferraro F. R., Sohn S. T., Lanzoni B., O'Connell R. W., 2012, AJ, 144, 126

Dalgleish H. S., Longmore S. N., Peters T., Henshaw J. D., Veitch-Michaelis J. L., Urquhart J. S., 2018, MNRAS, 478, 3530

Dalgleish H., et al., 2020, MNRAS, 492, 3859

Davies M. B., 2013, Globular Cluster Dynamical Evolution. p. 879, doi:10.1007/978-94-007-5612-0˙17

Davies B., Bastian N., Gieles M., Seth A. C., Mengel S., Konstantopoulos I. S., 2011, MNRAS, 411, 1386

Deharveng L., et al., 2015, A&A, 582, A1

Dias B., Kerber L. O., Barbuy B., Santiago B., Ortolani S., Balbinot E., 2014, A&A, 561, A106

Dias B., Barbuy B., Saviane I., Held E. V., Da Costa G. S., Ortolani S., Gullieuszik M., Vásquez S., 2016, A&A, 590, A9

Dick S. J., 2013, Discovery and Classification in Astronomy

Dieter N. H., 1967, ApJ, 150, 435

Djorgovski S., 1988, in Grindlay J. E., Philip A. G. D., eds, IAU Symposium Vol. 126, The Harlow-Shapley Symposium on Globular Cluster Systems in Galaxies. pp 333–345

Djorgovski S., King I. R., 1986, ApJl, 305, L61

Djorgovski S., Meylan G., 1994, AJ, 108, 1292

Djorgovski S. G., Gal R. R., McCarthy J. K., Cohen J. G., de Carvalho R. R., Meylan G., Bendinelli O., Parmeggiani G., 1997, ApJ, 474, L19

Dopita M., Hart J., McGregor P., Oates P., Bloxham G., Jones D., 2007, Ap&SS, 310, 255

Dopita M., et al., 2010, Ap&SS, 327, 245

Doppler C., 1842, Abhandlungen der k. Böhm, 2, 465

Dotter A., 2016, ApJS, 222, 8

Dotter A., Sarajedini A., Anderson J., 2011, ApJ, 738, 74

Draper H., 1880, Nature, 22, 583

Dravskikh A. F., Dravskikh Z. V., 1967, AZh, 44, 35

Dubath P., Meylan G., Mayor M., Magain P., 1990, A&A, 239, 142

Dubath P., Mayor M., Meylan G., 1993, Velocity Dispersion and Metallicity Determinations from High-Resolution Integrated Light Spectra in the Cores of 57 Globular Clusters. p. 557

Dubath P., Meylan G., Mayor M., 1997, A&A, 324, 505

Dull J. D., Cohn H. N., Lugger P. M., Murphy B. W., Seitzer P. O., Callanan P. J., Rutten R. G. M., Charles P. A., 1997, ApJ, 481, 267

Dullemond C. P., Juhasz A., Pohl A., Sereshti F., Shetty R., Peters T., Commercon B., Flock M., 2012, RADMC-3D: A multi-purpose radiative transfer tool, Astrophysics Source Code Library (ascl:1202.015)

Egan M. P., Shipman R. F., Price S. D., Carey S. J., Clark F. O., Cohen M., 1998, ApJl, 494, L199

Elmegreen B. G., Efremov Y. N., 1997, ApJ, 480, 235

Elson R. A. W., 1991, ApJS, 76, 185

Elson R. A. W., 1992, MNRAS, 256, 515

Elson R. A. W., Freeman K. C., 1985, ApJ, 288, 521

Elson R., Hut P., Inagaki S., 1987a, ARA&A, 25, 565

Elson R. A. W., Fall S. M., Freeman K. C., 1987b, ApJ, 323, 54

Elson R. A. W., Fall S. M., Freeman K. C., 1989a, ApJ, 336, 734

Elson R. A. W., Freeman K. C., Lauer T. R., 1989b, ApJl, 347, L69

Feast M. W., 1958, MNRAS, 118, 618

Feast M. W., Black C., 1980, MNRAS, 191, 285

Feast M. W., Thackeray A. D., 1960, MNRAS, 120, 463

Fellgett P., 1955, Optica Acta, 2, 9

Ferraro F. R., Carretta E., Bragaglia A., Renzini A., Ortolani S., 1997, MNRAS, 286, 1012

Ferraro F. R., et al., 2018, ApJ, 860, 50

Ferraro F. R., Lanzoni B., Dalessandro E., Cadelano M., Raso S., Mucciarelli A., Beccari G., Pallanca C., 2019, Nature Astronomy, 3, 1149

Fischer P., Welch D. L., Mateo M., 1993, AJ, 105, 938

Fischler M. A., Bolles R. C., 1981, Commun. ACM, 24, 381

Frank M. J., Grebel E. K., Küpper A. H. W., 2014, MNRAS, 443, 815

Freeman K. C., 1974, in Reiz A., ed., Research Programmes for the New Large Telescopes. p. 177

Freeman K. C., Gascoigne S. C. B., 1977, Proceedings of the Astronomical Society of Australia, 3, 136

Fregeau J. M., Gürkan M. A., Joshi K. J., Rasio F. A., 2003, ApJ, 593, 772

Fryxell B., et al., 2000, ApJS, 131, 273

Galilei G., 1610, Sidereus nuncius, doi:10.3931/e-rara-695.

Gallart C., Monelli M., Monteagudo-Narvión L., Carrera R., Stetson P. B., 2015, The Star Formation History of the Magellanic Clouds: An Observer's Perspective. p. 267, doi:10.1007/978-3-319-10614-4˙22

Gallazzi A., Bell E. F., 2009, ApJS, 185, 253

Galván-Madrid R., Rodríguez L. F., Ho P. T. P., Keto E., 2008, ApJl, 674, L33

Galván-Madrid R., Peters T., Keto E. R., Mac Low M.-M., Banerjee R., Klessen R. S., 2011, MNRAS, 416, 1033

Galván-Madrid R., Goddi C., Rodríguez L. F., 2012, A&A, 547, L3

Gao B., Goodman J., Cohn H., Murphy B., 1991, ApJ, 370, 567

Garay G., Rodriguez L. F., van Gorkom J. H., 1986, ApJ, 309, 553

Gaume R. A., Claussen M. J., 1990, ApJ, 351, 538

Gaume R. A., Fey A. L., Claussen M. J., 1994, ApJ, 432, 648

Gaume R. A., Goss W. M., Dickel H. R., Wilson T. L., Johnston K. J., 1995, ApJ, 438, 776

Gebhardt K., Pryor C., Williams T. B., Hesser J. E., 1995, AJ, 110, 1699

Gebhardt K., Pryor C., Williams T. B., Hesser J. E., Stetson P. B., 1997, AJ, 113, 1026

Gebhardt K., Pryor C., O'Connell R. D., Williams T. B., Hesser J. E., 2000, AJ, 119, 1268

Georgelin Y. M., Georgelin Y. P., 1976, A&A, 49, 57

Getman K. V., Feigelson E. D., Kuhn M. A., Broos P. S., Garmire G. P., 2019, AJ, 158, 235

Giannetti A., Leurini S., Wyrowski F., Urquhart J., Csengeri T., Menten K. M., König C., Güsten R., 2017, A&A, 603, A33

Gieles M., Zocchi A., 2015, MNRAS, 454, 576

Gieles M., Heggie D. C., Zhao H., 2011, MNRAS, 413, 2509

Giesers B., et al., 2018, MNRAS, 475, L15

Giesers B., et al., 2019, A&A, 632, A3

Gingerich O., 2010, The General History of Astronomy

Girardi L., Bressan A., Bertelli G., Chiosi C., 2000, A&AS, 141, 371

Girardi L., et al., 2013, MNRAS, 431, 3501

Girichidis P., Federrath C., Banerjee R., Klessen R. S., 2011, MNRAS, 413, 2741

Girichidis P., et al., 2016, MNRAS, 456, 3432

Giveon U., Becker R. H., Helfand D. J., White R. L., 2005a, AJ, 129, 348

Giveon U., Becker R. H., Helfand D. J., White R. L., 2005b, AJ, 130, 156

Glatt K., Grebel E. K., Koch A., 2010, A&A, 517, A50

Gonzalez O. A., Battaglia G., 2018, arXiv e-prints, p. arXiv:1810.04422

Gordon M. A., Sorochenko R. L., 2002, Radio Recombination Lines. Their Physics and Astronomical Applications. Vol. 282, doi:10.1007/978-0-387-09604-9,

Gouliermis D. A., 2018, PASP, 130, 072001

Green J. A., McClure-Griffiths N. M., 2011, MNRAS, 417, 2500

Green J. A., et al., 2012, MNRAS, 420, 3108

Greenfield P., White R. L., 2000, in Manset N., Veillet C., Crabtree D., eds, Astronomical Society of the Pacific Conference Series Vol. 216, Astronomical Data Analysis Software and Systems IX. p. 59

Greenfield P., White R. L., 2006, in Koekemoer A. M., Goudfrooij P., Dressel L. L., eds, The 2005 HST Calibration Workshop: Hubble After the Transition to Two-Gyro Mode. p. 437

Griffin R. F., 1967, ApJ, 148, 465

Gunn J. E., Griffin R. F., 1979, AJ, 84, 752

Gutermuth R. A., Heyer M., 2015, AJ, 149, 64

Habing H. J., Israel F. P., 1979, ARA&A, 17, 345

Hafez I., Stephenson F. R., Orchiston W., 2015, in New Insights From Recent Studies in Historical Astronomy: Following in the Footsteps of F. Richard Stephenson. p. 143, doi:10.1007/978-3-319-07614-0˙10

Haghi H., Khalaj P., Hasani Zonoozi A., Kroupa P., 2017, ApJ, 839, 60

Halley E., 1679, Catalogus Stellarum Australium sive Supplementum Catalogi Tychonici exhibens Longitudines et Latitudines Stellarum fixarum...

Harris W. E., 1996, AJ, 112, 1487

Harris W. E., 2010, arXiv e-prints, p. arXiv:1012.3224

Harrison T. G., 1984, QJRAS, 25, 65

Haworth T. J., Glover S. C. O., Koepferl C. M., Bisbas T. G., Dale J. E., 2018, New Astronomy Reviews, 82, 1

Hearnshaw J., 2009, Astronomical Spectrographs and their History, doi:10.1017/CBO9780511735288.

Hearnshaw J. B., 2014, The Analysis of Starlight

Heggie D. C., 1975, MNRAS, 173, 729

Heggie D. C., 2014, MNRAS, 445, 3435

Heggie D. C., Giersz M., 2008, MNRAS, 389, 1858

Helfand D. J., Becker R. H., White R. L., Fallon A., Tuttle S., 2006, AJ, 131, 2525

Hénault-Brunet V., et al., 2012, A&A, 546, A73

Hénon M., 1961, Annales d'Astrophysique, 24, 369

Hénon M., 1965, Annales d'Astrophysique, 28, 62

Henshaw J. D., et al., 2016, MNRAS, 457, 2675

Herschel W., 1786, Philosophical Transactions of the Royal Society of London Series I, 76, 457

Herschel W., 1789, Philosophical Transactions of the Royal Society of London Series I, 79, 212

Herschel W., 1791, Philosophical Transactions of the Royal Society of London Series I, 81, 71

Herschel W., 1802, Philosophical Transactions of the Royal Society of London Series I, 92, 477

Herschel W., 1814, Philosophical Transactions of the Royal Society of London Series I, 104, 248

Hoare M. G., et al., 2012, PASP, 124, 939

Hockey T., et al., 2007, The Biographical Encyclopedia of Astronomers, doi:10.1007/978-0-387-30400-7.

Hodierna G. B., 1654, De systemate orbis cometici deque admirandis coeli characteribus explicantur, necnon vie Com etarum, per orbem cometicum multiplices opuscula duo, in quorum primo cometarum causae disquiruntur, & indicantur. In secundo vero quid, quales, quotue sint stellae luminosae, nebulae, necnon, & occultae, manifestantur & rerum caelestium studiosis commendantur, doi:10.3931/e-rara-444.

Hoglund B., Mezger P. G., 1965, Science, 150, 339

Holden E., 1882, Astronomical and Meteorological Observations made at the U.S. Naval Observatory, 18, a1

Hopkins P. F., Kereš D., Oñorbe J., Faucher-Giguère C.-A., Quataert E., Murray N., Bullock J. S., 2014, MNRAS, 445, 581

Hoskin M., 2008, Journal for the History of Astronomy, 39, 363

Hoskin M., 2011a, Discoverers of the Universe: William and Caroline Herschel

Hoskin M., 2011b, Journal for the History of Astronomy, 42, 177

Hoskin M., 2011c, Journal for the History of Astronomy, 42, 321

Hoskin M., 2012, The Construction of the Heavens

Hou L. G., Han J. L., 2014, A&A, 569, A125

Huggins W., 1868, Philosophical Transactions of the Royal Society of London Series I, 158, 529

Hunter D. A., Elmegreen B. G., Dupuy T. J., Mortonson M., 2003, AJ, 126, 1836

Hunter T. R., et al., 2018, Understanding Massive Star Formation through Maser Imaging. p. 321

Husser T.-O., Wende-von Berg S., Dreizler S., Homeier D., Reiners A., Barman T., Hauschildt P. H., 2013, A&A, 553, A6

Husser T.-O., et al., 2016, A&A, 588, A148

Ibata R., Sollima A., Nipoti C., Bellazzini M., Chapman S. C., Dalessandro E., 2011, ApJ, 738, 186

Illingworth G., 1976, ApJ, 204, 73

Illingworth G., Illingworth W., 1976, ApJS, 30, 227

Immer K., Cyganowski C., Reid M. J., Menten K. M., 2014, A&A, 563, A39

Jaffe D. T., Martín-Pintado J., 1999, ApJ, 520, 162

Johnson C. O., De Pree C. G., Goss W. M., 1998, ApJ, 500, 302

Jones K. G., 1975, The Search for the Nebulae

Juvela M., 1996, A&AS, 118, 191

Kamann S., Wisotzki L., Roth M. M., 2013, A&A, 549, A71

Kamann S., Wisotzki L., Roth M. M., Gerssen J., Husser T. O., Sandin C., Weilbacher P., 2014, A&A, 566, A58

Kamann S., et al., 2016, A&A, 588, A149

Kamann S., et al., 2018a, MNRAS, 473, 5591

Kamann S., et al., 2018b, MNRAS, 480, 1689

Kamann S., et al., 2020, MNRAS, 492, 966

Kardashev N. S., 1959, Soviet Ast., 3, 813

Katz N., Weinberg D. H., Hernquist L., 1996, ApJS, 105, 19

Kaufmann P., et al., 1976, Nature, 260, 306

Keeler J. E., 1890a, PASP, 2, 265

Keeler J. E., 1890b, PASP, 2, 284

Kennicutt R. C., Evans N. J., 2012, ARA&A, 50, 531

Kerber L. O., Santiago B. X., 2006, A&A, 452, 155

Kereš D., Katz N., Davé R., Fardal M., Weinberg D. H., 2009, MNRAS, 396, 2332

Keto E., 2002, ApJ, 568, 754

Keto E., 2003, ApJ, 599, 1196

Keto E., 2007, ApJ, 666, 976

Keto E., Klaassen P., 2008, ApJl, 678, L109

Keto E., Wood K., 2006, ApJ, 637, 850

Keto E. R., Ho P. T. P., Haschick A. D., 1988, ApJ, 324, 920

Keto E., Zhang Q., Kurtz S., 2008, ApJ, 672, 423

Kim C.-G., Ostriker E. C., Kim W.-T., 2013, ApJ, 776, 1

Kim W.-J., Wyrowski F., Urquhart J. S., Menten K. M., Csengeri T., 2017, A&A, 602, A37

Kimmig B., Seth A., Ivans I. I., Strader J., Caldwell N., Anderton T., Gregersen D., 2015, AJ, 149, 53

King E. S., 1931, Popular Astronomy, 39, 456

King I., 1962, AJ, 67, 471

King I. R., 1966, AJ, 71, 64

King I. R., Hedemann Edmund J., Hodge S. M., White R. E., 1968, AJ, 73, 456

King I. R., Sosin C., Cool A. M., 1995, ApJl, 452, L33

Kirby E. N., Simon J. D., Geha M., Guhathakurta P., Frebel A., 2008, ApJl, 685, L43

Kirchhoff G., Bunsen R., 1860, Poggendorfs Annalen der Physik, 110, 161

Klaassen P. D., Wilson C. D., Keto E. R., Zhang Q., 2009, ApJ, 703, 1308

Klaassen P. D., Galván-Madrid R., Peters T., Longmore S. N., Maercker M., 2013, A&A, 556, A107

Klaassen P. D., et al., 2018, A&A, 611, A99

Klessen R. S., Heitsch F., Mac Low M.-M., 2000, ApJ, 535, 887

Klumpke-Roberts D., 1929, L'Astronomie, 43, 284

Klumpke-Roberts D., 1931, Popular Astronomy, 39, 23

Koch A., Grebel E. K., Odenkirchen M., Martínez-Delgado D., Caldwell J. A. R., 2004, AJ, 128, 2274

Kontizas M., Danezis E., Kontizas E., 1982, A&AS, 49, 1

Koposov S. E., Belokurov V., Torrealba G., 2017, MNRAS, 470, 2702

Kremer K., Lu W., Rodriguez C. L., Lachat M., Rasio F. A., 2019, ApJ, 881, 75

Kroupa P., 2001, MNRAS, 322, 231

Kruijssen J. M. D., 2012, MNRAS, 426, 3008

Kruijssen J. M. D., Pfeffer J. L., Reina-Campos M., Crain R. A., Bastian N., 2019, MNRAS, 486, 3180

Krumholz M. R., McKee C. F., 2020, MNRAS,

Krumholz M. R., Cunningham A. J., Klein R. I., McKee C. F., 2010, ApJ, 713, 1120

Krumholz M. R., et al., 2014, Protostars and Planets VI, pp 243–266

Krumholz M. R., McKee C. F., Bland -Hawthorn J., 2019, ARA&A, 57, 227

Kuhn M. A., Hillenbrand L. A., Sills A., Feigelson E. D., Getman K. V., 2019, ApJ, 870, 32

Kurtz S., 2002, Ultracompact HII Regions. p. 81

Lada C. J., Lada E. A., 2003, ARA&A, 41, 57

Lane J. M. M., Navarro J. F., Fattahi A., Oman K. A., Bovy J., 2020, MNRAS, 492, 4164

Lanzoni B., et al., 2013, ApJ, 769, 107

Lanzoni B., et al., 2019, ApJ, 887, 176

Leibundgut B., et al., 2019, The Messenger, 176, 16

Libralato M., et al., 2018, ApJ, 861, 99

Lockman F. J., 1989, ApJS, 71, 469

Lockman F. J., Pisano D. J., Howard G. J., 1996, ApJ, 472, 173

Lockyer W. J. S., 1900, Nature, 61, 533

Longmore S. N., Burton M. G., Barnes P. J., Wong T., Purcell C. R., Ott J., 2007, MNRAS, 379, 535

Longmore S. N., Burton M. G., Keto E., Kurtz S., Walsh A. J., 2009, MNRAS, 399, 861

Longmore S. N., et al., 2014, in Beuther H., Klessen R. S., Dullemond C. P., Henning T., eds, Protostars and Planets VI. p. 291 (arXiv:1401.4175), doi:10.2458/azu˙uapress˙9780816531240-ch013

Longmore S. N., et al., 2017, MNRAS, 470, 1462

Lumsden S. L., Hoare M. G., 1996, ApJ, 464, 272

Lumsden S. L., Hoare M. G., 1999, MNRAS, 305, 701

Lynden-Bell D., Wood R., 1968, MNRAS, 138, 495

MacLeod G. C., Gaylard M. J., 1992, MNRAS, 256, 519

Mackey A. D., 2009, in Mamajek E. E., Soderblom D. R., Wyse R. F. G., eds, IAU Symposium Vol. 258, The Ages of Stars. pp 275–286, doi:10.1017/S1743921309031925

Mackey A. D., Gilmore G. F., 2003a, MNRAS, 338, 85

Mackey A. D., Gilmore G. F., 2003b, MNRAS, 338, 120

Mackey A. D., Wilkinson M. I., Davies M. B., Gilmore G. F., 2008, MNRAS, 386, 65

Mackey A. D., Da Costa G. S., Ferguson A. M. N., Yong D., 2013, ApJ, 762, 65

Maddox R. L., 1871, The British Journal of Photography, 18, 422

Madrid J. P., Leigh N. W. C., Hurley J. R., Giersz M., 2017, MNRAS, 470, 1729

Maia F. F. S., Piatti A. E., Santos J. F. C., 2014, MNRAS, 437, 2005

Maia F. F. S., et al., 2019, MNRAS, 484, 5702

Makino J., 1996, ApJ, 471, 796

Mapelli M., 2017, MNRAS, 467, 3255

Maraston C., 2005, MNRAS, 362, 799

Marius S., 1614, Mundus Iovialis Anno M.DC.IX.Detectus Ope Perspicill Belgici, Hoc est, Quatuor Jovialium Planetarum, cum Theoria, tum Tabulæ, Propriis Observationibus Maxime Fundatæ

Martinazzi E., Pieres A., Kepler S. O., Costa J. E. S., Bonatto C., Bica E., 2014, MNRAS, 442, 3105

Martins L. P., Lima-Dias C., Coelho P. R. T., Laganá T. F., 2019, MNRAS, 484, 2388

Martocchia S., et al., 2017, MNRAS, 468, 3150

Martocchia S., et al., 2018, MNRAS, 473, 2688

Mateo M., 1988, ApJ, 331, 261

Mateo M., 1989, Ap&SS, 156, 85

Mateo M., Welch D., Fischer P., 1991, in Haynes R., Milne D., eds, IAU Symposium Vol. 148, The Magellanic Clouds. p. 191

Maunder E. W., 1885, The Observatory, 8, 162

Maunder E. W., 1892, The Observatory, 15, 393

Mayor M., et al., 1997, AJ, 114, 1087

McGee R. X., Gardner F. F., Robinson B. J., 1967, Australian Journal of Physics, 20, 407

McGrath A., 2019, Master's thesis, Simmons College, Boston, Massachusetts

McLaughlin D. E., van der Marel R. P., 2005, The Astrophysical Journal Supplement Series, 161, 304

McLaughlin D. E., Anderson J., Meylan G., Gebhardt K., Pryor C., Minniti D., Phinney S., 2006, ApJS, 166, 249

McMullin J. P., Waters B., Schiebel D., Young W., Golap K., 2007, in Shaw R. A., Hill F., Bell D. J., eds, Astronomical Society of the Pacific Conference Series Vol. 376, Astronomical Data Analysis Software and Systems XVI. p. 127

Merritt D., Piatek S., Portegies Zwart S., Hemsendorf M., 2004, ApJl, 608, L25

Meylan G., 1988, ApJ, 331, 718

Meylan G., Dubath P., Mayor M., 1991, M/L ratios of two LMC globular clusters: NGC 1835 and NGC 1978.. pp 158–160

Mezger P. G., Hoglund B., 1967, ApJ, 147, 490

Mezger P. G., Altenhoff W., Schraml J., Burke B. F., Reifenstein E. C. I., Wilson T. L., 1967, ApJl, 150, L157

Mieske S., Frank M. J., Baumgardt H., Lützgendorf N., Neumayer N., Hilker M., 2013, A&A, 558, A14

Miocchi P., et al., 2013, ApJ, 774, 151

Montegriffo P., Ferraro F. R., Fusi Pecci F., Origlia L., 1995, MNRAS, 276, 739

Moore J. H., 1932, Publications of Lick Observatory, 18, v

Morscher M., Umbreit S., Farr W. M., Rasio F. A., 2013, ApJl, 763, L15

Morscher M., Pattabiraman B., Rodriguez C., Rasio F. A., Umbreit S., 2015, ApJ, 800, 9

Moscadelli L., et al., 2018, A&A, 616, A66

Motte F., Bontemps S., Louvet F., 2018, ARA&A, 56, 41

Muratov A. L., Kereš D., Faucher-Giguère C.-A., Hopkins P. F., Quataert E., Murray N., 2015, MNRAS, 454, 2691

Murray N., Ménard B., Thompson T. A., 2011, ApJ, 735, 66

Myers A. T., Krumholz M. R., Klein R. I., McKee C. F., 2011, ApJ, 735, 49

Nasim O. W., 2013, Observing by Hand: Sketching the Nebulae in the Nineteenth Century

Newman A. B., Treu T., Ellis R. S., Sand D. J., 2013, ApJ, 765, 25

Niederhofer F., Hilker M., Bastian N., Silva-Villa E., 2015, A&A, 575, A62

Niederhofer F., et al., 2017, MNRAS, 464, 94

Nitadori K., Aarseth S. J., 2012, MNRAS, 424, 545

Núñez A., Ostriker J. P., Naab T., Oser L., Hu C.-Y., Choi E., 2017, ApJ, 836, 204

Oort J. H., van Herk G., 1959, Bull. Astron. Inst. Netherlands, 14, 299

Ostriker J. P., Spitzer Lyman J., Chevalier R. A., 1972, ApJl, 176, L51

Palacios A., Gebran M., Josselin E., Martins F., Plez B., Belmas M., Lèbre A., 2010, A&A, 516, A13

Palmer H. K., 1899, ApJ, 10, 246

Paresce F., de Marchi G., Jedrzejewski R., 1995, ApJl, 442, L57

Pasachoff J. M., 2018, Simon Marius's Mundus Iovialis and the Discovery of the Moons of Jupiter. p. 191, doi:10.1007/978-3-319-92621-6˙5

Paxton B., Bildsten L., Dotter A., Herwig F., Lesaffre P., Timmes F., 2011, ApJS, 192, 3

Paxton B., et al., 2013, ApJS, 208, 4

Paxton B., et al., 2015, ApJS, 220, 15

Pestalozzi M. R., Minier V., Booth R. S., 2005, A&A, 432, 737

Peters T., Banerjee R., Klessen R. S., Mac Low M.-M., Galván-Madrid R., Keto E. R., 2010a, ApJ, 711, 1017

Peters T., Mac Low M.-M., Banerjee R., Klessen R. S., Dullemond C. P., 2010b, ApJ, 719, 831

Peters T., Klessen R. S., Mac Low M.-M., Banerjee R., 2010c, ApJ, 725, 134

Peters T., Longmore S. N., Dullemond C. P., 2012, MNRAS, 425, 2352

Peters T., Klaassen P. D., Mac Low M.-M., Schrön M., Federrath C., Smith M. D., Klessen R. S., 2014, ApJ, 788, 14

Peters T., et al., 2017, MNRAS, 466, 3293

Peterson R. C., Seitzer P., Cudworth K. M., 1989, ApJ, 347, 251

Piatti A. E., Mackey A. D., 2018, MNRAS, 478, 2164

Pickering E. C., Fleming M., 1897, Annals of Harvard College Observatory, 26, 193

Pietrinferni A., Cassisi S., Salaris M., Castelli F., 2004, ApJ, 612, 168

Piotto G., et al., 2002, A&A, 391, 945

Price-Whelan A. M., Bonaca A., 2018, ApJl, 863, L20

Pryor C., Meylan G., 1993, in Djorgovski S. G., Meylan G., eds, Astronomical Society of the Pacific Conference Series Vol. 50, Structure and Dynamics of Globular Clusters. p. 357

Reber G., Greenstein J. L., 1947, The Observatory, 67, 15

Reid M. J., et al., 2009, ApJ, 700, 137

Reid M. J., et al., 2014, ApJ, 783, 130

Reid M. J., et al., 2019, ApJ, 885, 131

Reifenstein E. C., Wilson T. L., Burke B. F., Mezger P. G., Altenhoff W. J., 1970, A&A, 4, 357

Reijns R. A., Seitzer P., Arnold R., Freeman K. C., Ingerson T., van den Bosch R. C. E., van de Ven G., de Zeeuw P. T., 2006, A&A, 445, 503

Renaud F., 2020, in Bragaglia A., Davies M., Sills A., Vesperini E., eds, IAU Symposium Vol. 351, IAU Symposium. pp 40–46 (arXiv:1908.02301), doi:10.1017/S1743921319007312

Renzini A., Ciotti L., 1993, ApJ, 416, L49

Rezaeikh S., Javadi A., Khosroshahi H., van Loon J. T., 2014, MNRAS, 445, 2214

Roberts I., 1893, A Selection of Photographs of Stars, Star-Clusters and Nebulae, together with Information concerning the Instruments and the Methods employed in the pursuit of Celestial Photography

Roberts I., 1899, A Selection of Photographs of Stars, Star-Clusters and Nebulae, together with Records of Results obtained in the pursuit of Celestial Photography (Volume 2)

Rodrigues M., et al., 2018, in Proc. SPIE. p. 107029M, doi:10.1117/12.2313396

Rodriguez L. F., Bastian T. S., 1994, ApJ, 428, 324

Rodriguez L. F., Moran J. M., Canto J., Kahn F. D., 1988, in Bulletin of the American Astronomical Society. p. 1031

Rosse E. O., 1861, Philosophical Transactions of the Royal Society of London Series I, 151, 681

Sabbi E., et al., 2012, ApJl, 754, L37

Sánchez-Blázquez P., et al., 2006, MNRAS, 371, 703

Santiago B. X., 2009, in Van Loon J. T., Oliveira J. M., eds, IAU Symposium Vol. 256, The Magellanic System: Stars, Gas, and Galaxies. pp 69–80 (arXiv:0810.1514), doi:10.1017/S1743921308028287

Saracino S., et al., 2015, ApJ, 806, 152

Saracino S., et al., 2020, MNRAS, 493, 6060

Sawyer Hogg H., 1959, Star Clusters. Springer Berlin Heidelberg, pp 129–207, doi:10.1007/978-3-642-45932-0˙4

Scannapieco C., et al., 2012, MNRAS, 423, 1726

Science Software Branch at STScI 2012, PyRAF: Python alternative for IRAF, Astrophysics Source Code Library (ascl:1207.011)

Seitzer P., 1991, in Haynes R., Milne D., eds, IAU Symposium Vol. 148, The Magellanic Clouds. p. 213

Serio G. F., Indorato L., Nastasi P., 1985, Journal for the History of Astronomy, 16, 1

Sewiło M., Churchwell E., Kurtz S., Goss W. M., Hofner P., 2004, ApJ, 605, 285

Sewiło M., Churchwell E., Kurtz S., Goss W. M., Hofner P., 2008, ApJ, 681, 350

Shanahan R. L., Gieles M., 2015, MNRAS, 448, L94

Shapley H., 1930, Star Clusters. Vol. 2

Shara M. M., Drissen L., Bergeron L. E., Paresce F., 1995, ApJ, 441, 617

Shaver P. A., Retallack D. S., Wamsteker W., Danks A. C., 1981, A&A, 102, 225

Shepherd D. S., Churchwell E., Goss W. M., 1995, ApJ, 448, 426

Shishkovsky L., et al., 2018, ApJ, 855, 55

Simkin S. M., 1974, A&A, 31, 129

Simpson J. D., et al., 2017, MNRAS, 471, 4087

Smith B., Struve O., 1944, ApJ, 100, 360

Smyth W. H., 1864, Sidereal Chromatics

Soderberg A. M., Pilachowski C. A., Barden S. C., Willmarth D., Sneden C., 1999, PASP, 111, 1233

Sollima A., Baumgardt H., 2017, MNRAS, 471, 3668

Sollima A., Bellazzini M., Smart R. L., Correnti M., Pancino E., Ferraro F. R., Romano D., 2009, MNRAS, 396, 2183

Sollima A., Dalessandro E., Beccari G., Pallanca C., 2017, MNRAS, 464, 3871

Sollima A., Baumgardt H., Hilker M., 2019, MNRAS, 485, 1460

Sollins P. K., Zhang Q., Keto E., Ho P. T. P., 2005, ApJl, 624, L49

Somerville R. S., Primack J. R., 1999, MNRAS, 310, 1087

Sommariva V., Piotto G., Rejkuba M., Bedin L. R., Heggie D. C., Mathieu R. D., Villanova S., 2009, A&A, 493, 947

Song Y.-Y., Mateo M., Mackey A. D., Olszewski E. W., Roederer I. U., Walker M. G., Bailey J. I., 2019, MNRAS, 490, 385

Sorochenko R. L., Borodzich É. V., 1966, Soviet Physics Doklady, 10, 588

Sosin C., 1997, AJ, 114, 1517

Sosin C., King I. R., 1997, AJ, 113, 1328

Soto M., et al., 2017, AJ, 153, 19

Spitzer Lyman J., 1969, ApJl, 158, L139

Spitzer L., 1978, Physical processes in the interstellar medium, doi:10.1002/9783527617722.

Spitzer L., 1987, Dynamical evolution of globular clusters

Springel V., Hernquist L., 2003, MNRAS, 339, 312

Steinicke W., 2010, Observing and Cataloguing Nebulae and Star Clusters

Stodolkiewicz J. S., 1986, Acta Astronomica, 36, 19

Strader J., Smith G. H., Larsen S., Brodie J. P., Huchra J. P., 2009, AJ, 138, 547

Strader J., Caldwell N., Seth A. C., 2011, AJ, 142, 8

Strader J., Chomiuk L., Maccarone T. J., Miller-Jones J. C. A., Seth A. C., 2012, Nature, 490, 71

Strömgren B., 1939, ApJ, 89, 526

Struve O., 1944, ApJ, 100, 189

Sugimoto D., Bettwieser E., 1983, MNRAS, 204, 19P

Suntzeff N. B., Schommer R. A., Olszewski E. W., Walker A. R., 1992, AJ, 104, 1743

Tanaka K. E. I., Tan J. C., Zhang Y., 2016, ApJ, 818, 52

Tasker E. J., Wadsley J., Pudritz R., 2015, ApJ, 801, 33

Taylor J. H., Cordes J. M., 1993, ApJ, 411, 674

Thatte N. A., et al., 2014, HARMONI: the first light integral field spectrograph for the E-ELT. p. 914725, doi:10.1117/12.2055436

Tonry J., Davis M., 1979, AJ, 84, 1511

Torniamenti S., Bertin G., Bianchini P., 2019, A&A, 632, A67

Torrealba G., Belokurov V., Koposov S. E., 2019, MNRAS, 484, 2181

Trager S. C., King I. R., Djorgovski S., 1995, AJ, 109, 218

Trumpler R. J., 1935, PASP, 47, 249

Urquhart J. S., et al., 2013a, MNRAS, 431, 1752

Urquhart J. S., et al., 2013b, MNRAS, 435, 400

Usher C., Forbes D. A., Spitler L. R., Brodie J. P., Romanowsky A. J., Strader J., Woodley K. A., 2013, MNRAS, 436, 1172

Usher C., et al., 2017, MNRAS, 468, 3828

Usher C., et al., 2019, MNRAS, 482, 1275

Vanderriest C., 1980, PASP, 92, 858

Vazdekis A., Koleva M., Ricciardelli E., Röck B., Falcón-Barroso J., 2016, MNRAS, 463, 3409

Vázquez-Semadeni E., Palau A., Ballesteros-Paredes J., Gómez G. C., Zamora-Avilés M., 2019, MNRAS, 490, 3061

Veena V. S., Vig S., Tej A., Kantharia N. G., Ghosh S. K., 2017, MNRAS, 465, 4219

Vogel H., 1873, Astronomische Nachrichten, 82, 291

Vogel H. C., 1889, Astronomische Nachrichten, 121, 241

Voggel K. T., Seth A. C., Baumgardt H., Mieske S., Pfeffer J., Rasskazov A., 2019, ApJ, 871, 159

Walsh A. J., Hyland A. R., Robinson G., Burton M. G., 1997, MNRAS, 291, 261

Walsh A. J., Burton M. G., Hyland A. R., Robinson G., 1998, MNRAS, 301, 640

Walsh A. J., et al., 2011, MNRAS, 416, 1764

Walsh A. J., Purcell C. R., Longmore S. N., Breen S. L., Green J. A., Harvey-Smith L., Jordan C. H., Macpherson C., 2014, MNRAS, 442, 2240

Wang L., et al., 2016, MNRAS, 458, 1450

Ward J. L., Kruijssen J. M. D., Rix H.-W., 2020, MNRAS, 495, 663

Watkins L. L., van der Marel R. P., Bellini A., Anderson J., 2015, ApJ, 812, 149

Watkins E. J., Peretto N., Marsh K., Fuller G. A., 2019a, A&A, 628, A21

Watkins L. L., van der Marel R. P., Sohn S. T., Evans N. W., 2019b, ApJ, 873, 118

Weatherford N. C., Chatterjee S., Rodriguez C. L., Rasio F. A., 2018, ApJ, 864, 13

Weisz D. R., Dolphin A. E., Skillman E. D., Holtzman J., Dalcanton J. J., Cole A. A., Neary K., 2013, MNRAS, 431, 364

Wenger T. V., et al., 2019, ApJS, 240, 24

Wild J. P., 1952, ApJ, 115, 206

Wilkinson M. I., Hurley J. R., Mackey A. D., Gilmore G. F., Tout C. A., 2003, MNRAS, 343, 1025

Wilson O. C., Coffeen M. F., 1954, ApJ, 119, 197

Wilson T. L., Mezger P. G., Gardner F. F., Milne D. K., 1970, A&A, 6, 364

Wink J. E., Altenhoff W. J., Mezger P. G., 1982, A&A, 108, 227

Winlock J., Trouvelot L., 1876, Annals of Harvard College Observatory, 8, P1.1

Wolf M. J., et al., 2018, in Proc. SPIE. p. 107022O, doi:10.1117/12.2312792

Wood D. O. S., Churchwell E., 1989, ApJS, 69, 831

Wright N. J., Parker R. J., 2019, MNRAS, 489, 2694

Yang A. Y., Thompson M. A., Tian W. W., Bihr S., Beuther H., Hindson L., 2019, MNRAS, 482, 2681

Zaggia S. R., Capaccioli M., Piotto G., Stiavelli M., 1992, A&A, 258, 302

Zaritsky D., Colucci J. E., Pessev P. M., Bernstein R. A., Chandar R., 2014, ApJ, 796, 71

Zhang C.-P., Wang J.-J., Xu J.-L., Wyrowski F., Menten K. M., 2014, ApJ, 784, 107

Zik Y., Hon G., Manulis I., 2020, arXiv e-prints, p. arXiv:2002.04643

Zocchi A., Gieles M., Hénault-Brunet V., 2017, MNRAS, 468, 4429

Zonoozi A. H., Küpper A. H. W., Baumgardt H., Haghi H., Kroupa P., Hilker M., 2011, MNRAS, 411, 1989

Zonoozi A. H., Haghi H., Kroupa P., 2016, ApJ, 826, 89

de Boer T. J. L., Gieles M., Balbinot E., Hénault-Brunet V., Sollima A., Watkins L. L., Claydon I., 2019, MNRAS, 485, 4906

de Grijs R., 2009, Ap&SS, 324, 283

de La Peña M. D., White R. L., Greenfield P., 2001, in Harnden Jr. F. R., Primini F. A., Payne H. E., eds, Astronomical Society of the Pacific Conference Series Vol. 238, Astronomical Data Analysis Software and Systems X. p. 59

de Marchi G., Paresce F., 1996, ApJ, 467, 658

de Pree C. G., Goss W. M., Palmer P., Rubin R. H., 1994, ApJ, 428, 670

de Pree C. G., Rodriguez L. F., Dickel H. R., Goss W. M., 1995, ApJ, 447, 220

de Pree C. G., Gaume R. A., Goss W. M., Claussen M. J., 1996, ApJ, 464, 788

de Pree C. G., Mehringer D. M., Goss W. M., 1997, ApJ, 482, 307

de Pree C. G., Wilner D. J., Mercer A. J., Davis L. E., Goss W. M., Kurtz S., 2004, ApJ, 600, 286

de Pree C. G., Wilner D. J., Deblasio J., Mercer A. J., Davis L. E., 2005, ApJl, 624, L101

de Pree C. G., et al., 2014, ApJl, 781, L36

de Pree C. G., et al., 2015, ApJ, 815, 123

van Leeuwen F., Le Poole R. S., Reijns R. A., Freeman K. C., de Zeeuw P. T., 2000, A&A, 360, 472

van de Hulst H. C., 1945, Nederladsch Tidjschrift voor Naturkunde, 11, 210

van der Marel R. P., Gerssen J., Guhathakurta P., Peterson R. C., Gebhardt K., 2002, AJ, 124, 3255

vandenBerg D. A., Brogaard K., Leaman R., Casagrand e L., 2013, ApJ, 775, 134